SiD Letter of Intent

Vertex and Tracking Companion Document

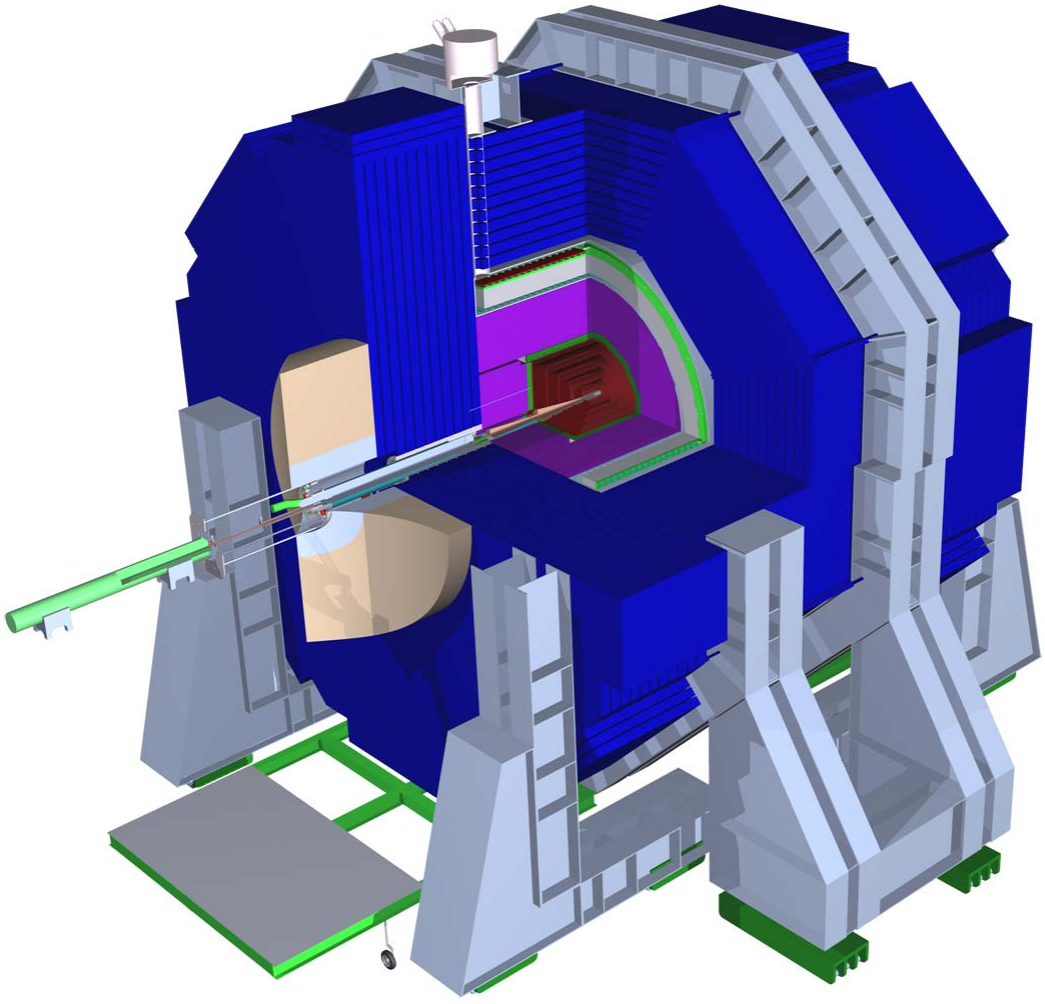

Contents

1.1 Vertex and Tracking System

1.1.1 Introduction

The tracking system of the SiD detector uses a barrel-disk layout. Five cylindrical layers of pixel detectors surround the interaction point, complemented by four disks of pixel sensors on either end. These inner layers are followed by a set of five barrels of silicon strip sensors in the central region, capped by four nested disks of silicon strip sensors at both ends. To provide uniform hit coverage, three disks with pixel sensors are provided in the transition region between the inner and outer disks in both the forward and backward region.

Within the SiD detector concept the tracking system is regarded as an integrated tracking system. Although individual detector components can be identified in the vertexing and tracking system, the overall design is driven by the combined performance of the pixel detector at small radius, the outer strip detector at large radius and the electromagnetic calorimeter for the identification of minimum ionizing track stubs. The physics at the ILC requires good track reconstruction and particle identification for a wide array of topologies. The main elements for the pattern recognition are the highly pixellated vertex detector and the low occupancy outer strip detector.

Early track finding studies relied on identifying tracks in the vertex detector, where pattern recognition is simplified by the fact that precise three-dimensional information is available for each hit. Tracks found in the vertex detector are then propagated into the outer tracker, picking up additional hits. While good performance was achieved using this approach, an important class of events, notably highly boosted b-quarks, will decay at radii that do not allow for pattern recognition in the vertex detector alone. To provide additional flexibility, a more general tracking algorithm has been developed that can seed tracks using any three layers in the tracker, either from the outer tracker, the vertex detector or a combination of both. Tracks produced by the decay products of long-lived particles, however, can leave too few hits in the tracker to be reconstructed using only hits in the tracking volume. Obvious examples are long-lived particles such as K_s^0's and Λ's. The detector should also be capable of detecting new physics signatures that would include long-lived exotic particles like those predicted by some gauge-mediated supersymmetry breaking scenarios. There are also issues of reconstructing kinked tracks produced by particles that lose a substantial portion of their energy in the tracker, as well as reconstructing backscatters from the calorimeter. To capture the tracks from these event topologies a calorimeter-assisted tracking algorithm has been employed. This algorithm uses the electromagnetic calorimeter to provide seeds for pattern recognition in the tracker. The very fine segmentation of the EM calorimeter allows for detection of traces left by minimum ionizing particles. These can be used to determine the track entry point, direction, and sometimes curvature with a precision sufficient for extrapolating the track back into the tracker. This set of complementary algorithms provides for very robust pattern recognition and track finding and it is the performance of this integrated tracking system that determines the overall physics reach of the detector.

In the next section the boundary conditions for operating an integrated tracking system at the ILC will be presented. These will form the basis for the choice of design of the overall system, which will be discussed in the following section. The remainder will describe the

details of the design, the implementation of the detector in the Monte Carlo simulations and some preliminary results. We will conclude with a discussion of the R&D needed in the next few years.

1.1.2 Beam Environment

The bunch structure of the ILC, which consists of trains of 2820 bunches which are spaced 308 ns apart, repeated 5 times per second, and the physics and machine backgrounds resulting from bunch-bunch collisions, impose many constraints on ILC detector technologies and on the readout electronics. The two main backgrounds are backgrounds from the interaction point and machine backgrounds. Events contributing to the first category are

- disrupted primary beam
- beamstrahlung photons
- e^+e^--pairs from beam-beam interactions
- radiative Bhabha events
- hadrons or muons from $\gamma\gamma$ interactions.

The second category is populated with events from

- direct beam losses
- beam-gas interactions
- collimator edge scattering
- synchrotron radiation
- neutron back-shine from the beam dump
- extraction line losses

Although these constraints are mild compared to those imposed on LHC detectors, the high flux of photons concomitant with the collisions, from virtual sources and beamstrahlung, results in the copious production of e^+e^--pairs as well as the frequent production of muon pairs and hadronic interactions. The e^+e^--pairs account for most of the background in the inner detectors, directly as charged tracks with low transverse momentum. They also cause a general flux of photons in the MeV energy range, which results when they shower in the beam calorimeters on the front face of the final quadrupoles. These photons, and the higher transverse momentum muons and charged and neutral hadrons which also result from photon-photon interactions, spray the entire detector with charged particles and photons.

As will be quantified in the following sections, SiD is largely immune to these backgrounds because the detector as a whole is only sensitive to backgrounds associated with a

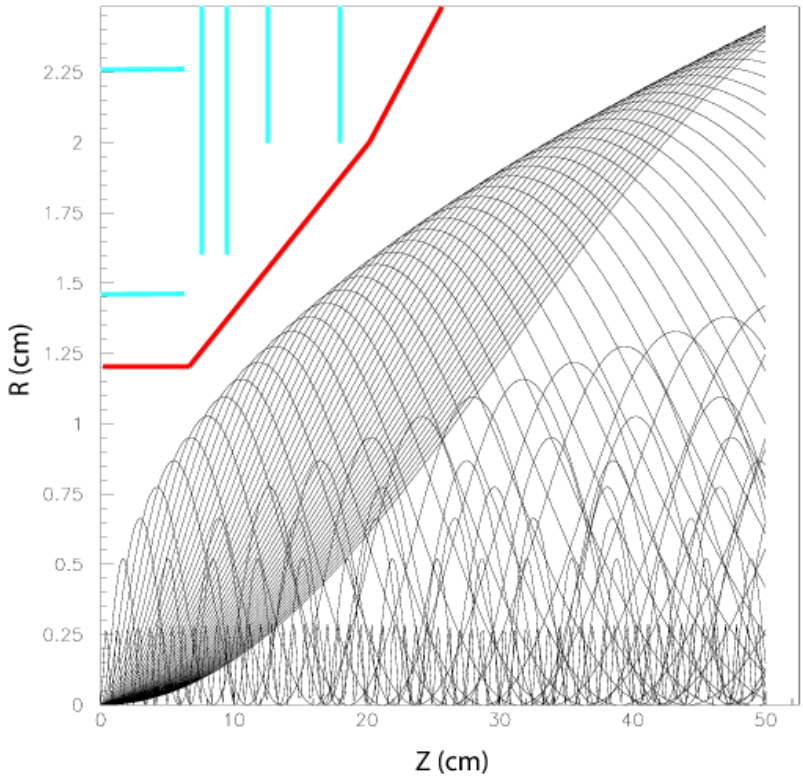

Figure 1.1: Maximum envelope of the e^+e^--pair backgrounds in a 5 Tesla field. Indicated is the 12 mm radius beampine.

single bunch crossing. The pixel detector is assumed to have a bunch-by-bunch timestamp and a channel-by-channel buffer, which is 4 deep in the current design, will store hits over the course of the entire bunch train and record each responsible bunch crossing, for the silicon strip detector. Similarly for the electromagnetic calorimeter. Consequently, SiD is sensitive only to the physics and backgrounds of a single bunch crossing.

The effects of these backgrounds have been evaluated with the Guinea-Pig program. The nominal ILC beam parameters have been used for the simulation. The beamline magnets up to about 20 m from the interaction point have been included, using a beam crossing angle of 14 *mrad*. The nearest quadrupole magnet of the final doublet ends at 3.51 m. The detector solenoid field is 5 Tesla, and a field map instead of a constant field is used for the calculations of the beam backgrounds. The beam pipe through the central portion of the vertex detector has been taken to be all-beryllium. Within the barrel region of the vertex detector, the beryllium beam pipe has been taken to be a straight cylinder with inner radius of 1.2 cm and a wall thickness of 0.04 cm. At $z = \pm 6.25$ cm, a transition is made to a conical beam pipe with a wall thickness of 0.07 cm. The half angle of the cone is 3.266^o. Transitions from beryllium to stainless steel are made beyond the tracking volume, at approximately $z = \pm 20.5$ cm. The initial stainless steel wall thickness is 0.107 cm; it increases to 0.15 cm at approximately $z = \pm 120$ cm. The half angle of the stainless steel cone is 5.329^o. The

inner profile of the beam pipe is dictated by the need to avoid the envelope of beam related backgrounds, as shown in Fig. 1.1. A titanium liner of thickness 0.0025 cm is has been included within the central beryllium portions of the beam pipe. The liner provides shielding against soft X-rays (¡ 10 keV). The titanium liner in the cone section of the beam pipe is expected to be a factor of 3 thicker than in the central region to take into account the incidence angle of back-scattered photons.

With these assumptions, the background in the tracking detector has been evaluated. The background hits in the vertex detector come predominantly from the e^+e^-pairs. The number of VXD hits in the first barrel layer of the vertex detector is expected to be nearly 80 hits/mm^2/train over the full train for 500 GeV operations; at 1 TeV, in the high luminosity option, this number rises to about 400 hits/mm^2/train.The charged backgrounds are appreciable only at the very small radii affecting the vertex detector and inner most sections of the forward tracking system. The hit densities from pairs in the forward vertex disks at their innermost radii match the densities in the barrel section of the detector, and the densities fall off with increasing radius. So the limits determined for the barrel detector should apply also to the forward disks. These boundary conditions, imposed by the machine, have led to the design described in the following section.

1.1.3 Vertex Detector Design

The vertex detector integrates with the outer tracker and remainder of the detector to provide significantly extended physics reach through superb vertex reconstruction – primary, secondary and tertiary. To date, all vertex detectors at collider experiments are silicon based, and the vertex detector for the SiD concept is no exception. The vertex detector consists of a central barrel section with five silicon pixel layers and forward and backward disk regions, each with four silicon pixel disks. Three silicon pixel disks at larger $\mid z \mid$ provide uniform coverage for the transition region between the vertex detector and the outer tracker. Barrel layers and disks are arranged to provide good hermeticity for $\cos\vartheta \leq 0.984$ and to guarantee good pattern recognition capability for charged tracking and excellent impact parameter resolution over the whole solid angle. A side-view of the vertex detector is shown in Fig. 1.2. For clarity, the silicon support structures have not been drawn in the right hand side of this figure.

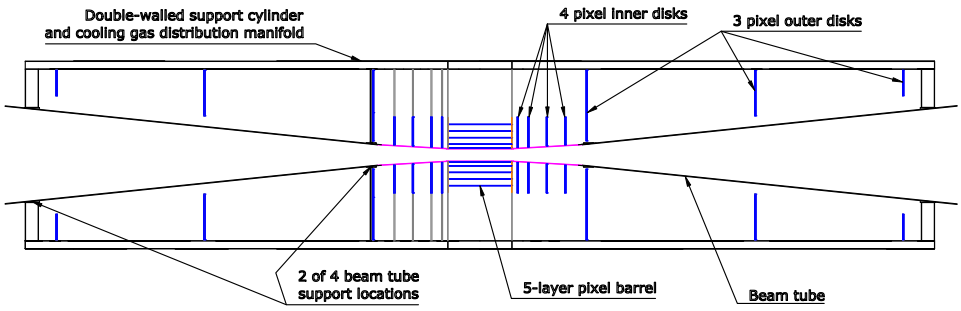

Figure 1.2: R-z view of the vertex detector. The right hand side has been drawn without the support structures.

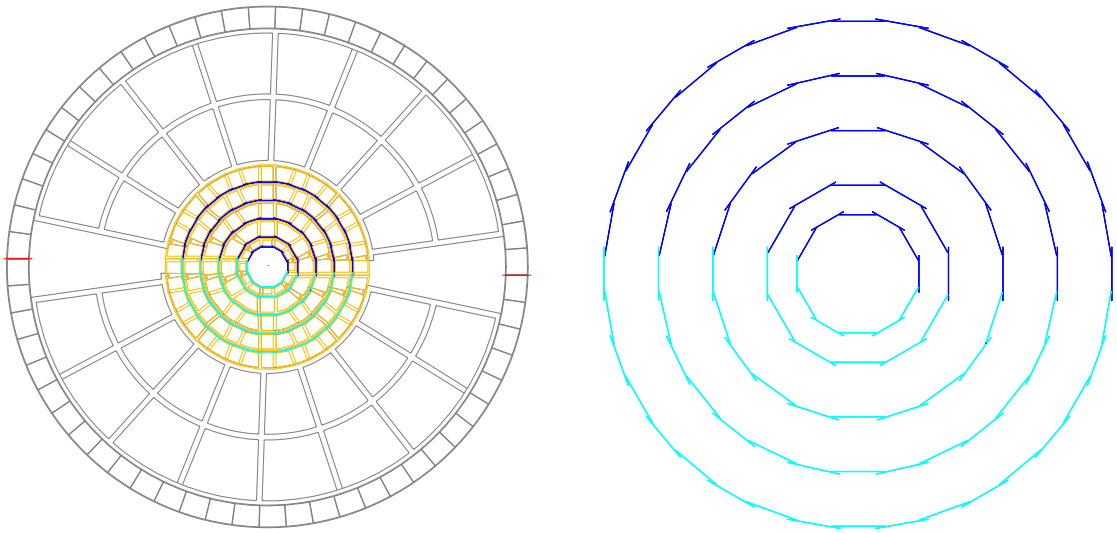

Figure 1.3: Barrel end view of the vertex detector (left) and layer arrangement of the silicon sensors only (right).

Vertex detectors are generally plagued by a mismatch in thermal expansion coefficients between the silicon and its support structures. Moreover, these supports in general add to the material budget in a region of physics phase space where it is least desired. To partially address those considerations, an 'all-silicon' structure is proposed for the vertex detector barrel. In this context, 'all-silicon' means that sensors of each barrel layer are joined along their edges with adhesive to approximate an arc of a circular cylinder, and no other structural materials are present in that limited region. Thermal distortions are reduced by limiting material to that of the sensors themselves and adhesive, which has a low elastic modulus relative to silicon. Longitudinal deflection of a layer is controlled by the cylindrical shape, thereby minimizing additional material. The quasi-cylindrical shape of a layer is maintained by annular, flat rings at each end. In turn, the end rings are joined to one another and connected to an outer support cylinder via web-like support disks. Though various possibilities are still under consideration for the end ring and support disk material, we would like a material, such as carbon fiber laminate or silicon-based foam, which has a longer radiation length than that of silicon. Because other materials than silicon are used for external mechanical connections, the term "all-silicon" is placed in quotes.

At this time, many sensor options remain under investigation and we have yet to choose a specific sensor technology. The candidates for sensor technology are discussed in the R&D section. The design presented here makes the assumption, independent of sensor technology, that fabrication and assembly of the detector occur at room temperature and that the sensors are operated at a temperature $>$ -10 ^{0}C. Because sensors are used as a structural element and other material has been minimized, our design favors relatively thick sensors. The sensor thickness has been taken to be 75 μm. Sensor cut width is 8.68 mm in the innermost layer and 12.58 mm in all other layers. The cut sensor length for all layers is 125 mm.

To allow assembly about the beam pipe and later servicing, all barrels, disks, and

support elements of the vertex detector are split about approximately the horizontal plane into top and bottom sub-assemblies. Once mated, the two sub-assemblies are supported from the beam pipe and stiffen the portion of the beam pipe passing through them. Fig. 1.3 is an end view of the barrel region, showing the five silicon barrel layers and their spoked support disk. The outer rings indicate the double-walled carbon fiber support tube. Since the silicon is very thin on the scale of this drawing, the layer arrangement of the individual sensors is shown in the right drawing in Fig. 1.3 for clarity.

The five layers are arranged at radii ranging from 14 to 60 mm. The vertex detector also has four disk layer sensors which are attached to carbon fiber support disks at z positions ranging from about 72 to 172 mm. The innermost disk covers radii from 14 mm out to 71 mm; the outermost, from 20 mm to 71 mm. Forward tracking continues beyond the vertex detector proper with three additional small pixel disks, extending in z from about 207 to 834 mm. Their inner radii range from 29 to about 117 mm, and their outer radius is about 166 mm.

The beam pipe through the central portion of the vertex detector has been taken to be all-beryllium. Within the barrel region of the vertex detector, the beryllium beam pipe has been taken to be a straight cylinder with inner radius of 1.2 cm and a wall thickness of 0.04 cm. At $z = \pm 6.25$ cm, a transition is made to a conical beam pipe with a wall thickness of 0.07 cm. The half angle of the cone is 3.266^o. Transitions from beryllium to stainless steel are made beyond the tracking volume, at approximately $z = \pm 20.5$ cm. The initial stainless steel wall thickness is 0.107 cm; it increases to 0.15 cm at approximately $z = \pm 120$ cm. The half angle of the stainless steel cone is 5.329°. The inner profile of the beam pipe is dictated by the need to avoid the envelope of beam-strahlung produced e^+e^--pairs.

To prevent bending of the small-radius portion of the beam pipe and ensure good stability of vertex detector position, the outer vertex detector support cylinder is coupled to the beam pipe at four longitudinal locations: $\pm$ 21.4 and $\pm$ 88.2 cm. Inner and outer support cylinder walls are 0.26 mm thick. They are made from four plies of high modulus carbon fiber, resin pre-preg. Wall separation is 15 mm. We propose to deliver cooling air via the vertex detector outer support cylinder. To allow that, the two walls of the cylinder would be separated by radially-oriented ribs running the full cylinder length. Calculations assumed ribs at 60 azimuths. Openings, each approximately 12.2 mm x 15 mm, at 18 z-locations in the inner cylinder wall distribute flow to the various disk locations and to the barrel.

For our initial investigation the flow for barrel cooling was assumed to be from one barrel end to the other. The average power dissipated in a sensor was taken to be 131 μW/mm^2. That corresponds to a total power of about 20 Watts for the 5-layer barrel considered. These numbers presume power cycling, i.e., that most power is dissipated during the roughly 1 ms during which the beam train is present, and that power is turned off in the 199 ms between trains. We assumed that power is distributed uniformly over the sensor active surface and that both sensor surfaces participate in heat removal. Supply air temperature was taken to be -15 ^{0}C. For a given sensor, power transferred inward through the carbon fiber cylinder was taken to be proportional to the surface contact between the sensor and carbon fiber. Thermal impedance through silicon, epoxy, and carbon fiber laminate has been included, but turns out not to be particularly significant. The remaining power was assumed to be transferred outward into the layer to layer gap. For flow and heat transfer calculations, the gap between

barrel layers was taken to be 1 mm less than the nominal layer spacing. Laminar flow was assumed.

The cooling power was evaluated as a function of Reynold's number, which was required to be the same for all barrel gaps. To provide laminar flow and limit the likelihood of vibration, a maximum Reynold's number of 1800 was considered. Cooling with turbulent flow and acceptable stability of sensor positions may also be possible, but remains to be investigated.

As mentioned before, openings, each approximately 12.2 mm x 15 mm, are envisioned at 18 z-locations and 60 azimuths in the inner cylinder wall to distribute flow to the various disk locations and to the barrel. At each azimuth, the cell through which flow passes was approximated by a rectangle of height 15 mm and width 18.246 mm. The wall thickness was assumed to be 0.26 mm for both cylinders and for all ribs. The result was a Reynold's number of 3105 in the portion of the cell which sees full flow, which indicates flow will be turbulent. Since a portion of the flow exits the cell at each opening, the Reynold's number drops to 1725 at approximately z = 51.9 cm (a short distance inboard of the two outermost disks). While entrance effects may remain, flow should gradually become laminar after that point. Supply and return connections to the outside world remain to be fully evaluated.

The sensors of the outermost layer, where it is easier to provide cross-section for air flow, and sensors in the innermost layer, where we have assumed that the beam pipe includes thermal intercepts and will introduce no heat, are noticeably cooler than sensors of the three middle layers, rather independent of the flow. In the outermost layer, the cross section provided for air flow could be reduced to raise the temperature of that layer. In the gap between the innermost layer and the beam tube, flow is likely to be lower and temperature higher, once supply and return distribution patterns of air flow have been taken into account. Higher flow rate clearly improves the uniformity of sensor temperatures end to end and reduces the difference between the temperature of a sensor and the cooling air. All flow rates which have been considered, lead to temperature variations which should be acceptable for dimensional stability, which is crucial for high precision vertexing. The time-dependent effects of power cycling remain to be investigated. Those depend on the thermal mass presented by the barrels and the details of the way in which power is cycled. External heat input to the barrel has been assumed to be negligible. Satisfying that assumption will require reasonable care in designing cables, in providing heat intercepts should they be needed, and in providing an external thermal enclosure. The outer support cylinder of the vertex detector offers a natural thermal enclosure. Details of end openings in barrel membranes remain to be included. Those openings provide a natural mechanism for adjusting relative flow between barrel layers. A membrane between the outermost barrel layer and the vertex chamber support cylinder would ensure that flow does not excessively bypass the barrel-to-barrel gaps.

Similar calculations have been made to understand disk cooling. Those calculations are based upon barrel results with a Reynold's number of 1800 (barrel flow = 20 g/s). Disk power dissipation is dependent upon the sensor technology chosen, and that choice remains to be made. At each end of the barrel region, the first four disks have been assumed to employ pixel sensors. For heat removal calculations, they have been assumed to dissipate the same power per unit area as the pixel sensors of the barrels. The result is a total power of 16.9

Watts for all eight disks and an air flow of 16.4 g/s.

For the next three disks outboard at each end the sensors were treated as silicon pixels with $\frac{1}{4}$ the power dissipation per unit area as that of barrel pixels; that assumes pixels which are twice as large. The result was a total power of 13.25 Watts for all six disks and an air flow of 12.8 g/s. The total required flow is the sum of that for the barrel, inner disks and outer disks, that is, 48.65 g/s. To take into account warming of air and to allow a small margin, flow calculations assumed an air temperature of -20 ^{0}C and a flow rate of 50 g/s.

The readout scheme for the SiD vertex detector is closely coupled to the sensor technology. Any technology will be required to adequately address hit occupancies, so that pattern recognition is not overwhelmed by background. Ideally the readout will associate hits with single beam crossings. The column-parallel CCD, DEPFET, and many MAPs-based readout schemes utilize a rolling shutter during the bunch train. In this scheme the detector frame is completely read out multiple times during the bunch train, with the effective time resolution equivalent to the frame readout time. The ISIS technology and some MAPS-based designs use in-pixel storage of multiple analog samples, with full readout between trains. The Chronopixel design stores analog pulse heights and digital and/or analog time stamps in the pixel, also with readout between trains.

The vertex detector readout is illustrated using the scheme with in-pixel storage of analog information and digital time stamps used in the 3D-VIP chip. In this scheme analog and digital information is stored within a pixel during the bunch train and read out between trains. Pixel complexity is minimized by storing address information on the periphery of the chip. Table 1.1 summarizes the power consumption of this readout scheme. Electrical connections of about one meter from the ladders to optical links installed on the support tube have been assumed. Assuming 32 bits are used per hit and 100 pF interconnect capacitance at 1.5 V, the local readout consumes 0.24 Watts of average power. If each of the 108 ladders is independently driven with a 200 MHz clock speed, the inner layers would dominate the readout time at 75 ms/ladder. The peak power at the start of readout, with all layers reading at 200 MHz, is 4.8 Watts. This could be reduced to 1.3 Watts if the outer layers are clocked more slowly to match the 75 ms inner layer readout time, or to a value close to the average power if the clock rate on each layer is tuned to match the data load. The bit rate from the entire vertex detector is about 2 Gbits/sec.

Layer	Number of ladders	hits/crossing	hits/train	bits/train	Readout time (ms)
Layer 1	12	2000	$5.6\ 10^6$	$1.8\ 10^8$	75
Layer 2	12	1200	$3.4\ 10^6$	$1.1\ 10^8$	45
Layer 3	20	800	$2.3\ 10^6$	$7.2\ 10^7$	18
Layer 4	28	450	$1.3\ 10^6$	$4.1\ 10^7$	7.3
Layer 5	36	400	$1.1\ 10^6$	$3.6\ 10^7$	5.0

Table 1.1: Readout rates for the vertex detector assuming 3D-VIP readout scheme.

The power delivery is expected to be a major source of material contribution. The

instantaneous power of many of the sensor technologies could be 50W or more per sensor. One naïve scheme is to deliver power through short copper wires with e.g. 300μm diameter or flat cables to each sensor and use DC-DC conversion on the vertex detector support cylinder from a higher supply voltage. A low mass local DC-DC conversion near the sensors with higher incoming voltage would be more favorable in many respects if it can be realized. An extension of the radiation hard optical transmission technology used for LHC detectors could be foreseen as the means of control and data transmission. The material from the thin fibers is expected to be significantly less than the material involved in power delivery. However, the major issue for both power delivery and signal transmission is the connection to the thin sensors. The miniaturization of the connectors and the transceivers will be key R&D projects to ensure the material minimization. For simulation purposes the readout section at each end of a sensor is assumed to be a 2mm tall and 5mm long block spanning the full width of the sensors with same radiation length as G10. The number of radiation lengths represented by vertex detector structures, averaged over φ in most cases, is given in Fig. 1.5.

In a 5 T solenoidal field, forces and torques acting on radial runs of power delivery cabling can be significant. When coupling with the cyclic delivery of power, as we have assumed to allow gas cooling, the result can be vibrations which are transmitted from the cables into sensors and their support structures. To mitigate those possibilities, we propose to deliver power on flat-lines with three conductor layers. The central layer, for example, would serve to supply power and the two outer layers would serve as power returns. To avoid ground currents and ensure that supply and return currents balance within a cable, some combination of isolation of power sources and isolation of sensor grounds is envisioned. Then, provided the two return currents of a cable are equal, net force and torque on the cable due to interaction of currents with the magnetic field would be zero. Power/ground isolation would also eliminate issues that arise when portions of the vertex detector are unpowered while other portions are powered. We note that the total conductor in a cable can be the same as in a more traditional, two-conductor-layer cable. We also note that coaxial cables could be used instead of flat-lines.

Power distribution at sensor locations should also be scrutinized. In the barrel, radial current runs within sensors are relatively short, thereby limiting forces and torques associated with the magnetic field. In the disks, care will need to be taken to avoid supply/return current loops within sensors. In both locations, limitation of support structure material lessens the ability of those structures to resist unexpected forces and torques. Careful design and testing will be necessary.

During silicon servicing, the vertex detector and beam pipe remain fixed while the outer silicon tracker rolls longitudinally (see Fig. 1.4). To allow that motion, to enable placement of the outer silicon tracker elements at the smallest possible radius, and to leave space for any additional thermal insulation which might be needed, the outer radius of the vertex detector, including its support structures, has been limited to 18.5 cm. To maximize physics potential, the inner radius of vertex detector elements has been chosen to be as small as practical consistent with beam-related backgrounds and the beam pipe profile. In the barrel region, the minimum radius to a sensor surface is 1.4 cm, governed by the beam backgrounds as discussed earlier.

The number of radiation lengths represented by vertex detector structures, averaged

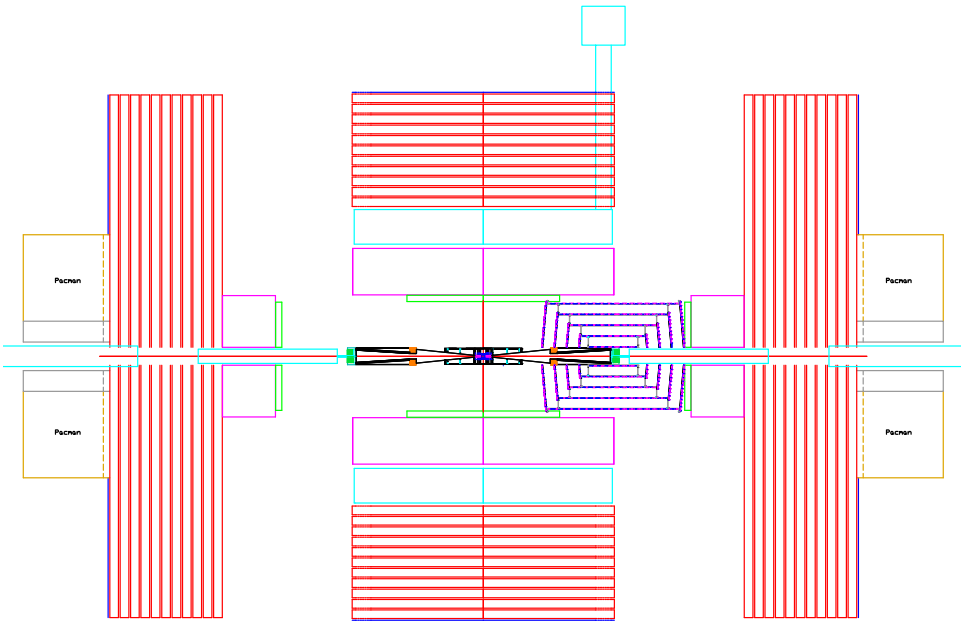

Figure 1.4: Tracker in the open position for servicing of the vertex detector.

over φ in most cases, and the vertex detector hit pattern are shown in Fig. 1.5. Shown are the contributions of the individual subdetectors to the total number of hits on a particle track with infinite momentum. The irregular features correspond to the transition regions. Overall there are more than five pixel hits on a particle trajectory down to angles of about 10°.

The irregular features of the readout and service contributions to the material budget are due to discrete elements at the end of the sensors. Most of the readout material is beyond the first few layers of the vertex detector, so that their influence on the impact parameter resolution is limited. The fact that the amount of material in these elements is comparable to that of the sensors or mechanical supports calls for close attention to the design of low mass power delivery and signal transmission components. If the readout and service material can indeed meet what is in the current model, the material balance would be more favorable for a considerable portion of the endcap region compared to the $1/\sin\vartheta$ growth for a long barrel geometry. With this material balance, the benefit of the endcap geometry in spatial resolution with a better track entrance angle and smaller radial alignment effect, is a meaningful advantage. Table 1.2 summarizes the main parameters of the vertex detector.

1.1.4 Tracker Design

The ILC experiments demand tracking systems unlike any previously envisioned. In addition to efficient and robust track-finding, the momentum resolution required to enable precision physics at ILC energies must improve significantly upon that of previous trackers. The design must minimize material in front of the calorimeter that might endanger particle-flow jet reconstruction. Even with the largest feasible magnetic field, the tracking volume is quite large so that tracker components must be relatively inexpensive and easily mass-

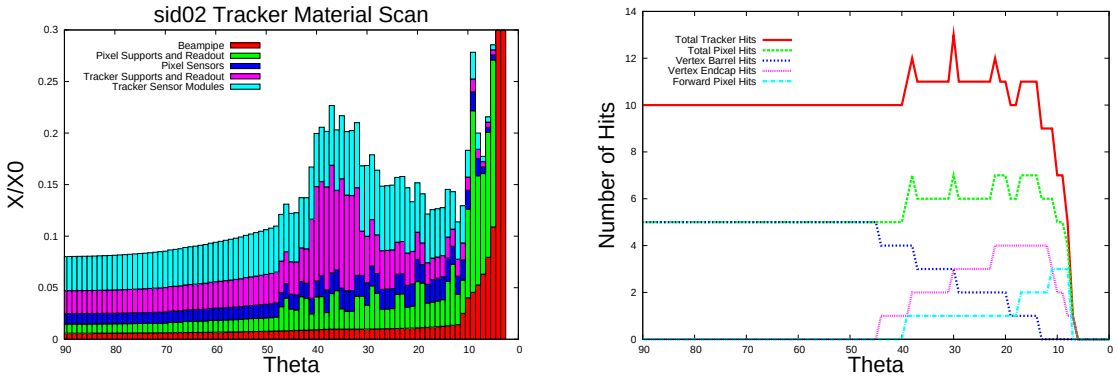

Figure 1.5: Material budget of the tracking system (left) and number of hit layers in the tracking system as a function of polar angle (right).

produced. Finally, the tracker must be robust against beam-related accidents and aging. These requirements have led to the choice of silicon microstrip detectors for the tracker. The outer silicon tracker design consists of five nested barrels in the central region and four cones in each of the end regions. The support material of disks follows a conical surface with an angle of 5-degrees with respect to the normal to the beamline. Sensors on disk modules are normal to the beam line. The barrel supports are continuous cylinders formed from a sandwich of pre-impregnated carbon fiber composite around a Rohacell core. The support cones are also double-walled carbon fiber structures around a Rohacell core. Each support cone is supported off a barrel. Spoked annular rings support the ends of each barrel cylinder from the inner surface of the next barrel out. It is expected that openings will be cut in the support structures to reduce material, once module mounting locations are known. These openings not only reduce the number of radiation lengths, but also reduce the weight to be supported. Openings may also be needed for an optical alignment system. It is envisioned that the electronics and power cables that supply entire segments of the detector are mounted on these spoked rings. The dimensions of the barrels and cones are given in Table 1.3. Fig. 1.6 shows an elevation view of the tracking system.

Because of the very low occupancies in the outer barrel, the nominal design for the outer tracker employs only axial readout in the barrel region. In the baseline design, the barrels are covered with silicon modules. Modules are comprised of a carbon fiber composite frame with rohacell/epoxy cross bracing and have one single-sided silicon sensor bonded to the outer surface. Sensors are obtained from one single 6-inch wafer and are approximately 10 cm $\times$ 10 cm. This size sets the longitudinal readout segmentation of the barrel detectors. The sensors are 300μm thick with a readout pitch of 50 μm and intermediate strips. Full coverage is obtained by ensuring small overlap both longitudinally and azimuthally. Azimuthal overlap is obtained by slightly tilting the sensors. The angle by which the sensor is tilted partially compensates for the Lorentz angle of the collected charge in the 5T field of the solenoid. Longitudinal overlap is obtained by placing alternate sensors at slightly different radii. Fig. 1.7 shows a detail of the overlap in the z and Rφ direction, respectively.

Modules are attached to the cylinder using a PEEK (Poly-Ether-Ether-Ketone) mounting clip. The readout chips and cables are mounted directly to the outer surface of the silicon

Barrel Region	R (mm)	Length (mm)	Number of sensors in φ
Layer 1	14	125	12
Layer 2	21	125	12
Layer 3	34	125	20
Layer 4	47	125	28
Layer 5	60	125	36
Disk	R_{inner}	R_{outer}	z_{center}
Disk 1	15	75	76
Disk 2	16	75	95
Disk 3	18	75	125
Disk 4	21	75	180
Forward Disk	R_{inner}	R_{outer}	z_{center}
Disk 1	28	166	211
Disk 2	76	166	543
Disk 3	118	166	834

Table 1.2: Parameters of the vertex detector. Units are mm.

sensors. The cables supply power and control to the readout chip from electronics located at the ends of the barrel.

Fig. 1.8 shows an Rφ-view of the barrel region. The outermost disk is projected onto the barrel layout in this figure. For pattern recognition in the disks, small angle stereo will provide 3d-space points. The current design has two single-sided wedge detectors back-to-back, with strips at $\pm 6^\circ$ with respect to the long axis of the wedge for a stereo angle of 12°. Please note that in Fig. 1.5 the hits from a pair of sensors, corresponding to one 3d-space point, is represented as one hit. Two types of sensors are needed to tile the disks, one type at the inner radii and a second sensor type to populate the area at the outer radii. Also in the forward region sensors will be 300μm thick with intermediate strips. The conical support disk design ("lampshade design") provides an elegant way to implement module overlaps, eliminating any dead areas, and allows for easy module mounting and cable routing. Fig. 1.9 shows a side view of modules mounted on a disk. The support disks have penetrations for cable routing. In this scheme all cable are routed on the inner surface of the disks.

The inner radius of the outer tracker is set by forward, beam-monitoring calorimetry and beamline elements, over which the tracker is intended to slide. Once the tracker inner radius is set, the outer radius of vertex detector structures follows. During servicing, the vertex detector and beam pipe remain fixed while the outer silicon tracker rolls longitudinally, as shown in Figure 1.4. To allow that motion, no element from the outer tracker can be at a radius smaller than the radius of the vertex detector outer support cylinder. To allow for good acceptance and pattern recognition, the small angle region is covered by three small

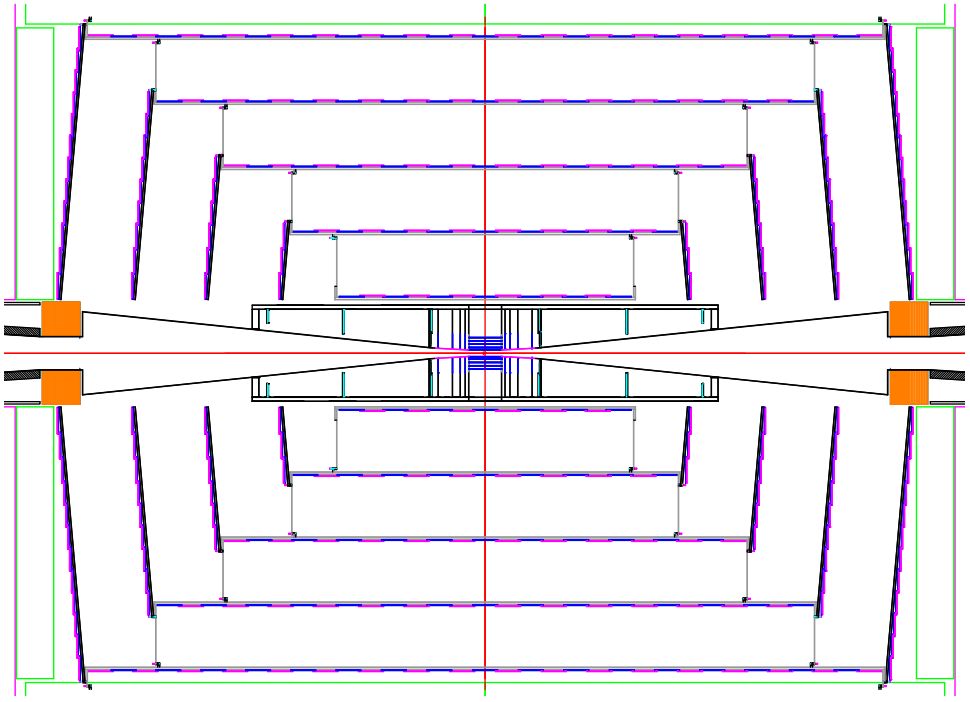

Figure 1.6: R-z view of the whole tracking system.

silicon disks at each end with radius below 20 cm, which has been described in the section on the mechanical layout of the vertex detector. Figure 1.5 shows the cumulative amount of material as a function of polar angle as modeled in the Monte Carlo. The lowest curve shows the contribution from the beampipe followed by the contribution of the support and readout structures for the pixel detector. The material corresponding to the various readout elements has conservatively been assumed to be uniformly distributed in the tracker volume. The next curve indicates the material due to the active vertex detector elements. The outer two curves give the amount of material of the tracker supports and readouts and the silicon modules, respectively. It should be noted that the material corresponding to the silicon modules includes the module supports in addition to the silicon.

Overall a material budget of about 0.8% X_0 per layer is achieved for the outer tracker. Table 1.3 lists some of the parameters of the tracker for the current design. There are 8130 modules in the barrel region and 2848 modules for the end regions combined.

1.1.5 Tracker Module Design

To build a large volume silicon tracker within an acceptable material budget is quite challenging. The scale of the project puts a premium on minimizing the number of different components and achieving a modular construction process, while at the same time limiting the mass budget of the overall system. To achieve this goal, the design of the SiD tracker employs silicon modules with novel characteristics.

A module is the most elementary working component of the SiD tracker. Each barrel

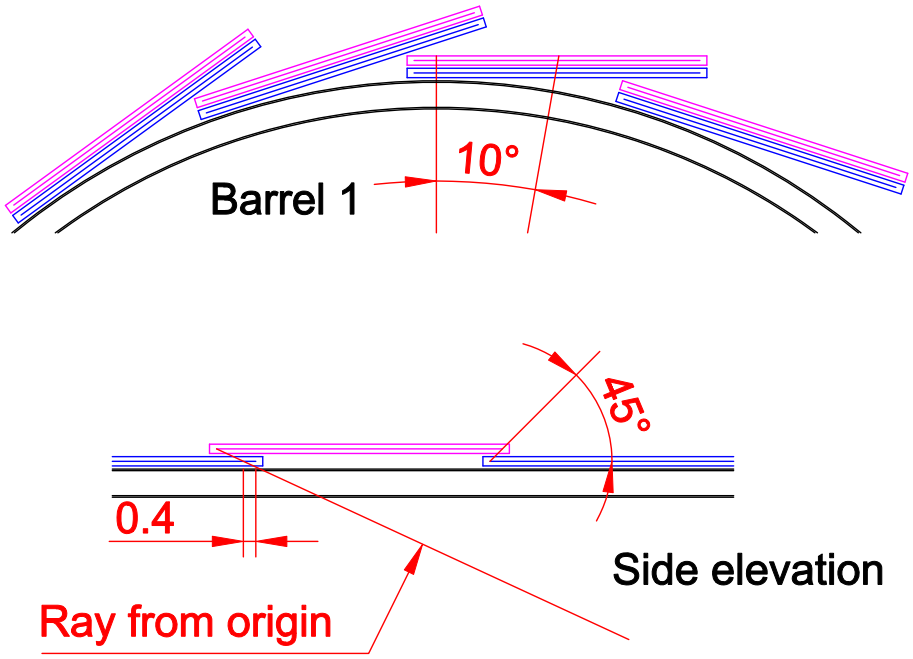

Figure 1.7: Detail of the sensor overlap in the barrel region in the z and Rφ projection.

module has a single square sensor, while an endcap module consists of two wedge-shaped sensors placed back-to-back to create a stereo pair. Each sensor is read out by a pair of 1024-channel readout ASICs, called KPiX. A short Kapton readout cable provides power and control signals to the KPiX chips and carries digitized signals to the edge of the module where they are transmitted to a longer bus cable which transmits them to the end of the tracker. There is neither a hybrid circuit board nor a mechanical cooling path since gas flow can provide the required cooling.

The barrel sensors for the SiD tracker are square, 9.53 cm on a side, 300 μm thick, <100>, single-sided, double-metal, p^+-on-n sensors with 25 μm sense pitch and 50 μm readout pitch. This floating-strip design provides the best possible single-hit resolution for a reasonable channel count as long as the signal-to-noise ration remains large, motivating the use of short readout strips to reduce capacitance. The sensors are AC-coupled with polysilicon bias resistors. Aside from having a different shape, the wedge sensors in the endcap are essentially the same. Fig. 1.10 shows a picture of a prototype sensor. Initial tests of several SiD prototype sensors indicate that the fabrication was successful. By measuring the resistance of the strips from end-to-end, as well as the resistance from one end of the strip to the end of the corresponding readout trace, the separate strip and trace resistances can be estimated. This was done for two sensors, and the strip resistance was found to be approximately 550 Ω. The resistance of a typical readout trace was found to be approximately 200 Ω. Measurements of the CV characteristics suggested a depletion voltage of approximately 50 V; a typical CV curve is shown in Fig. 1.11. At full depletion, a typical leakage current (all channels combined) was 300 nA, or about 160 pA per channel for the 1840-channel sensor.

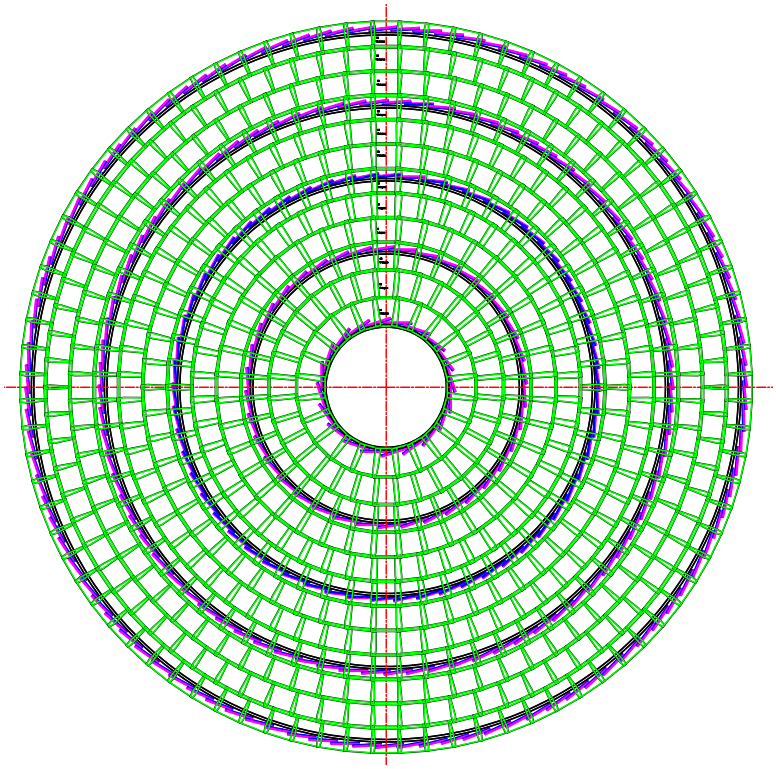

Figure 1.8: Rφ projection view of the tracker barrels and disks.

The pair of KPiX readout chips are bump-bonded directly to the face of the sensor and the readout strips of the sensor connect to the bonding array via double-metal traces (see Figure 6). Fig. 1.12 shows a detail of the double-metal routing of the traces for one half of the sensor to one of the two readout chips. The pads for bump-bonding to the readout chip are 70×70 μm^2, with a 200 by 500 μm pitch. A necessary consequence of this scheme is that the power, control and readout signals of the KPiX chip must also be routed to a bonding array from the readout cable on the double-metal layer, also shown in Fig. 1.12. Extensive modeling of the capacitances and the behavior of the KPiX chip has refined the sensor design with an emphasis on low-impedance power delivery, minimal readout capacitance and reduced coupling to potential noise sources on the power and readout traces. A reduced set of specifications for prototype barrel sensors is given Table 1.4.

The central component of the readout architecture proposed for the SiD tracker is the 1024-channel KPiX readout chip. The KPiX chip is designed for pulsed power, minimizing the input current between bunch trains. This reduces the power consumption to 20 mW on average for a 1024-channel KPiX chip, or 40 mW for a single-sided module allowing for gas cooling of the tracker. The chip has four time-stamped analog buffers per channel that store signals from the detector until the inter-train period for digitization and readout. As a result, the only digital activities on KPiX during the bunch train are a synchronous LVDS clock and individual comparators firing when a channel crosses the readout thresholds. This low-noise mode of operation during the bunch train allows KPiX to be mounted directly to the sensor without inducing large RF pickup on the strips.

Figure 1.9: Detail of the sensor overlap and cable routing for the tracker disks.

A low mass readout cable, called a "pigtail", is glued to the module and wirebonded to the double metal power and readout traces. The other end of the pigtail connects the module to a two-meter long extension cable which connects, in turn, to power and data concentrator boards at the end of the barrels, each of which serves approximately 20 sensors. The cable includes two pairs of traces each for analog and digital power, sixteen traces (eight per KPiX readout chip) for digital control and readout, along with one pair for sensor bias. The pigtail cable has a pair of tabs near the sensor edge for connection of the sensor bias as well as surface mount pads for bias and power filtering, and for LVDS signal termination resistors.

These single-sensor sized modules require minimal support, only enough to hold the sensors flat and provide stable and repeatable mounting. The support frame of a module is composed of a pair of thin, high-modulus carbon-fiber skins sandwiched around a Rohacell core. The frame has injection-molded carbon fiber filled PEEK strips on two edges into which precision silicon-nitride balls are molded, providing a kinematic, three-point mount. Mounting clips are used to place the module on the support structure. They are also injection-molded carbon fiber filled PEEK and include custom silicon nitride mating parts for the mounting balls of the support frame. The current barrel module design represents roughly 0.5% X_0 per unit coverage including the mounting clips and longer readout cables needed to connect the pigtails to the power and readout distribution boards mounted on the support rings at the ends of the barrels. Fig. 1.13 shows a sketch of a prototype barrel module.

Although a detailed design for the forward modules awaits further simulation study, it is presumed that these modules will be of similar design. The detector model currently being simulated for performance studies has modules utilizing two different wedge-shaped sensor designs for the endcaps, as shown in Fig. 1.14.

An alternative approach to the KPIX front-end readout ASIC, the Long-Shaping-Time Front End (LSTFE) ASIC, has also been under development. The LSTFE ASIC features a long (~ 1.5 μs) shaping time, typical for ILC silicon sensor readout applications, that limits

Barrel Region	$\langle R \rangle$ (cm)	Length of sensor coverage (cm)	Number of modules in φ	Number of modules in z
Barrel 1	21.95	111.6	20	13
Barrel 2	46.95	147.3	38	17
Barrel 3	71.95	200.1	58	23
Barrel 4	96.95	251.8	80	29
Barrel 5	121.95	304.5	102	35
Disk Region	z_{inner} (cm)	R_{inner} (cm)	R_{outer} (cm)	Number of modules per end
Disk 1	78.89	20.89	49.80	96
Disk 2	107.50	20.89	75.14	238
Disk 3	135.55	20.89	100.31	428
Disk 4	164.09	20.89	125.36	662

Table 1.3: Parameters of the tracking detector.

readout noise from capacitive and series-resistance load. After amplification and shaping, the signals are split in two and directed to two separate comparators. One runs at a high ($\sim$ 1.2 fC) threshold to suppress noise, while the other runs at a low ($\sim$ 0.4 fC) threshold to maximize the information used in constructing the centroid of pulses that trigger the high threshold. The charge amplitude measurement is provided by the duration of low-threshold comparator's time-over-threshold, which, in a full implementation of the ASIC, would be stored digitally in an on-board FIFO and read out asynchronously. The chip includes a power-cycling feature that is designed to allow the chip to be powered on in 1 msec, allowing the chip to reduce its power consumption by 99% by exploiting the 5 Hz duty cycle of the Linear Collider. The time-over-threshold digitization of the charge amplitude allows for real-time processing of minimum-ionizing signals, with no dead time other than that associated with the return-to-baseline of the amplified pulse. Due to its real-time processing of pulse-height information, which limits occupancy-related deadtime, the LSTFE time-over-threshold strategy is a particularly promising approach for the use of microstrips for forward tracking.

1.1.6 Simulation Infrastructure

The vertex detector and tracker designs have been incorporated in the compact *xml* detector description that drives our simulation studies. This detector description serves as an input both to *slic.org*, the GEANT4-based detector simulation used by SiD, as well as the event reconstruction software.

The current detector description includes both the active sensing elements, as well as our estimates of the dead material required to provide mechanical support, beam tube, readout electronics, and required services (including power and cooling). For the tracking

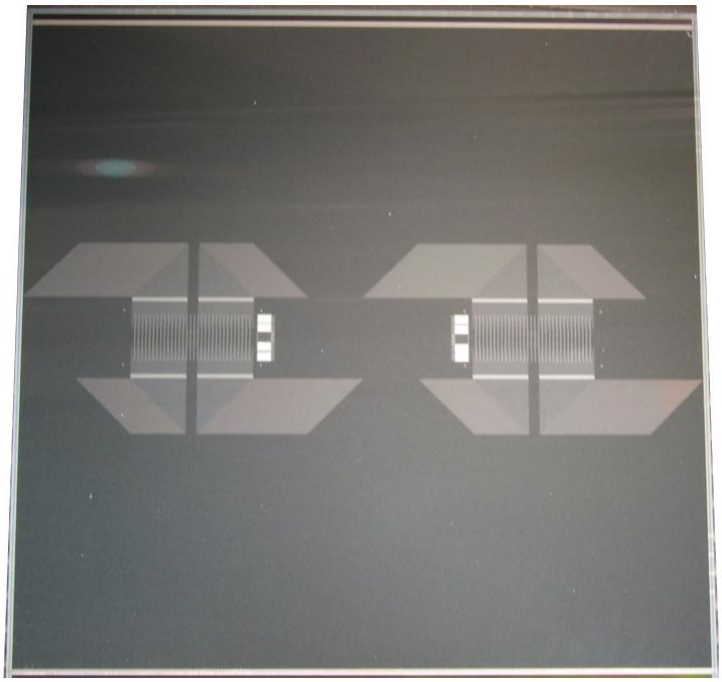

Figure 1.10: Photograph of a prototype SiD tracker sensor.

studies reported here, the barrel sensors have been approximated by thin cylinders, while the disk sensors have been approximated by planar disks perpendicular to the beamline. The dead material is modeled as a cylinder, planar disk, or cone as appropriate. Fig. 1.15 shows an x-y quarter view of the tracking system as implemented in this simplified geometry. This model has also been used to simulate the detector response for the large number of events generated for the physics benchmarking. Further details of the detector model are, therefore, presented in that section.

We have also developed a fully detailed tracker description that closely matches the engineering designs. It incorporates each individual sensor as a planar device with its mounting hardware. The fully segmented tracker description provides a highly realistic model of the tracker geometry, allowing us to study the effects of sensor overlaps and gaps, sensor mis-alignment, support material and more generally improve the precision of our detector modeling. Having the complete geometry fully defined and configurable at runtime (using a plain-text file), and immediately available to the reconstruction software, provides enormous flexibility to the design and optimization process.

Figs. 1.16 and 1.17 show the sensor layout for the fully segmented vertex detector and the sensor layout and support barrels for the central region of the fully segmented tracker description, respectively, as extracted from the GEANT4 description.

We do not include the individual pixels and strips in the GEANT4 simulation, preferring to defer this to the reconstruction stage. Instead, we store the full Monte Carlo information about the particle's interaction with the sensitive sensor material (e.g. track ID, deposited

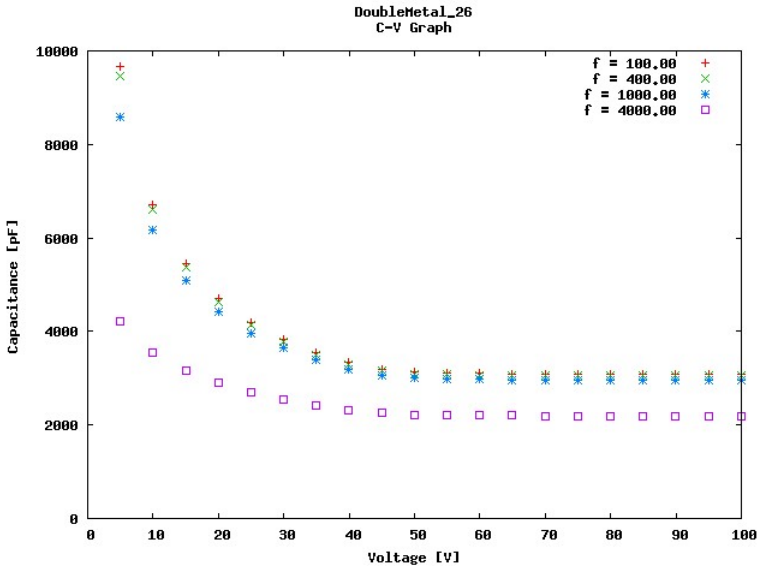

Figure 1.11: Capacitanc in pF versus bias voltage in Volt of a typical SiD double-metal prototype sensor.

energy, time, position). Hit digitization is the process of transforming these GEANT4 energy deposits into strip and pixel charge depositions, and then clustering these charge depositions to form tracker hits. This allows us to study different readout configurations without the overhead of having to rerun the full simulation.

1.1.7 Vertex Detector Hit Digitization

Although no baseline sensor technology has been established for the vertex detector, two vertex detector sensor simulation algorithms are currently implemented. The first one is based on a CCD simulation from SLD and is used in the simulation studies described here, which employs a cylindrical geometry. The second simulation package is more detailed and was developed for a more realistic planar geometry.

The main process to be simulated in a CCD is the diffusion of the charge from a charged particle track. In a CCD the larger part of the active layer is not depleted. That is, there is no electrical field in that part of the sensor and the charge collection occurs because of a slow diffusion of the charge into the CCD channel. In this case transverse diffusion has the same scale as the un-depleted layer thickness. To simulate the diffusion, a Gaussian distribution of the probability of an electron, generated at some point deep in the active layer, to reach the collection point a certain distance away from the projection of the generation point was assumed. The width of this distribution is proportional to the depth of the generation point. To be more precise, the model assumes two Gaussian distributions. The first one is for electrons that diffuse directly towards the CCD channel. The second distribution is for electrons reflected at the epitaxial layer, the substrate boundary, where there is a potential barrier. An important role in the performance of a tracking detector is played by the generation of the δ-electrons, that is, large energy transfer by the ionizing

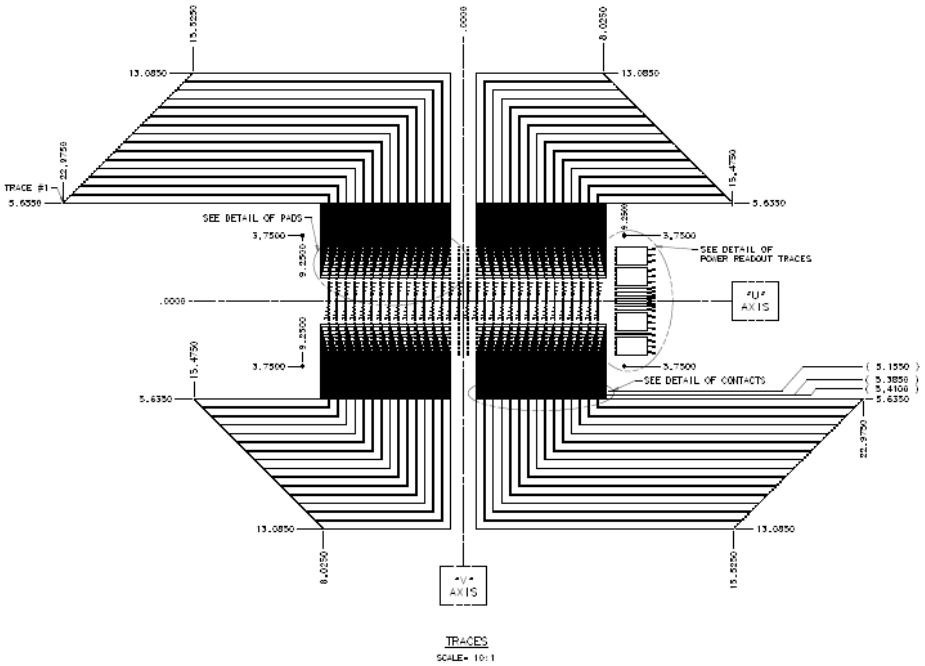

Figure 1.12: Detail of the double-metal routing of the traces to the readout chip and the connections to the readout cable, visible to the right of the bump-bond array.

particle to a single electron. This effect has been simulated by assuming that the energy loss in the tail of the Landau distribution is due to such δ-electrons. The width of the Landau distribution is simulated according to an empirical formula, which is in good agreement with experiment to thicknesses as small as about 10μm of silicon. The simulation package also includes special functions for simulating low-energy electrons, such as Compton electrons generated by photons.

Apart from the physics effects in the silicon detector, its performance is affected by the noise level of the readout electronics and the parameters of the signal digitization. All these effects have been simulated. This package does have its limitations, however, and was not designed for detailed studies of sensor effects. For example, it does not take into account specific effects in the energy loss in very thin layers ($\approx 1\mu$m). This effect as well as full simulation of diffusion and drift of charge carriers in any configuration of electric and magnetic fields inside the sensors are taken into account in second simulation package, which is described below.

The CCD simulation package starts with an initialization procedure that defines the CCD simulation parameters and geometry. At that time lookup tables are generated for the simulation of electron diffusion. The actual movement of each electron is not simulated in this package. Rather precalculated density functions for the distribution of electrons generated at a given depth inside the active layer are used. The next step in the simulation includes processing of every hit in the CCD detector. For every such hit, first the CCD and the pixel in the CCD is found where the hit is located. The CCD active layer is then divided into thin sublayers and the energy deposition in every sublayer is simulated. If the energy deposition

Parameter	**Value**
Overall Dimensions	93.531×93.531 mm^2
Active Area	92.031×92.031 mm^2
Strip pitch	25 μm
Readout pitch	50 μm
Number of strips	3679
Number of readout strips	1840
Depletion voltage	<100V
Biasing scheme	R_{poly}
Poly resistor value	20-40MΩ
Implant strip width	8 to 9 μm
Width of Al sense strips	8 to 9 μm
Width of double-metal readout traces	3 to 4 μm
Resistivity of Al sense strips	$< 25\Omega$/cm
Resistivity of double-metal readout traces	$< 60\Omega$/cm
Insulation thickness between metal layers	0.9 μm
Coupling capacitor value	> 10 pf/cm
Passivation (except bonding areas)	SiO_2, 0.5-1.0μm thick
Width of unpassivated regions on bias ring	$\geq 200\mu$m
Junction breakdown	> 200 V
Micro-discharge breakdown	> 150 V
Coupling capacitor breakdown	> 100 V
Total detector current at 150V	$< 4\mu$A
Interstrip capacitance	< 1.2 pf/cm

Table 1.4: Specifications for some of the SiD sensor parameters.

in any sublayer is in the tail of the Landau distribution, the generation of a δ-electron is assumed. The charge is propagated to the CCD surface according to the diffusion density functions, and charge signals in the central pixel, as well as in neighboring ones are found. The electronics noise is then added, and the ADC digitization algorithm is applied. The resulting ADC outputs for all pixels in the CCD are fed to the cluster finding routine, which finds clusters of pixels and the coordinates of their centers. Different algorithms may be used for coordinate finding. For the current studies a charge weighted average clustering algorithm is used. It should be noted that, although the name of the package implies simulation of CCDs, the package is rather versatile. By changing the parameters of the simulated sensor and by setting appropriate depletion depth and bias voltage, other types of silicon sensors can be simulated.

In a second, more detailed simulation package, the parameterization of the diffusion and

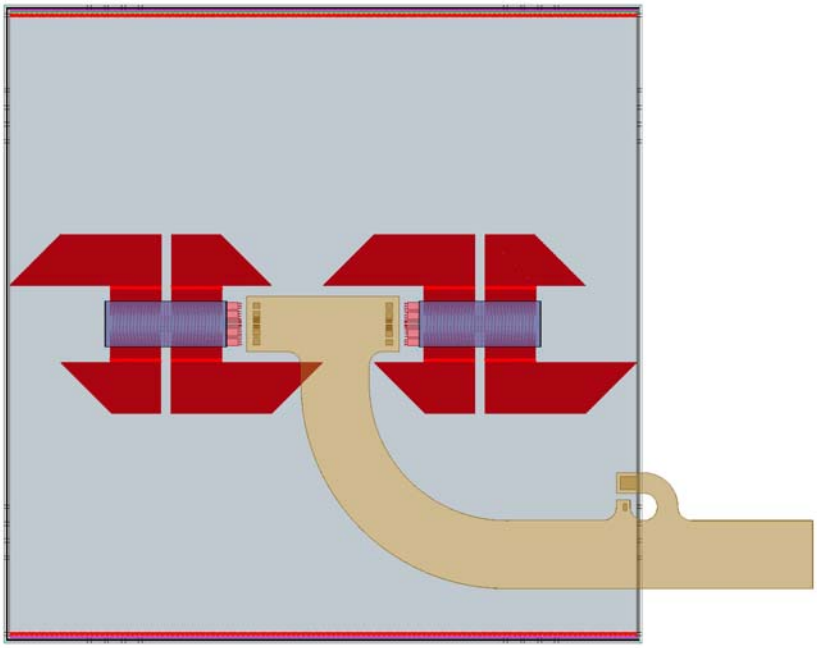

Figure 1.13: An x-ray view showing the details of the sensor readout chain for tracker modules.

the approximation of the Landau distribution has been eliminated. This package simulates every ionizing collision of a relativistic charged particle travelling through the sensitive layer of silicon. Algorithms and functions, developed by Hans Bichsel, were used to simulate interaction points and the energy losses of such collisions. If the energy loss exceeds a few keV, the generation of a δ-electron is assumed. If it is not a δ-electron, all electron-hole pairs generated in this collision are assumed to originate at the collision point. If it is a δ-electron, a random vector is generated for its direction and the path length of its trace is taken from a range table for low energy electrons in silicon. For each electron or hole, depending of the type of signal generating carriers in the given sensor, the drift and diffusion in the sensor volume is simulated. Electric and magnetic maps are used to simulate the path of each single carrier. The sensor geometry description defines the regions where carriers are collected. These simulation studies not only provide the signal amplitude in each pixel, but also the signal shape and time of the charge collection.

Detailed simulation takes a lot of computing resources. To enable physics benchmark studies, lookup tables are used, which tabulate the probability for each pixel to collect charge as function of the impact point inside the pixel under consideration or in a neighboring pixels. When using lookup tables, the timing of the charge collection is also simulated, though it is less accurate than in the case of the detailed simulation of carriers propagation. In addition to the probabilities of the carriers generated at a given space point to be collected by given pixel, the average time of such collection is also tabulated. This information can then be used at a later stage to generate the distribution of arrival time for carriers from given point inside a pixel. The shape of the distribution may change, however, depending on the electric field map and a correction may need to be applied based on the detailed simulation.

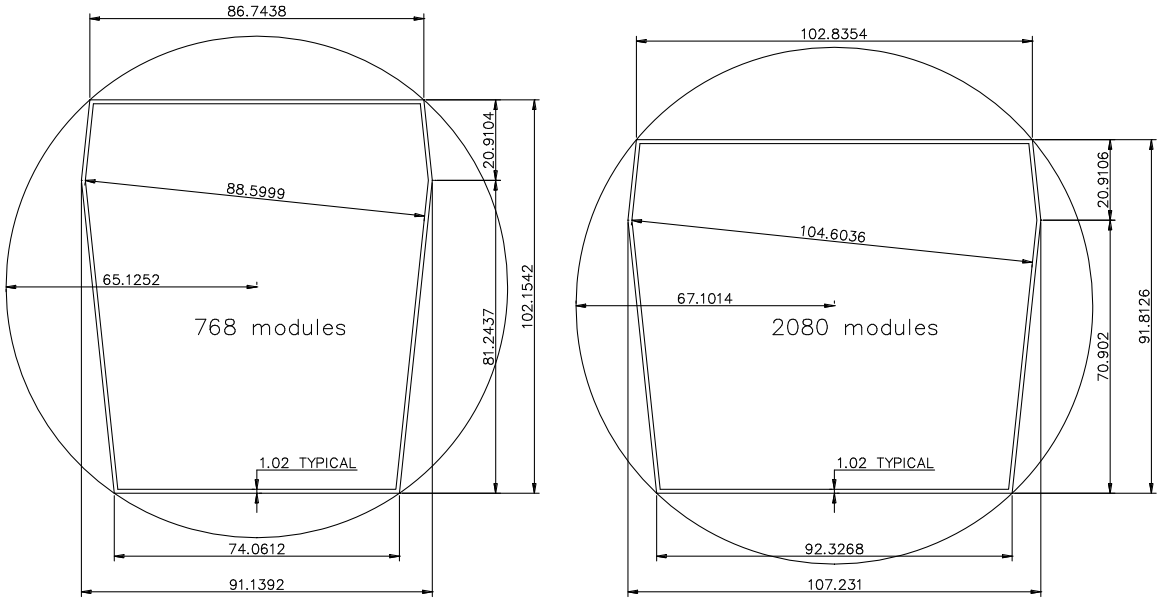

Figure 1.14: A proposed pair of sensor designs for the endcap modules of the SiD tracker. Strips are parallel to one of the long edges of each sensor. Placed back-to-back around a support frame, they create a stereo pair. The sensor and module design details are essentially identical to the barrel prototypes.

In addition to digitizing real particle hits, the simulation package also provides the possibility to generate fake hits from the electronics noise. Signal processing for different technologies may be different and the simulation can use amplitude and time information as appropriate.

1.1.8 Tracker Hit Digitization

The requirements for digitization of hits in the microstrip sensors of the tracker are somewhat different than for the thin pixel sensors of the vertex detector. Above about 100 μm in thickness, there is no need to simulate straggling effects or drift each charge carrier generated in the silicon individually. In addition, recent versions of Geant4 do an excellent job of simulating the charge deposition and generating δ-rays in these layers, simplifying the simulation of charge deposition at reconstruction time considerably.

Two different strategies are used for digitization of hits in the outer tracker depending upon the geometry being simulated. For the cylindrical geometries used in physics benchmarking a "virtual segmentation" is performed to divide the cylinder into individual tiles that are roughly the same size as single modules. In this case, the deposited charge is calculated directly from the energy deposition generated by Geant4 and the location of the charge deposition is smeared according to a Gaussian in the measured coordinate. The length of a hypothetical strip located at that coordinate is calculated in order to constrain tracks in the unmeasured coordinate.

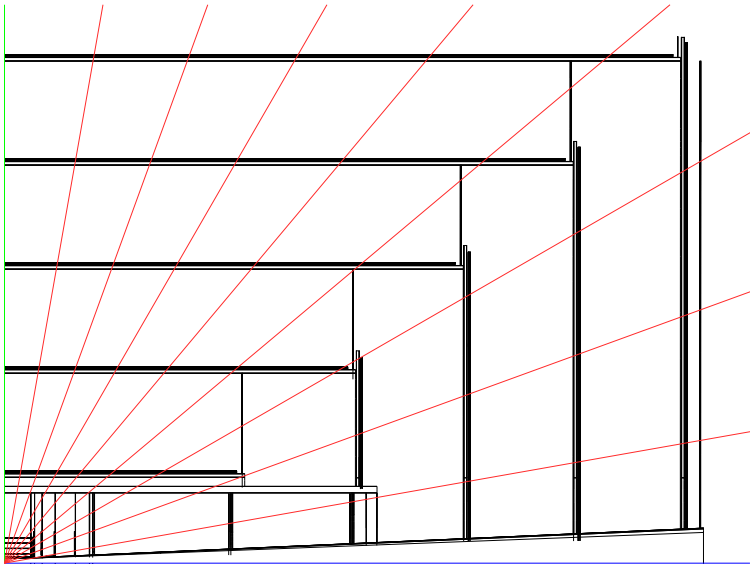

Figure 1.15: R-z view of the simplified tracking system as implemented in SiD02.

In the more realistic detector model with individual planar sensors, a more sophisticated charge deposition and digitization package is used to accurately simulate the hits that would be produced in the real detector. This model is used for more detailed tracking studies to optimize the design and validate the underlying tracking performance of the simplified digitization and detector geometry used for physics benchmarking. There are three components of this full digitization package for the outer tracker: charge generation and deposition, response of the readout system, and clustering of hits into measurements.

The charge is generated according to the energy deposition by Geant4 with small range cuts (a few μm) and step sizes (of order 50 μm) to produce an accurate description of the spatial distribution of the generated charge. The paths along which charge is generated are then subdivided into pieces no longer than a few microns, and the cloud of charge from each piece is drifted to the surface of the sensor according to the applied electric and magnetic fields including diffusion effects. At the surface of the sensor, the Gaussian-distributed cloud of charge is integrated onto the detailed pattern of electrodes from all of the hits in an event. The charge is then transferred from the sense strips to the AC-coupled readout strips according to the ratio of the coupling capacitance to the total capacitance of each sense node. This is important to accurately estimate the charge collection efficiency of the "intermediate strips" between each strip that is instrumented with a KPiX channel. A complete register-level model of the KPiX chip has been implemented to convert the charge on each readout strip to a digital signal: this is critical to understanding the impact of KPiX design decisions on the performance of the tracker, which sits at the small-signal extreme of the palette of KPiX applications. The simulation of KPiX includes full modeling of the noise of each readout node according to its capacitance, and Gaussian noise is added to all strips that will be detectable given the clustering algorithm being used. Clusters are seeded with channels above some threshold, typically four standard deviations of noise above the pedestal, and channels above

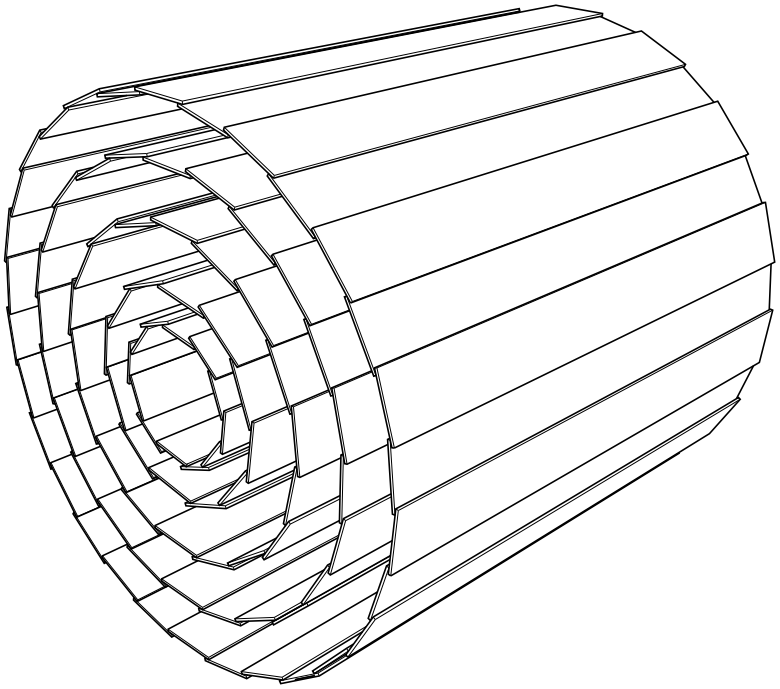

Figure 1.16: The central vertex detector showing the layout of the silicon pixel sensor modules.

some lower threshold, typically two standard deviations of noise above pedestal, are added to complete the clustering of each hit. The measured coordinate of clusters with three or fewer strips is taken as the charge-weighted centroid of those strips, while the charge on interior strips of longer clusters is first averaged over all of the interior strips to minimize the degradation of cluster position due to fluctuations in energy deposition and noise for tracks that cross the silicon at shallow incidence angles. The length of a hypothetical strip at the charge-weighted centroid is used to constrain the non-measured coordinate. Fig. 1.18 shows the hits resulting from this simulation in the double-sided endcap modules of the SiD tracker. Hits in green trace their parentage to generated Monte Carlo particles while those in purple result from readout noise.

1.1.9 Track Reconstruction

The standard pattern recognition algorithm developed by SiD is designed to efficiently find tracks using pixel and strip hits in the tracker. The pattern recognition algorithm treats the tracker as a single integrated device that is "agnostic" as to the origin of the hits (pixel or strip, barrel or endcap). This approach provides uniform pattern recognition throughout the tracking volume, effortlessly handling transitions between the different parts of the detector. Typically, 6-7 hits are sufficient for finding a track, which allows the standard pattern recognition algorithm to efficiently track particles originating near the interaction point with $p_T > 200$ MeV.

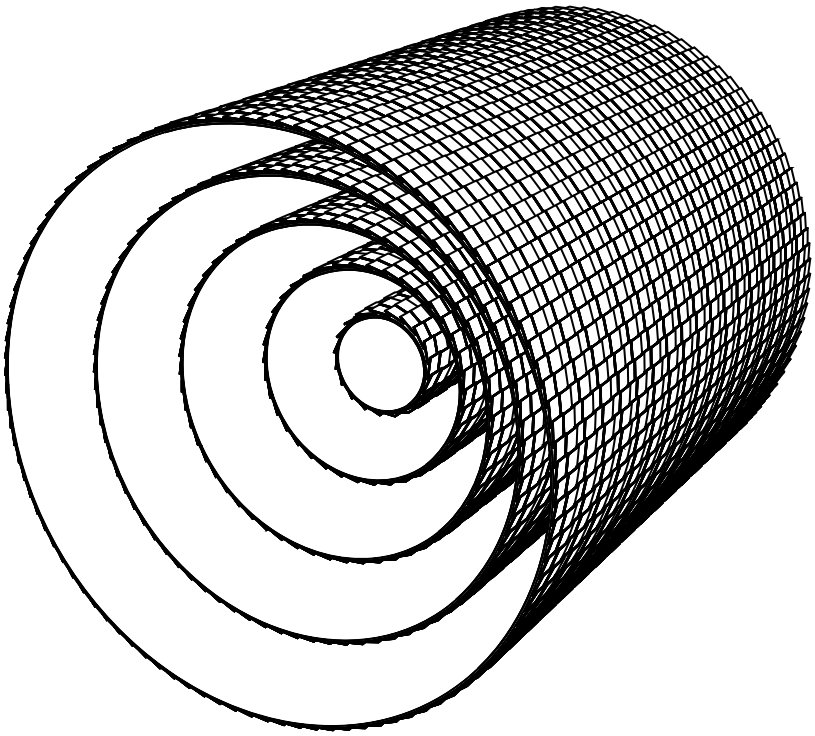

Figure 1.17: The central tracker showing support barrels tiled with overlapping readout modules.

Since pattern recognition is of utmost importance in a sparse hit environment, additional track finding algorithms are explored. Of particular note is the calorimeter assisted track finder, which uses the tracking capability of the electromagnetic calorimeter to associate hits in the outer tracker with calorimeter "track stubs". Calorimeter assisted tracking is particularly well suited to reconstructing tracks that originate outside the vertex detector, as often occurs in K_s and Λ decays. Both the standard pattern recognition and calorimeter assisted tracking algorithm are described below.

1.1.9.1 Standard Pattern Recognition Algorithm

The standard pattern recognition algorithm is explicitly designed for the task of optimizing the design of an all-silicon tracker. Variations in tracker geometry and layout can be easily studied with no change to the software. The algorithm bases all its decisions on a global χ^2. A high level of user control over the tracking "strategies" is available if desired, but more typically a "strategy builder" tool is used to automate the process of developing an optimized set of strategies for a given detector configuration.

The first step in track finding is to convert the digitized hits into a common hit format. This format encapsulates all the information needed by the standard pattern recognition algorithm, while insulating the track finding from differences and changes in the digitization

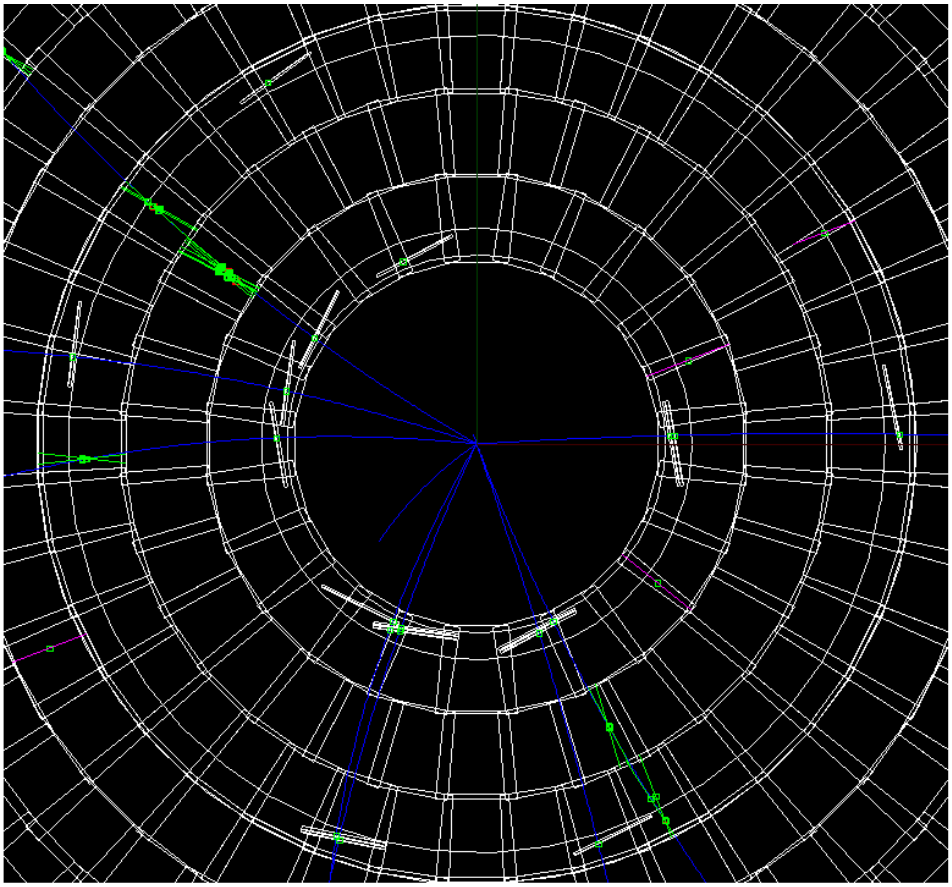

Figure 1.18: Hit pattern in the tracker disks.

algorithms.

Three types of hits are supported: pixel hits that have two measured coordinates, axial strip hits that have one measured coordinate and one bounded coordinate, and stereo hits formed from a pair of strip hits. The pixel and stereo hits may be associated with either barrel or disk geometries, while the axial strip hits have the bounded coordinate parallel to the beam axis and are intrinsically associated with barrel geometries. One further limitation is placed on stereo hits: the planes of the two strip sensors must be parallel to each other.

Track finding is controlled by a set of strategies. A strategy consists of the list of detector layers to be used, the role of each layer (seed, confirm, or extend), kinematic constraints (p_T, impact parameters), requirements on the number of hits, and the χ^2 cut. Multiple strategies can be processed by the track finding algorithm, and the resulting tracks are the collection of all distinct tracks found. The set of strategies is contained in an *xml* file that is easily understood and can be viewed/edited with a text editor.

The track finding algorithm is exhaustive in the sense that all combinations of hits that could potentially lead to a successful track fit are considered. The algorithm proceeds in four steps:

1. The first step is to form a 3-hit track seed candidate by taking all 3-hit combinations possible among the 3 seed layers. A helix fit is performed on the seed candidate, and those seeds that fail the χ^2 cut are eliminated.

2. The second step tries to "confirm" the seed by adding additional hit(s) from the confirm layer(s). A helix fit is performed on the new seeds and those that fail the χ^2 cut are eliminated. Typically, it is found that good performance is achieved with one confirmation layer.

3. The third step seeks to "extend" a confirmed seed by trying to add additional hits from the extend layers. Each time a new hit is considered, a helix fit is performed and the hit is discarded if it fails the χ^2 cut. If no hits in a given extend layer give a satisfactory helix fit, then the original track seed is kept and the next extend layer is tried.

4. Track seeds that meet the strategy's requirement on the minimum number of hits are merged to form a list of distinct tracks. Two track candidates are allowed to share a single hit, but if a track candidate shares more than one hit with another candidate, an arbitration scheme is used to select the better candidate. Precedence is given to the candidate with the greatest number of hits, while the candidate with smaller χ^2 is selected when the number of hits is equal.

Consistency checks and hit sorting algorithms are used to minimize the number of helix fits performed, substantially improving the performance of the algorithm. Furthermore, a "bad hit χ^2" cut is used to identify track candidates with an outlier hit and allows preference to be given to track candidates without an outlier hit.

A key component of the pattern recognition algorithm is a fast helix fitter. The helix fitter takes as input 3 or more tracker hits. The hits can be any combination of pixel, axial strip, or stereo hits in the barrel and/or endcap detectors. The fitter is the one place in the tracking code that distinguishes between the various types of hits. The fast fitter is used to estimate the helix parameters and helix fit χ^2. First, a circle fit to the x,y coordinates of all hits is performed using the Karimäki algorithm to determine the helix parameters ω, ϕ_0, and d_0. If there are two or more pixel/stereo hits, then a line fit in the $s-z$ plane is used to determine the z_0 and $\tan\lambda$ helix parameters. In order to provide full helix fits for the case where there are fewer than two pixel/stereo hits, a new fitting algorithm was developed.

While an axial strip does not measure the z coordinate, it has well defined bounds that impose the constraint $z_{min} < z < z_{max}$. These bounds lead to each axial strip having an allowed band in the z_0-$\tan\lambda$ plane. For two or more axial strips, the intersection of these bands will produce a polygonal allowed region, the centroid of which is taken to be the measured values for z_0 and $\tan\lambda$. If there is no region of intersection, the hits are inconsistent with being from a helix and the fit fails. For the case of a single pixel/stereo hit, the pixel/stereo hit is treated like a very short strip and the above algorithm is used.

For all but the highest momentum particles, the multiple scattering errors will exceed the intrinsic hit resolution. Multiple scattering errors for both the active and dead materials are estimated and included in the helix fit. Correlations in the multiple scattering errors are ignored, leading to an under-estimate of the helix parameter errors by a factor of ≈ 1.5.

For stereo hits, full account is taken for the separation between the two stereo layers in the calculation of both the hit position and hit covariance matrix.

The performance of the standard pattern recognition algorithm is shown in the section on tracker performance and is also reflected in the benchmarking studies. Unless otherwise noted, the tracking strategies require 1 confirmation hit, a total of at least 7 hits (6 hits for barrel-only tracks), $p_T > 0.2$ GeV, xy distance of closest approach $d_0 < 10$ mm, and distance of closest approach along the beam direction $z_0 < 10$ mm.

1.1.9.2 Calorimeter-Assisted Tracking

The development of the calorimeter assisted track finding algorithm was primarily motivated by the need to reconstruct non-prompt tracks and long-lived particles in the SiD detector. As will be shown later, the standard track finding algorithm achieves excellent efficiency in reconstructing prompt tracks that originate close to the interaction point. However, using the same algorithm for finding non-prompt tracks is difficult because those tracks often do not produce enough hits in the vertex detector to seed the track finder, and creating seeds from 3-hit combinations in outer layers without limiting combinatorics by constraining the track origin to the interaction region can be problematic.

The calorimeter assisted tracking solves the problem by seeding the track finder from traces left by charged particles in the electromagnetic calorimeter - so called MIP stubs. The standard SiD track finder is run first, and the found tracks are then propagated through the calorimeter. Clusters are created and attached to the tracks. After that, topological clustering is applied to the remaining calorimeter hits. Those of the created clusters that include hits in inner electromagnetic calorimeter layers are analyzed for consistency with being produced by minimum ionizing particles. Clusters that pass the test are converted into track seeds that contain information about the track position and direction at the calorimeter entry point. Depending on the MIP stub quality, the seed can also contain a track curvature estimate. The seeds are propagated back into the tracker, picking up hits that are not attached to any existing tracks. The search window in each tracker layer is calculated based on the trajectory parameters uncertainties, and the track parameters are re-evaluated after attaching every new hit. If more than one hit can be attached to the track in a certain layer, multiple track candidates are created. Once all seeds have been processed, the newly created tracks are rated based on quality, and duplicates are removed. This algorithm is essential for reconstructing all kinds of non-prompt tracks - K_s^0 and Λ decay products, new physics signatures that might include long-lived particles, kinked tracks, and calorimeter backscatters. It also performs high purity, topologically linked initial clustering in the calorimeter, and associates clusters with tracks.

1.1.9.3 Track Fitting

The track fitting results presented here use the fast helix finder described before. Two more precise approaches to track fitting have been developed by SiD. The first of these is based on a track fitting algorithm originally used by SLD and used in previous studies of the

performance of the SiD tracking system. It solves minimization equations for χ^2, calculated from the matrix of residual weights. This weight matrix takes into account multiple scattering derived from the amount of material passed by a track, correlations between track deviations in the subsequent detector layers and independent measurement errors due to the sensors spatial resolution. Solving the matrix equation for 5 track parameters gives the parameter values corresponding to the best fit; the inverse of the weight matrix of the parameters gives the covariance matrix of parameter errors. Comparison of the expected parameter errors derived from the covariance matrix with real track parameter residual distributions shows agreement to within a few percent. This fitter may be slow for a large number of layers, as it requires a matrix inversion with a matrix dimension equal to the number of layers. For the SiD concept, however, it works fine as total number of layers crossed by a track rarely exceeds 10. A Kalman filter, which treats multiple scattering close to optimally, is under development and updated results using that Kalman filter will be presented at a later time. The Kalman filter will be used as a final fitter to refit tracks that are currently fitted by the simple fitter.

1.1.10 Tracking Performance

In this section the performance of the vertex and tracking detector will be described, along with its associated track-parameter fitter. The goal of these studies is to evaluate the overall performance of the SiD tracking system with the most realistic simulation available. The standard tracking algorithm was tuned for the benchmark processing to find tracks having $p_T > 0.2$ GeV that originate from near the interaction region. The strategies used generally required at least 7 hits to be associated with a track. An additional strategy that required 6 barrel hits in the vertex detector and first layer of the outer tracker was put in place to provide low-p_T coverage for central tracks that may not pass through 7 different layers before curling back around. Additionally, for the benchmark processing the strategies placed a 1 cm constraint on the x-y and z distances of closest approach.

We can break down tracking efficiency into two parts: (1) the fraction of Monte Carlo charged particles that are in principle "findable" given the set of strategies used, and (2) the track reconstruction efficiency for the findable tracks. The starting point for the tracking efficiency measurement is the set of long-lived charged particles identified as being "final state particles" by the event generator. Final state particles include short-lived particle decay products (e.g. $\pi^{\pm}$ from $K_S \to \pi^+\pi^-$), but does not include long-lived particle decay products (e.g. $\pi^{\pm}$ decay products) or secondaries produced by GEANT as the result of interactions in the detector.

Among the final state particles in $e^+e^- \to t\bar{t}$ collisions at $\sqrt{s} = 500$ GeV, 6.5% of the tracks are below the 0.2 GeV p_T cutoff in the standard tracking algorithm. Of the tracks satisfying the p_T constraint, 9.1% of the tracks have fewer than 6 hits, which is the minimum number of hits for the standard tracking algorithm. Some of these tracks are from sources, such as K_s decay, that are potentially recoverable by the calorimeter assisted tracking algorithm. Findable tracks must also satisfy the requirements for having seed and confirmation hits and satisfy the 1 cm constraint on the x-y (d_0) and z (z_0) distances of closest approach. Taken together, 84.4% of the final state particles are findable by the standard

Selection	Selection Efficiency	Cumulative Efficiency
All Tracks	-	100%
$p_T \geq 0.2$ GeV	$(93.54 \pm 0.11)\%$	$(93.54 \pm 0.11)\%$
$N_{hit} \geq 6$	$(90.91 \pm 0.13)\%$	$(85.04 \pm 0.16)\%$
Seed Hits Present	$(99.78 \pm 0.02)\%$	$(84.85 \pm 0.17)\%$
Confirm Hit Present	$(99.95 \pm 0.01)\%$	$(84.84 \pm 0.17)\%$
$\lvert d_0 \rvert \leq 1$ cm	$(99.80 \pm 0.02)\%$	$(84.65 \pm 0.17)\%$
$\lvert z_0 \rvert \leq 1$ cm	$(99.69 \pm 0.03)\%$	$(84.39 \pm 0.17)\%$
Track Reconstruction	$(99.32 \pm 0.04)\%$	$(83.81 \pm 0.17)\%$

Table 1.5: Fraction of findable tracks

tracking algorithm. The breakdown of these contributions to the findable track efficiency can be found in Table 1.5.

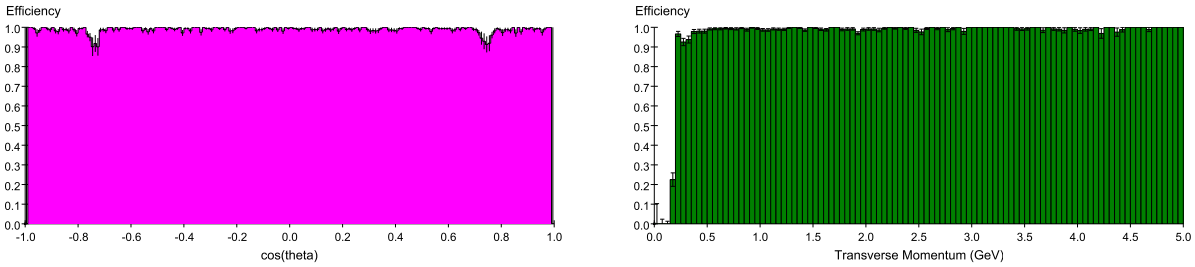

Figure 1.19: Track finding efficiency as a function of track $\cos\vartheta$ (left) and p_T (right).

The track reconstruction efficiency measures the fraction of findable tracks that are found by the standard tracking algorithm. Using the sample described above, the track reconstruction efficiency is found to be 99.3%. Fig. 1.19 shows the efficiency as a function of $\cos\vartheta$ and p_T. The track finding efficiency drops in the transition region between barrels and disks. Fig. 1.20 shows the efficiency as function of $\cos\vartheta$ for two p_T bins. The left plot is for tracks with $p_T < 500$ MeV and the right plot is for tracks with $p_T > 500$ MeV. All the inefficiency is due to low momentum tracks in this transition region. It is thought that the inefficiency is due to tracks just beyond the pixel barrel acceptance that curl by more than 180 degrees before they get to the seed layers that cover this acceptance region. As such, this may be an artifact of the current tracking algorithm and could be improved upon.

Tracking algorithms must balance track finding efficiency against the probability of finding "fake tracks" that are not associated with a Monte Carlo particle. A key indicator for the number of fake tracks is the number of mis-assigned hits on a track. These hits are generated by a different Monte Carlo particle than the one with the preponderance of hits on the track. More than 99% of tracks have at most one wrong hit on the track, as seen from Fig. 1.21. Fake tracks, where no single Monte Carlo particle is responsible for the majority of hits, make up only 0.07% of the tracks found.

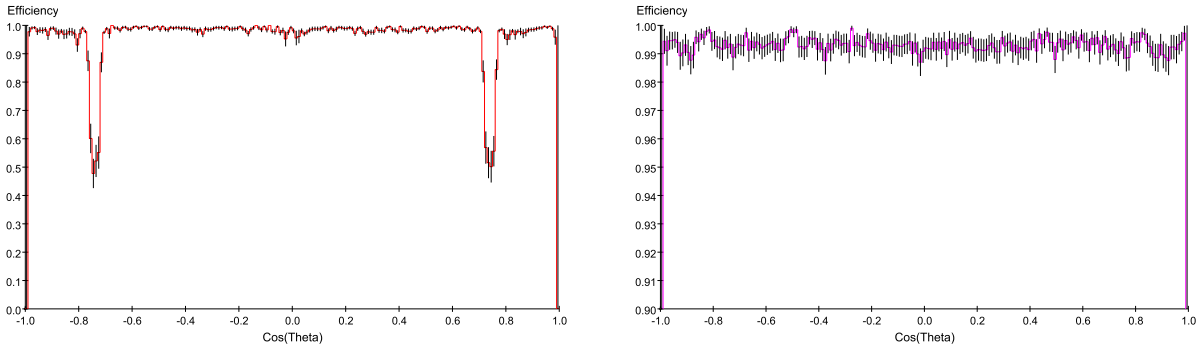

Figure 1.20: Track finding efficiency as a function of track $\cos\vartheta$ for tracks with $p_T < 500$ MeV (left) and $p_T > 500$ MeV (right). Please note the different vertical scales in the two figures.

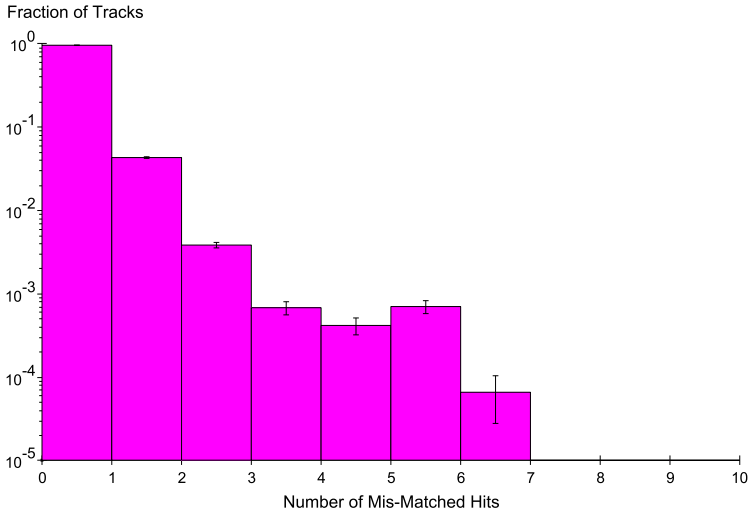

Figure 1.21: Fraction of tracks versus the number of mis-assigned hits.

The momentum resolution of the tracker is shown in the top plot in Fig. 1.22 as a function of momentum for various track angles. The bottom figure shows the impact parameter resolution for various track angles. An impact parameter resolution of 4 μm is obtained in the high momentum limit.

How the tracking performs in higher occupancy environments is summarized in Fig. 1.23. Two studies have been carried out. First, the performance of the track finder has been studied in the environment of dense jets. The plot in the upper left corner in Fig. 1.23 shows the track finding efficiency as function of the angle between the track and the jet thrust axis for $e^+e^- \to q\overline{q}$ events at $\sqrt{s} = 1$ TeV. The efficiency holds up rather well, dropping by about 1% for tracks within 2mrad of the jet core. The distribution in α, the angle of charged particles with respect to the jet thrust axis, is shown in the upper right corner in Fig. 1.23. The bottom figure shows the track finding efficiency as a function of track p_T for $e^+e^- \to b\overline{b}$ events at $\sqrt{s} = 500$ GeV with the backgrounds from 10 bunch crossings overlaid. In this

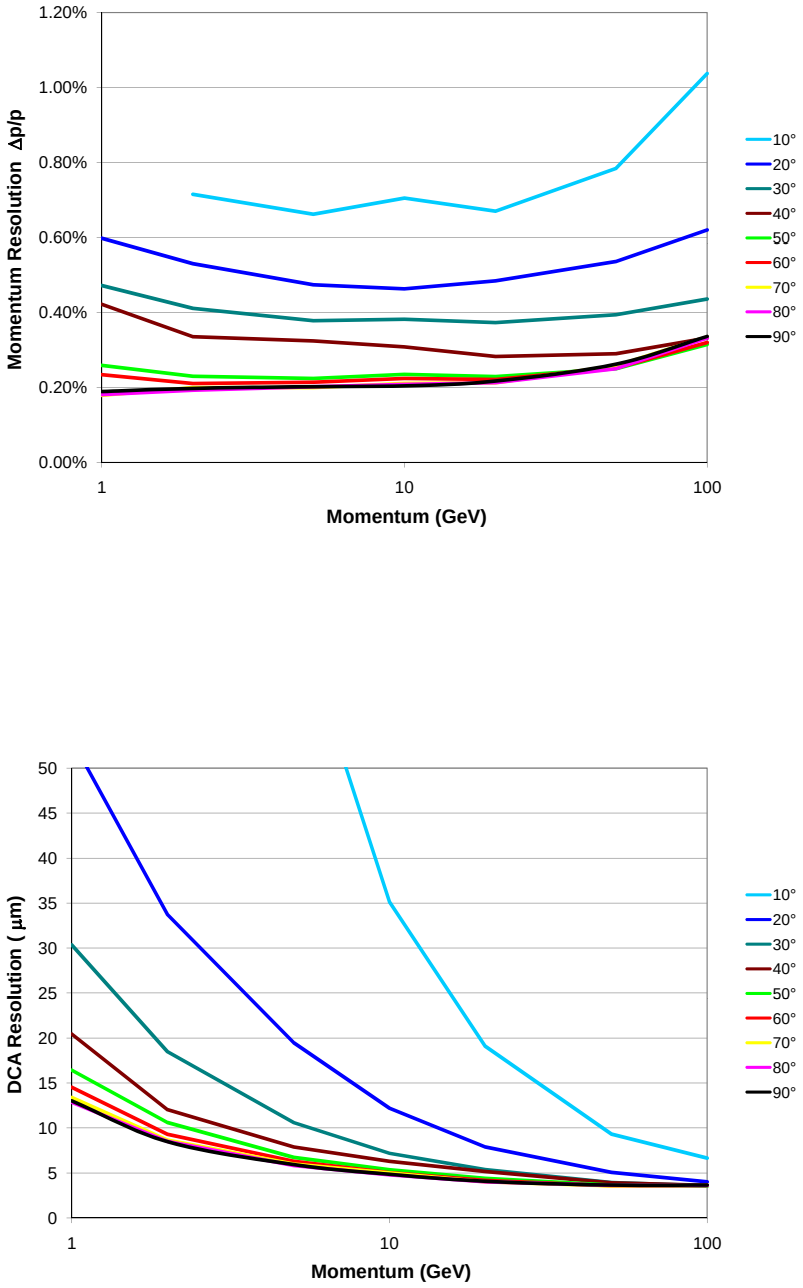

Figure 1.22: Resolution in momentum (top) and $r - \varphi$ distance of closest approach, DCA (bottom), as function of track momentum at various angles.

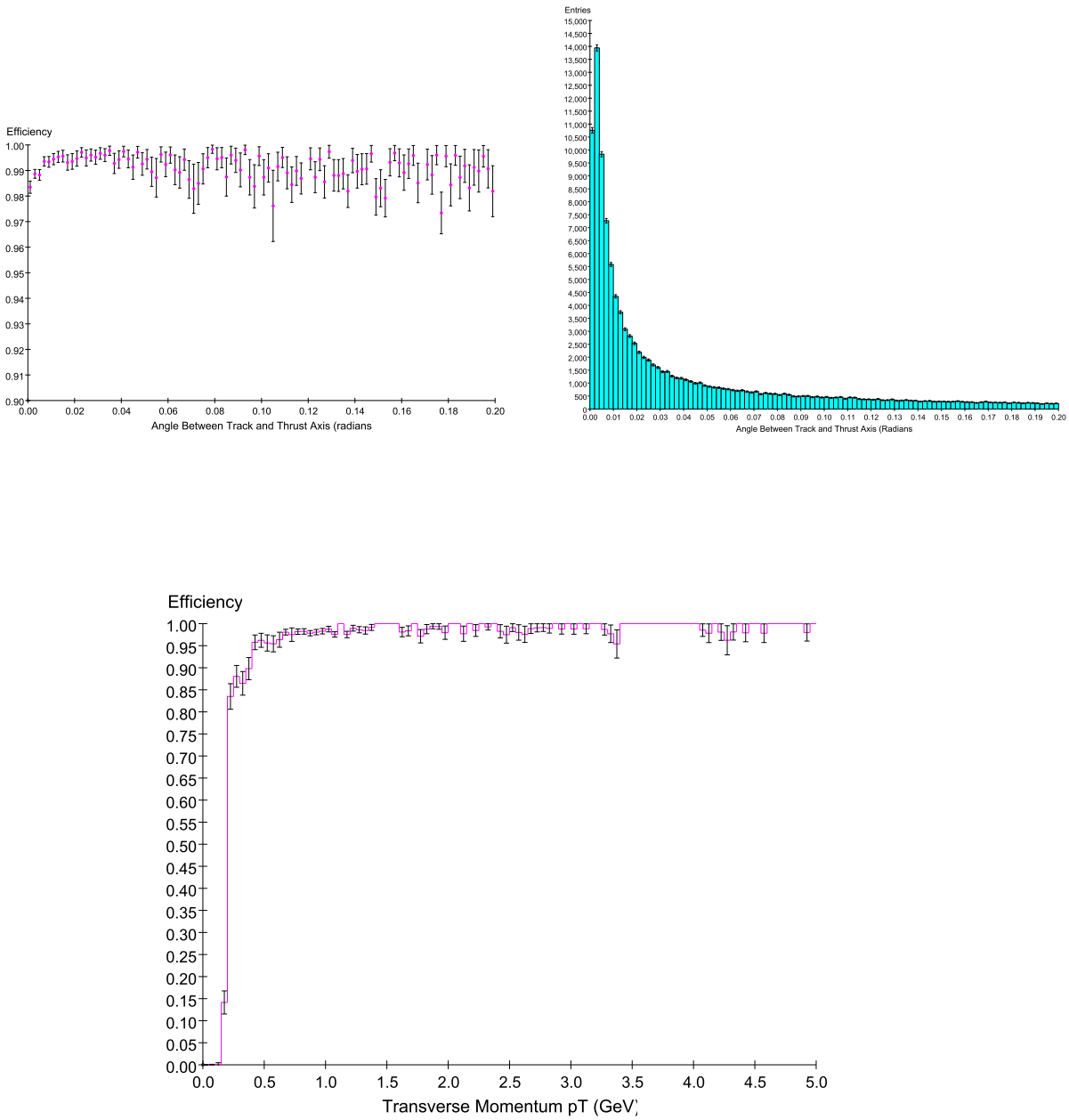

Figure 1.23: Tracking efficiency as function of α (upper left) and distribution in α (upper right) for $e^+e^- \to q\overline{q}$ events at $\sqrt{s} = 1$ TeV. The bottom figure shows the tracking efficiency for $e^+e^- \to b\overline{b}$ events at $\sqrt{s} = 500$ GeV with the background from 10 bunch crossings overlaid.

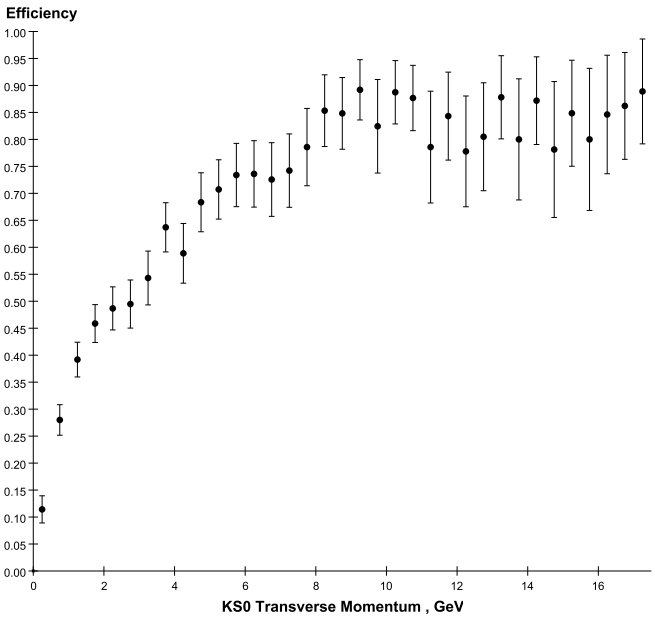

Figure 1.24: K_s^0 finding efficiency as function of its transverse momentum.

study the effect of accumulating beam backgrounds over 10 crossings has been mimicked by adding these hits to all pixel devices in the detector. Hits in the silicon strip tracker were added only for a single bunch crossing, in-time of course with the physics event. There is a small loss in efficiency at low p_T, as anticipated. Also the fake track rate is higher, about 0.6%. Most of the fake tracks seem to be due to combinatorics.

An often-voiced concern of a tracker with relatively few measurements on a charged particle trajectory is the efficiency for the reconstruction of long-lived particles. The SiD detector should be viewed as an integrated detector where the overall performance derives from a combination of all the subdetectors. As described in section 1.1.9.2 a calorimeter assisted track finding algorithm was developed to reconstruct non-prompt tracks and long-lived particles. Fig. 1.24 shows the K_s^0 reconstruction efficiency for $t\bar{t}$-events, obtained by running the standard tracking algorithm followed by the calorimeter assisted tracking algorithm. The efficiency is defined as the ratio of the number of successfully reconstructed K_s^0's to the total number of K_s^0's that decayed into a charged pion pair inside the third layer of the outer tracker. The efficiency reaches 85% for K_s^0's with transverse momenta above 8 GeV. The result represents the current status of the software and significant improvements, particularly for low momentum K_s^0, are anticipated.

All the simulations are performed using a uniform 5 Tesla magnetic field with no radial component. ANSYS simulations of the solenoid and the return flux show that the field is not uniform. Fig. 1.25 shows the distribution inside the tracking volume of the longitudinal (left) and radial (right) component of the magnetic field. The SiD detector having a 5 T magnetic field is defined as the field at $(R, z) = (0, 0)$ being 5 T. In Fig. 1.25 B_z is given as fraction of the nominal 5 T field. In the center of the detector B_z increases slightly with increasing

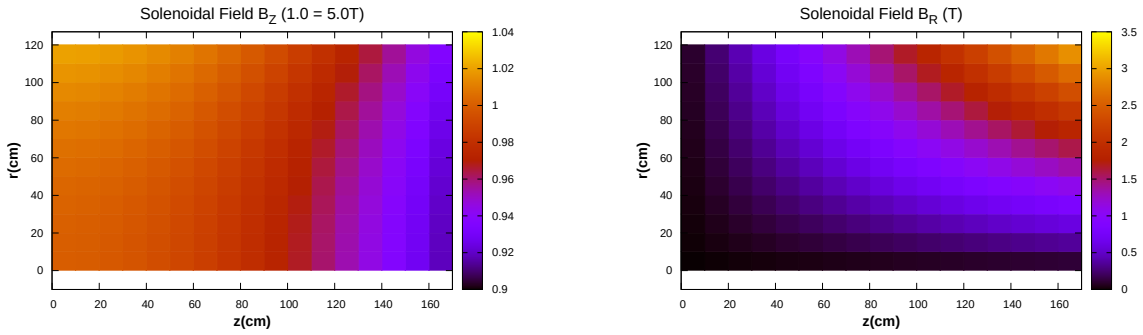

Figure 1.25: Map of the magnetic field components inside the tracking volume: B_z in fractional deviation from the nominal magnetic field (left) and B_R in absolute values (right)

radius. There is a drop of about 6% when reaching the end of the tracker volume. The field component B_R, given in absolute values in Fig. 1.25, is not negligible. The effect of a non-uniform magnetic field was studied by simulating particle trajectories with the field map as shown in Fig. 1.25 and reconstructing the trajectories assuming a perfect uniform field configuration. Preliminary studies indicate the effect on the pattern recognition to be minor. Studies are ongoing to investigate how it affects the fitted track parameters and whether the field uniformity must be improved.

1.1.11 Tracker Alignment

The unprecedented track momentum resolution contemplated for linear collider detectors demands minimizing systematic uncertainties in sub-detector relative alignments. At the same time, there is a strong impetus to minimize the amount of material in the tracking system, which might compromise its stability. These two requirements put a premium on accurate alignment of the various elements of the tracker. The short time scales on which alignment could change (e.g., from beam-driven temperature fluctuations) may preclude reliance on traditional alignment schemes based on detected tracks, where it is assumed the alignment drifts slowly, if at all, during the time required to accumulate sufficient statistics.

The prospect of two ILC detectors swapping places in the beamline only increases the importance of *in situ* alignment monitoring that does not depend on tracks. It will be important to monitor tracker distortions during the push-pull operations, not only for later track reconstruction, but also to ensure that no damage-inducing stresses are inadvertently applied to the tracker components. Alignment systems that can also be used during tracker assembly to monitor strains would also be useful.

A system that can monitor alignment drifts in real time would be highly desirable in any precise tracker and probably essential to an aggressive, low-material silicon tracker. The tradeoff one would make in the future between low material budget and rigidity will depend critically upon what a feasible alignment system permits. The SiD tracker is considering two

alignment methods, one based on Frequency Scanned Interferometry (FSI), and one based on Infrared Transparent Silicon Sensors (IRSS).

The FSI system incorporates multiple interferometers fed by optical fibers from the same laser sources, where the laser frequency is scanned and fringes counted, to obtain a set of absolute lengths. With a test apparatus the state of the art in precision DC distance measurements over distance scales of a meter under laboratory-controlled conditions has been reached and even extended. Precisions better than 100 nm have been attained using a single tunable laser when environmental conditions are carefully controlled. Precisions under uncontrolled conditions (e.g., air currents, temperature fluctuations) were, however, an order of magnitude worse with the single laser measurements.

Hence a dual-laser FSI system is foreseen for the tracker, that employs optical choppers to alternate the beams introduced to the interferometer by the optical fibers. By using lasers that scan over the same wavelength range but in opposite directions during the same short time interval, major systematic uncertainties can be eliminated. Bench tests have achieved a precision of 200 nm under highly unfavorable conditions using the dual-laser scanning technique. Fig. 1.26 shows an example of dual-laser fringes measured on a benchtop single-channel prototype system.

It should be noted that complementary analysis techniques of FSI data can be used either to minimize sensitivity to vibrations in order to determine accurate mean shape distortion or to maximize sensitivity to vibrations below the Nyquist frequency of data sampling. The latter algorithm could prove especially useful in commissioning in assessing vibration effects, such as might arise from pulse powering in a magnetic field.

The second method exploits the fact that silicon sensors have a weak absorption of infrared (IR) light. Consecutive layers of silicon sensors are traversed by IR laser beams which play the role of infinite momentum tracks (see Fig. 1.27). Then the same sophisticated alignment algorithms as employed for track alignment with real particles can be applied to achieve relative alignment between modules to better than a few microns. This method employs the tracking sensors themselves, with only a minor modifcation to make them highly transparent to infrared light. Only the aluminum metalization on the back of the sensor needs to be swept away in a circular window with a diameter of few millimeters to allow the IR beam to pass through. Since IR light produces a measurable signal in the silicon bulk, there is no need for any extra readout electronics.

A key parameter to understand the ultimate resolution of this method is the transmittance of a silicon sensor and the diffraction of the light. As a first approximation a silicon sensor is viewed as a stack of perfectly homogeneous plano-parallel layers, each characterized by its index of refraction and thickness. The layers are, however, not continuous but present local features, so that diffraction phenomena will appear if the size of the obstacle is comparable to the wavelength used. For instance, the strips of the detector with 50 μm readout pitch, are good examples of an optical diffraction grating for an incoming beam in the IR. It has been determined that a key parameter that determines the overall transmittance of a microstrip detector is the pitch to strip ratio, that is, the fraction of the strip covered by aluminum. The smaller the strip width, the more light is transmitted. It was determined that good transmittance was achieved when the strip width was set to 10% of the pitch.

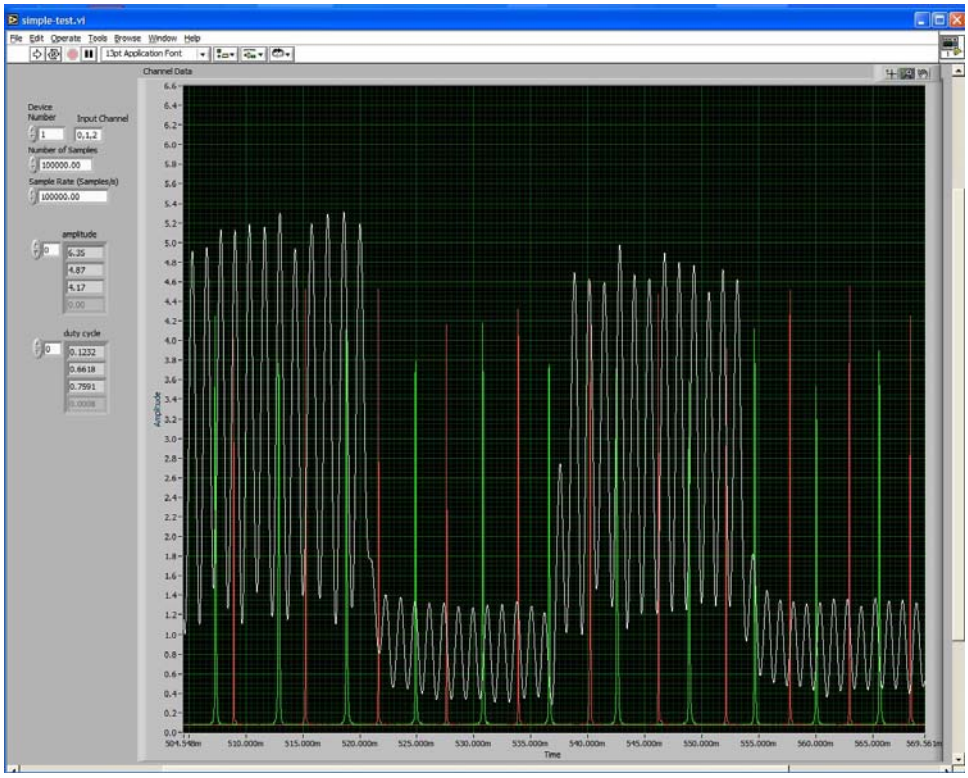

Figure 1.26: Example of FSI fringe display for a single-channel FSI system. White peaks indicate interference fringes, while red and green peaks are Fabry-Perot transmission maxima from a chopped, dual-laser system.

Tuning of sensor thickness was found to contribute up to 5% over the layout optimized value. In bench tests, based on CMS strip detectors, a relative alignment of a few microns has been achieved.

It should be noted that this alignment method has been implemented at the Alpha Magnetic Spectrometer (AMS) and has been by the tracking system of the Compact Muon Solenoid experiment. Furthermore, both methods, developed for central and forward tracker alignment, may also prove useful for the vertex detector.

1.1.12 R&D

1.1.12.1 Sensor Technology

Sensor technology is sensitive to the state of the art in microelectronics. Given the rapid advances in this field, we feel that the choice of vertex detector technology can and should be delayed until either one technology is demonstrated to be superior, or a choice is imposed by the installation schedule for the detector. We note that the detector is physically small and the SiD design allows for installation and service of detector assemblies during shutdowns. The danger with this approach is that it does not allow for early consideration of system

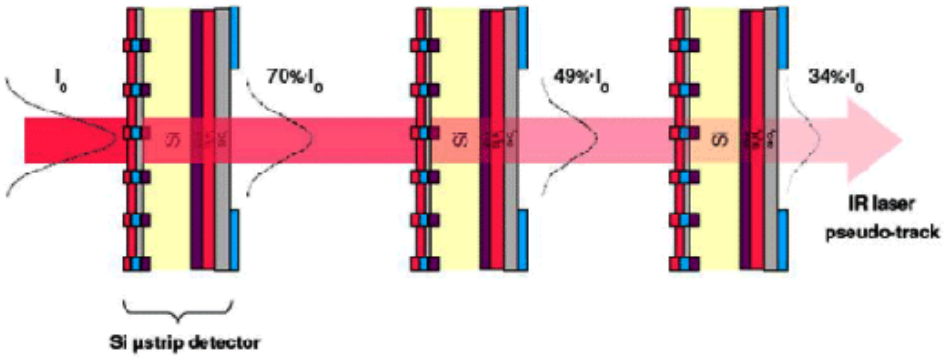

Figure 1.27: Sketch of the IR alignment method.

design aspects that depend on sensor technology. It also requires support of sensor R&D on a rather broad front.

Candidate technologies sensor technologies include:

- CMOS MAPS - Monolithic active pixel sensor where signal charge is produced in the $\approx$ 10 micron thick epitaxial layer available in many standard CMOS processes and collected in an implanted well.
- Charge Coupled Device (CCD) - based technologies
  - ISIS - CCD/CMOS hybrid device where good time resolution and reduction of instantaneous power is achieved by in-pixel storage of multiple CCD raw charge samples.
  - Fine Pixel CCD - CCD with pixel size of about 5 microns. These fine pixels would provide enhanced ability to discriminate MIPS from pairs generated at the IP.
  - Short column CCD - time resolution is achieved by pairing the shared charge in adjacent columns shifted in opposite directions.
- DEPFET - Provides in-pixel storage and amplification of charge using a transistor (DEPFET) integrated on the sensor which serves as both the charge collecting and amplifying node.
- SOI - Uses the substrate in a monolithic Silicon-on-Insulator device as sensor with the

top silicon providing readout electronics. Vias are placed in the buried oxide insulator layer to access the signal charge produced in the bulk silicon "handle".

- 3D - Uses vertical integration of electronics to increase in-pixel functionality and to integrate sensors and ICs. This provides the ability to provide complex electronics and fine pitch pixels without extremely small feature size.

Table 1.6 summarizes some (but not all) of the leading candidate sensor technologies. Some are more easily adapted to fine time resolution which could accommodate smaller detector radii and higher machine backgrounds. Others have advantages for mechanical assembly or power consumption. R&D efforts are focussed on addressing the challenges associated with each technology. We note that the ISIS effort, which provides relatively uniform power dissipation during the inter-train period, has recently been discontinued in the UK.

1.1.12.2 Power

Power distribution and engineering is a crucial part of the vertex design. Air cooling is essential to minimize the mass of the detector. A practical air cooling system limits the heat load in the central barrel to about 20 Watts. This can be achieved in some technologies by pulsing the power applied to the front-end circuitry. Given the 200:1 duty factor of the beam, and assuming that 100:1 can practically be achieved for pulsed powering, this implies a 2,000 Watt peak load for the central barrel. With electronics operating at 1.5 V this implies peak currents of 1333 A. The conductor needed to carry this current with acceptable voltage drop is too massive. To reduce the mass we expect to employ either a serial powering or DC-DC conversion scheme to allow high voltage, low current power delivery.

Work on these technologies has just started.

Fermilab, Penn and RAL have developed the Serial Power Interface (SPi) ASIC, which will enable the testing of pulsed serially powered systems.

The SPi was developed for both SLHC and ILC applications. The chip has two linear and one shunt regulator each with the ability to control the output voltage levels via a control lines, allowing

for a pulsed power mode. We also expect to benefit from work for super-LHC, which will need a high voltage power delivery scheme to keep the size and mass of the

cable plant within acceptable bounds.

Early DC-DC converter prototypes from CMS with air-core inductors show acceptable EMI only when shielded. The mass of these devices is about 0.02 radiation lengths.

The tradeoff between bulkier, higher mass DC-DC systems and serially powered systems which do not naturally have balanced currents and are therefore more susceptible to Lorentz forces needs to be studied. Pulsed powering is unique to ILC, and work to understand the electrical and mechanical impact of power pulsing will be a high priority for most SiD subsystems.

	CMOS MAPS	ISIS CCD	DEPFET	SOI	3D
Advantages	Available technology, moderate in-pixel complexity	EMI resistant, uniform power utilization	Low power, demonstrated functionality	Low noise, large signal, monolithic design	High in-pixel functionality, large S/N, good time resolution
Challenges	Charge collection by diffusion, parasitic collection by PMOS	Time resolution set by in-pixel samples	Limited time resolution, need for auxiliary chips	Back gate effects on transistors limit V_{bias}	Yield of integrated structure
R&D Focus	Complex in-pixel functions, S/N, time resolution	Integration of CMOS and CCD technology	Speed of RS readout, system design	Transistor backgate, commercial availability	Technology demonstration, commercial availability
Readout schemes studied	RS, CP, PS, TS	PS	CP	RS, PS	TS
Form factor	Reticle	Reticle	Full ladder	Reticle	Full ladder
R&D Projects	Mimosa, LDRD, FAPS, CAP, SRD0, Chronopixel	ISIS	DEPFET	LDRD-SOI, CAP5	VIP1,2

Table 1.6: Summary of the characteristics of some candidate vertex sensor technologies. In the Readout Scheme row RS=Rolling Shutter, CP=Column Parallel, PS=Pipelined Storage, TS=Time Stamp.

1.1.12.3 Outer Tracker

The ILC experiments demand tracking systems unlike any previously envisioned. In addition to efficient and robust track-finding over the full solid angle, the momentum resolution required to enable precision physics at ILC energies must improve significantly beyond that of previous trackers. The design must minimize material in front of the calorimeter that might compromise particle-flow jet reconstruction. Establishing and maintaining the alignment for the tracker is critical. Even with the largest feasible magnetic field, the tracking volume is quite large, demanding optimized tracker components which facilitate mass production. Finally, the tracker must be robust against beam-related accidents and aging. All these requirements must be maintained within a "push-pull" scenario.

The emphasis in the area of the tracking detector is currently on the development of the double-metal sensor with the associated readout. These sensors need to work in a 5 T magnetic field and remain stable and aligned during power pulsing. The forward tracker design must be optimized. A small scale system consisting of a few sensors with full readout will be tested in a test beam under these operating conditions. Only then can issues associated with the Lorentz forces and mechanical stability be tested.

PROJECT DESCRIPTION and STATUS REPORT

Development of a Digital Hadron Calorimeter for the Linear Collider Using Gas Electron Multiplier Technology

Personnel and Institution

J. Yu, A. White, S. Park, J. Smith, M. Sosebee, A. Brandt and K. De
University of Texas at Arlington

Collaborators

R. de Oliveira, CERN, Geneva, Switzerland
C. Hahn and W. J. Kim, Changwon National University, Changwon, South Korea
Peter Fisher, Ulrich Becker, Ray Cowan, Massachussetts Institute of Technology, Boston
A. Breskin, Weizmann Institute, Israel

Project Leaders

A. White, J. Yu

Project Overview

The precision measurements of physics topics at the International Linear Collider demand unprecedented energy resolution of jets. The Particle Flow Algorithm (PFA) [1] approach is a solution that could be used to achieve such a jet energy resolution. In order to take full advantage of a PFA, it is of critical importance to minimize contributions to the energy resolution due to confusion in track-energy cluster match. Accomplishing this requires a calorimeter that can provide excellent matching between energy clusters and tracks whose momenta are measured in the tracking detector. This means small cell size and fine readout granularity. Reading out in such a high granularity in analog mode could make the cost of the calorimeter prohibitively high. One bit readout per cell would reduce the total number of digital bits dramatically and thus provide the possibility of reducing the cost for readout electronics. However, we will also discuss analog readout later in the context of the SLAC KPiX chip.

Gas Electron Multiplier (GEM) [2, 3] is a detector technology which can be used in a high granularity calorimeter. Over the past several years the University of Texas at Arlington (UTA) team and collaborators from the other institutions listed have been developing a digital hadronic calorimeter (DHCAL) [4 – 6] using GEM as the sensitive gap detector technology. DHCAL is a solution for allowing PFA to be used in precision jet energy measurement. GEM can provide flexible configurations which allow small anode pads for high granularity. It is robust and fast with only a few nano-second rise time, and has a short recovery time which allows higher rate capability than other detectors, such as a resistive plate chamber (RPC) [7, 8]. It operates at a relatively low voltage across the amplification layer, can provide high gain using a simple gas ($ArCO_2$) which protects the detector from long term issues, and is stable.

The ionization signal from charged tracks passing through the drift section of the active layer is amplified using a double GEM layer structure. The amplified charge is collected at the anode layer with 1cm×1cm pads at zero volts. The potential differences,

required to guide the ionization electrons, are produced by a resistor network, with successive connections to the cathode, both sides of each GEM foil, and the anode layer. The pad signal is amplified, discriminated, and a digital output produced. GEM design allows a high degree of flexibility with, for instance, possibilities for microstrips for precision tracking layer(s), variable pad sizes, and optional initial ganging of pads for eventual finer granularity future readout if required and allowed by cost considerations. Figure 1.(a) depicts how the double GEM approach can be incorporated into a DHCAL scheme.

Results of Initial GEM Studies

Initial studies were conducted on signal characteristics and gain from a small prototype GEM detector shown in Fig. 1.(b). The signals from the chamber were read out using the QPA02 chip originally developed by Fermilab for Silicon Strip Detectors. The gain of the chamber was determined to be of the order 3,500, for a 70% Ar/30% CO_2 mixture, consistent with measurements by the CERN GDD group. The MIP efficiency was measured to be 94.6% for a 40 mV threshold, which agrees with a simulation of chamber performance. The corresponding hit multiplicity for the same threshold was measured to be 1.27, which will be beneficial for track following and cluster definition in a final calorimeter system. A gas mixture of 80% Ar/20% CO_2 has been shown to work well and give an increase in gain of a factor of 3 over the 70% Ar/30% CO_2 mixture. A minimum MIP signal size of 10 fC and an average size of 50 fC were observed from the use of this new mixture. The prototype system has proved very stable in operation over many months, even after deliberate disassembly and rebuilding, returning always to the same measured characteristics. We investigated cross talk properties using the nine $1\,\text{cm}\times1\,\text{cm}$ cell anode pad layout shown in Fig.1(c). We used collimated gamma rays from a ^{137}Cs source to study signal sharing between adjacent pads.

Beam and Source Test Results

As the first step toward building the full-size (1m×1m) test beam chamber, we developed 30cm×30cm GEM foils together with Microinterconnect Systems Division of 3M Corporation. A foil is divided into 12 independent HV strips for operational safety (we had to disconnect a few strips during beam test experiments). For mechanical

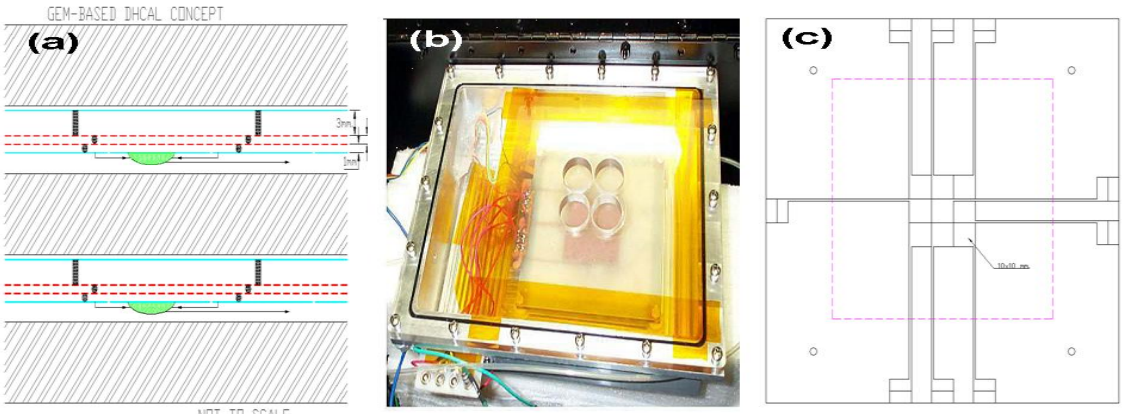

Figure 1. (a) GEM DHCAL concept diagram (b) UTA GEM prototype chamber constructed with $10\,\text{cm}\times10\,\text{cm}$ CERN GDD GEM foils (c) Prototype readout anode pad with nine $1\,\text{cm}\times1\,\text{cm}$ cells

assembly, we have developed tools to handle large area foils, maintaining flatness of the foils and the detector walls that provide gas and HV feed-through. We constructed several prototype chambers using these foils and a readout board with 1cm×1cm pads, and exposed them in various particle beams. These chambers were read out using the 32-channel QPA02 chip-based Fermilab preamp cards.

We conducted three beam tests to measure the rate capability of the chamber, its MIP characteristics, cross talk between the channels, and occupancy. The output signals from the amplifier cards were sent to discriminator boards which contain discriminator chips, multiplexer stages, and data output interface. The output from the discriminator boards were read out by a PCI based ADLink ADC controlled by LabView software.

The first beam exposure of our 30cm×30cm prototype chamber took place in May 2006 at a high flux beam which consists of 30 ps pulses of 10^{10} electrons every 43 μs in 5 cm radius. The detector and the electronics measured responses to 10^{9} electrons per pad. The chamber was able to see the beam clearly and provided a good measure of the time structure of the beam. Additionally, as a test, we directly exposed a broken GEM foil to the beam. In both the chamber and the broken GEM foil, we did not see any physical damage. In addition, while the signal shapes were distorted by the hits from 10^{9} electrons per pad, the chamber responded well to such a large signal, giving us confidence that the chamber will function well in the ILC environment.

Additional beam tests were conducted at Fermilab's Meson Test Beam Facility (MTBF) [11] in April 2007. We tested a single multi-channel chamber using a 100 channel readout system. Most the useful data was taken using 120 GeV proton beams from the Main Injector. LabView-based online analysis software complimented the DAQ software and allowed us to monitor the data as they were accumulated. Since the DAQ card required a long signal for efficient sampling, we developed a pulse shaper to stretch the signal to a suitable level for the ADLink DAQ card to sample. We also used a commercial shaper for verification purposes.

The trigger was formed of coincidences of three 1cm×1cm and two 19cm×19cm counters to constrain the beam to an area smaller than 1cm×1cm, which was the size of a readout pad. The two 19cm×19cm counters enveloped the GEM prototype chamber to ensure beam passage through the active area of the detector. In addition to the beam trigger, we employed two additional triggers: chamber self trigger with the signal above 30mV, utilizing the negative output from Fermilab QPA02 preamplifier, and the coincidence between the five counters and a pad signal above 30mV to constrain the beam on a particular target pad.

Using the data collected in the MTBF beam tests, we were able to determine relative efficiencies and fractional cross talk ratios. In order to verify the proper functionality of the chamber, we took data using a high intensity Sr^{90} radioactive beta source. Fig. 2.(a) shows the signal without noise subtraction (blue), noise (purple) and noise subtracted signal (red) when 120GeV proton beam is incident on the target pad. The noise subtracted signal distribution demonstrates a Landau shape as expected. Fig. 2.(c) shows the relative efficiency measured on this pad as a function of threshold, which demonstrates that the efficiency is about 98% at 40mV. However, it should be noted that a sizable number of events have more than one proton entering the detector within the 200ns gate. This is the apparent reason why we observed differences in the widths between the noise subtracted signal distributions from the source and proton beams

respectively. An initial estimate of the multiple proton events shows about 20% multiple proton event contamination. A more detailed analysis using the differences between the data obtained from the Sr^{90} source and the proton beams is being finalized.

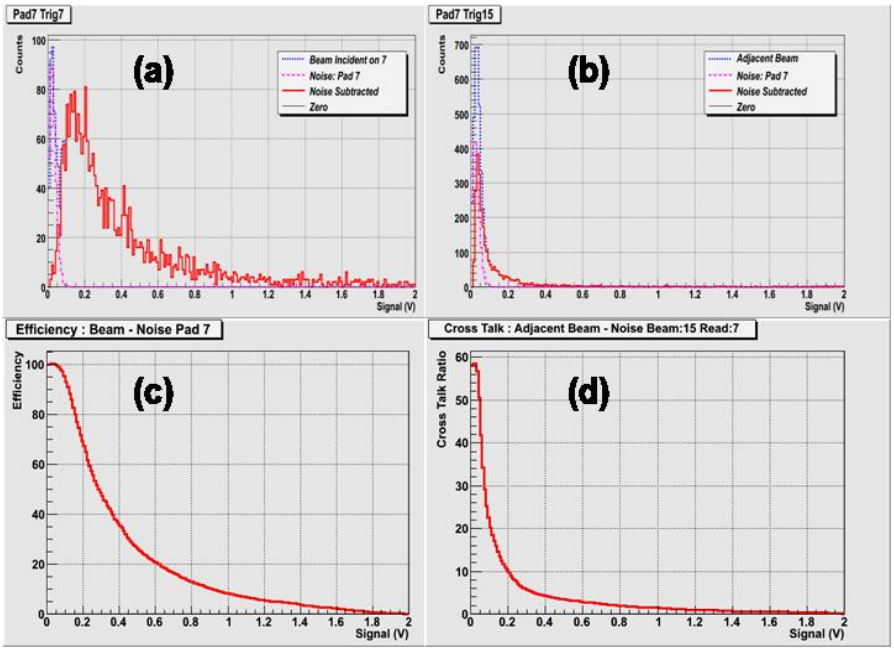

Figure 2. Signal from 120GeV proton (blue), noise (purple) and the noise subtracted beam (red) distributions (a) when the beam is incident to the pad and (b) when the beam is incident to the neighboring pad (c) Relative efficiency (d) % fractional cross talk ratio

In order to measure the cross talk rate, we read out the pad immediately next to the trigger pad. Fig. 2.(b) shows the pulse height distributions of the pad number 7 when beam was incident on an immediate neighboring pad. Blue dotted lines represent the signal before noise subtraction, the purple lines represent noise, and the red line is the noise subtracted signal. The difference between the two cases is apparent from the two figures. From these, we can extract the fractional cross talk rate on a pad, as shown in Fig.2.(d). From these studies, while the probability of the cross talk is small for both the pads, it should be emphasized that given the size of the trigger paddle this distribution includes charge sharing between the neighboring pads and the multiple proton events. As in the cases before, a more systematic analysis is being finalized to take into account these different effects Fig. 3.(a) and 3.(c) show the responses of the two channels of the prototype chamber described above to electrons from a Sr^{90} radioactive source. Both channels show the characteristic Landau distributions expected from a gas detector. Figures 3.(b) and 3.(d) show the absolute efficiencies of the chamber for the same two channels as a function of threshold in mV. As can be seen, the chamber demonstrates efficiencies over 99% when the threshold is set at 30mV which is equivalent to 4 fC.

Multichannel Readout of GEM DHCAL Using KPiX

As the next phase, for a full chamber characterization using a multiple channel readout system, we have been working with the high density analog readout system, KPiX which is being developed at SLAC, and is described in detail in Ref. [12]. As described later in this proposal, we plan to conduct further beam tests using KPiX once we complete integrating the chip with our GEM chambers and fully characterize its behavior in bench tests. The KPiX readout chip was originally developed for silicon-tungsten (Si/W) electromagnetic calorimeter (ECAL) [13, 14]. The chip has been modified to include a switchable gain to accommodate small signals from a GEM chamber. KPiX is being considered as the standard front-end readout device for most of the major SiD [15] subsystems. It offers a 4 event deep pipeline, with a 13-bit Wilkinson ADC on each channel. A decision, based on a combination of hardware tests, PFA studies and costs, will be taken later about the final use of KPiX for the hadron calorimeter.

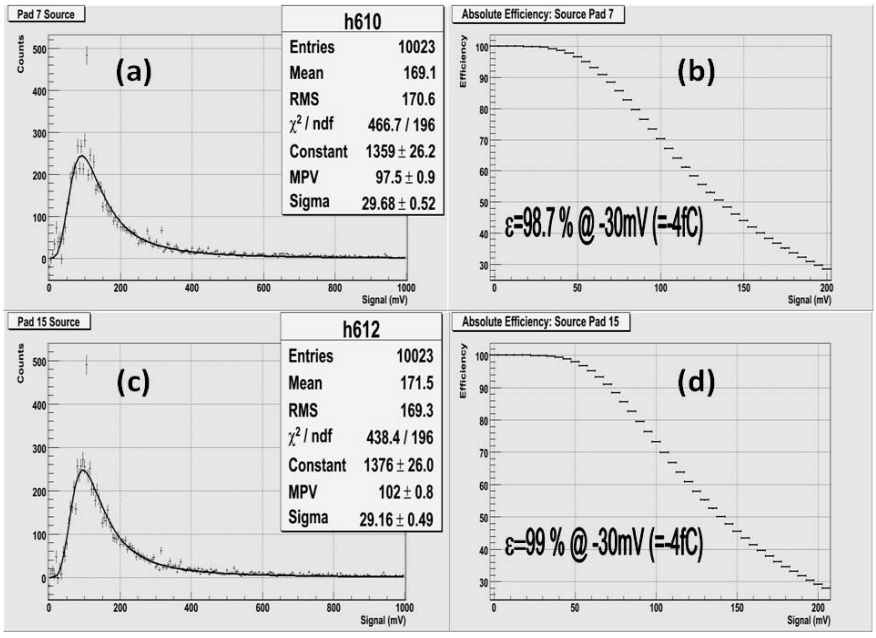

Figure 3. (a) and (c) responses of two channels to Sr90 source in mV; (b) and (d) Absolute efficiencies of the same two channels as a function of threshold in mV

The first study we performed was the characterization of the calibration parameters of the KPiX v4 chip with a GEM chamber. For this study, we took calibration data hourly for 19 hours and 24 hours on two different days to see if there are day – night and weekday – weekend effects. This was to fully understand whether there are environmental effects that would impact our measurements with KPiX v4 in our labs. We observed that the mean values of any given KPiX v4 channels do not show any systematic day – night dependence or weekday – weekend dependence. The fluctuation in pedestal mean value for each channel is within 3 – 5%. We, however, observed the mean values of the pedestal vary between 20 and 130 ADC counts channel to channel, as shown in Fig.4.(a). We also observed that the channel to channel variations of the gains vary 5 – 20 ADC counts/fC, as shown in Fig.4.(b). This channel to channel gain variation has been reduced by a factor of two in the newest version of the KPiX chip (v7). These observations have been communicated to SLAC team, and we anticipate the next generations of the chip will have far less variations.

Fig. 4.(c) shows the signal read out from the GEM chamber with the KPiX chip from a channel right under the source. As can be seen, the plot shows a large pedestal peak

near 0 fC with the long tail that signifies the signal from Sr^{90} source. Since this version of the KPiX chip was designed specifically to work in the International Linear

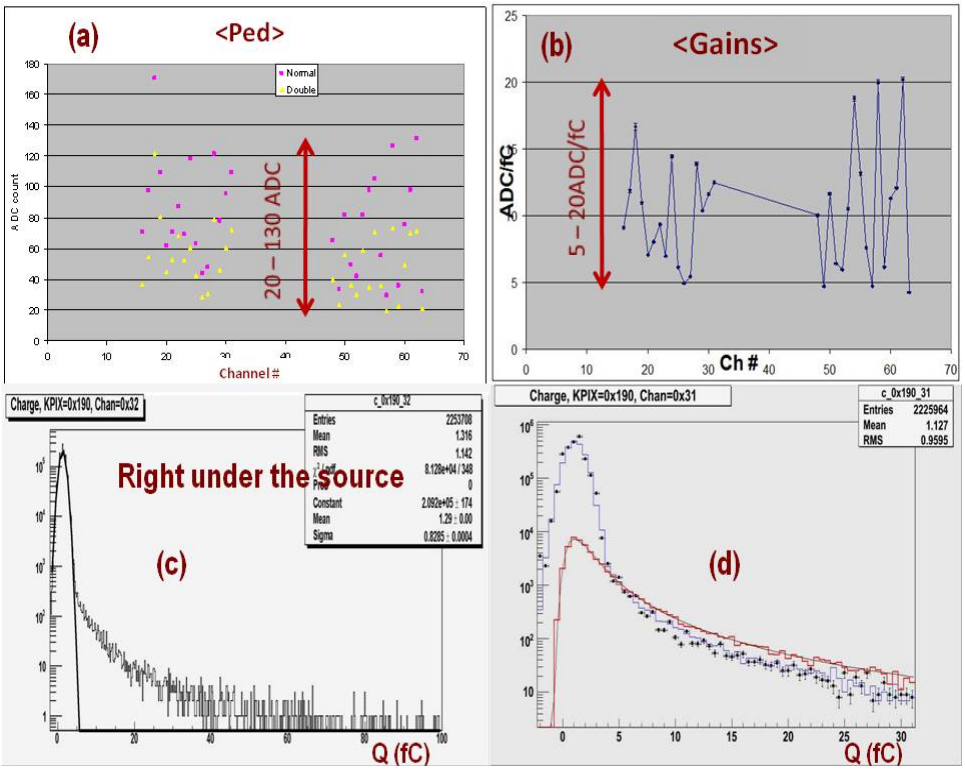

Figure 4. (a) The pedestal mean value vs channel number (b) Mean value of the electronics gain vs channel number (c) Mean pedestal subtracted and electronics gain corrected charge distribution from Sr90 source run (d) Extracted charge distribution from the GEM chamber (red) from the inference method using the simulation (blue) and its description of the data (solid circles). The good distribution of the data from the simulation demonstrates that the extracted signal represents the chamber responses well.

Collider (ILC) operational mode, its trigger is synchronized to the ILC accelerator clock which is expected to send the signal of beam arrival ahead of collisions. Due to this feature of the chip's triggering scheme and to the fact that we took data with Sr^{90} source which emits low energy electrons that are difficult to trigger, the readout chip ran in a periodic reset mode that integrates the charge in regular intervals independent of the existence of the actual charge in the chamber.

In order to extract the charge distributions from Fig.4.(c), we developed an inference method based on simple simulation of the KPiX charge integration scheme, the actual pedestal distribution of the channels from previous calibration runs, the simulated pulse shape of the minimum-ionizing particle and the charge distributions from the previous beam test measurements. We simulated the KPiX charge integration within a fixed amount of time (333ns – the ILC beam crossing interval) starting randomly with respect to the signal pulse. We then let the normalization of the Gaussian pedestal distributions and the most probable value and the width of the charge distributions float until the resulting output charge distribution describes the data distribution well. Fig.4.(d) shows the data from the channel under the source in solid circle, the final simulation results in blue histogram and the extracted GEM chamber response in red histogram. As can be seen, the fact that the form of the data is well described by the simulation gives us confidence that the extracted chamber response is real.

We, however, noticed that the most probable value of the extracted GEM chamber response is 1.9fC which is about a factor of 10 smaller than what we observed in previous source and beam tests. Upon detailed investigation of the chamber structure, which was to give flexibility in modification of the chamber for KPiX v4, it was determined that this does not provide an adequate level of gas in the active volume of the chamber since the structure imposes a large resistance to the gas diffusion; thus most of the gas flows following the direction around the active chamber volume. As a result, when we took the source data, the charged particles traversing through the detector volume did not produce sufficiently large amounts of ionization. Given this feature, we modified the chamber so that the gas is forced to be directly injected into the active volume and diffuse out to the remaining volume of the chamber through tubing laid within the chamber active volume.

We took cosmic ray data to make sure that the chamber is producing sufficiently large signals and have indeed observed the expected size signals from the chamber. We are now working on integrating this new chamber with the new version (v7) of KPiX chip (KPiX7). We are in the process of characterizing the new version of the KPiX chip and are taking cosmic ray and source data to fully characterize the chamber with KPiX v7 chip.

Summary of Project Status

The UTA HEP group has made significant progress using the 30cm×30cm GEM foils developed in collaboration with the 3M Inc. We have been working on integrating the GEM chamber with the KPiX analog readout chip. We have characterized the previous version (v4) of the KPiX together with a GEM chamber and extracted the signal from a Sr^{90} radioactive source. We are working on integrating the chamber with the latest version (v7) of the KPiX chip that allows external trigger input. We describe our plans in FY2009 – 2011 in the sections below.

FY2009 Project Activities and Deliverables

- **Full Characterization of 30cm x 30cm GEM chamber with KPiX7 Readout**

The SLAC team has provided an anode board with the new 64 channel KPiX v7 chip. This new version provides HV discharge protection as well as the capability of external trigger input which will help testing dramatically. Based on the experience from the previous version of KPiX chip, we have made a change in the gas distribution system to ensure fast gas replacement and optimal ionization and signal induction levels. Now that we have successfully observed signals from Sr^{90} radioactive sources, we are ready to take data for full characterization of our double GEM chamber prototype read out by the analog KPiX chip.

As the next step, we will construct a new 30 cm × 30 cm chamber with the optimal gas distribution and a KPiX v7 readout board. We will understand the noise characteristics of the chamber and will perform source tests. We will then take cosmic ray data for MiP characterization, noise characteristics, and cross talk, on the bench at UTA - reading out 64 channels. Once we are confident with these results, we will expose the chamber in particle beams for high statistics chamber characterization, measuring response uniformity, noise rates, cross talks, absolute efficiencies, and gains.

- **Development of 100cm x 33cm Large GEM Foils and Chambers**

We plan to construct a total of five 100 cm × 100 cm GEM chamber planes to demonstrate performance of GEM active layers in a hadronic calorimeter. We will be working on development of smaller unit chamber of size 100 cm × 33 cm (with 96 cm × 32 cm active area), three of which will make up one ~100 cm × 100 cm plane. While we had been working on development of 30 cm × 30 cm GEM foils successfully with the 3M Inc., they decided to close their micro-flex circuit division in late 2007. For this reason and because the CERN GDD workshop has been working on developing cost effective technology to produce large size GEM foils, we are now working with this workshop on the design of a 100 cm × 33 cm GEM foil silkscreen. The CERN GDD work shop estimates a total production time of eight weeks for the first set of 20 large GEM foils after the finalization of the silkscreen. We are currently working with CERN to finalize the design of the silkscreen that is optimal for our prototype detectors. This work is being carried out in the context of the RD51 – Micro-Pattern Gas Detector Collaboration, of which UTA is an active member (A. White is a RD51 Management Board member).

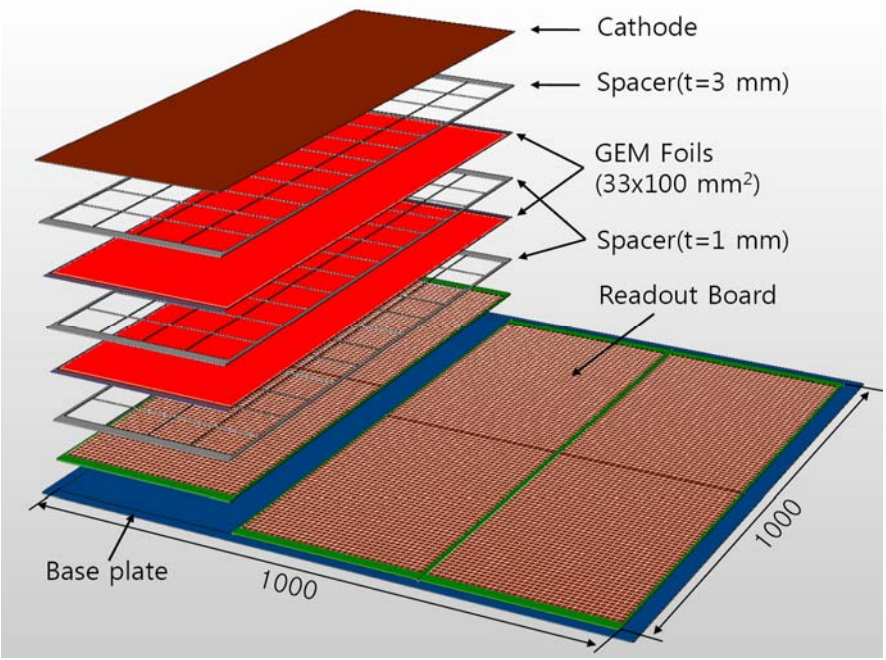

Figure 5. A schematic diagram of a $100\,cm \times 100\,cm$ double GEM detector plane. Three of unit chambers of size $100\,cm \times 33\,cm$ will be assembled on a 2mm steel plate to make up one $100\,cm \times 100\,cm$ GEM plane. The figure also shows the anode board structure where two boards $50\,cm \times 33\,cm$ make up one unit chamber.

As part of the effort for constructing $100\,cm \times 100\,cm$ GEM planes, we will work on development of mechanical structure, the electronic readout board schemes with the SLAC team, and the schemes for connecting the three unit chambers to form one $100\,cm \times 100\,cm$ detector plane. Each of the $100\,cm \times 33\,cm$ unit chambers will have $96\,cm \times 32\,cm$ active area, leaving two 1cm gaps on each of $100\,cm \times 100\,cm$ plane in between unit chambers. As shown in Fig. 5, we plan to use a 2mm thick $100\,cm \times 100\,cm$ area steel plate to assemble three of these unit chambers into one $100\,cm \times 100\,cm$ detector plane with strong mechanical support.

Once we finalize the mechanical structure for the unit chamber of size $100\,cm \times 33\,cm$, we will construct one prototype chamber using the 256 channel KPiX v8 analog readout chips, to be available by mid-2009, and a readout anode board of size $50\,cm \times 33\,cm$. We anticipate the first chamber to be ready for testing in late 2009. We will characterize the chamber and the chip using source and cosmic ray at UTA. Once the chamber is characterized on the bench, we will expose the chamber to particle beams.

- **Anode Board for 1m x 33cm GEM Unit Chamber with KPiX v8**

We have been working with the SLAC KPiX electronics team led by M. Breidenbach in using the analog system for GEM chamber signal readout. After several months of understanding the performance of the electronics with $30\,\text{cm}\times30\,\text{cm}$ GEM chambers, we will be at the point to take data using KPiX v8 readout chips. Two $50\,\text{cm}\times33\,\text{cm}$ anode boards will make up one $100\,\text{cm}\times33\,\text{cm}$ anode boards for a unit chamber. Each half anode board will be read out by six 256 channel KPiX v8 chips.

Project Activities and Deliverables Beyond FY2009

- **Completion of Construction and Characterization of 100cm x 33cm Unit Chamber**

In the case that the development of $100\,\text{cm}\times33\,\text{cm}$ unit chamber and the characterization process does not finish in FY2009, we will complete this process as part of the FY2010 activities.

- **Large Thick-GEM prototype chamber in 2010**

As an alternate, cost effective solution for regular thin GEM foils, we have been continuing to pursue the development of thick-GEM's (TGEM) [16, 17]. In addition to TGEMs that are made of normal PCBs, a new development effort has been made on Resistive Electrode TGEMs (RETGEMs) [18]. As a member of the RD51 collaboration, we are working closely with various collaborators on the development of these new TGEMs in small and large scales. In particular, we have been working with the Amos Breskin's group at the Weizmann Institute for large scale TGEM development. These TGEMs are anticipated to become available on a late 2009 or early 2010 time scale. Once TGEMs are tested and certified, we will construct and characterize a prototype chamber on the bench using 64 channel KPiX v7 or 256 channel KPiX v8 analog chips. When this completes, we plan to expose the chamber in the beam for full, high statistics characterization and for comparison of its performance with regular thin GEM chambers. We anticipate this beam test to be on an early or mid 2010 time scale.

- **Completion of Construction of five 100cm x 100cm GEM Planes and DHCAL Beam Test**

As the $100\,\text{cm}\times33\,\text{cm}$ unit chamber is being fully characterized, we will complete the mechanical design for $100\,\text{cm}\times100\text{cm}$ GEM active layer planes and construct a total of five of such planes. We will develop a procedure for mechanical construction and quality testing of the planes and will replace five of the forty RPC planes in the existing CALICE[19] calorimeter beam test stack currently located at Fermilab for beam test. The goal of this beam test is to partially measure the performance of a GEM-based DHCAL. This result should be compared to that of a DHCAL with full 40 layer RPCs and other analog HCALs to provide valuable information in overall ILC detector design choices. This beam test will be carried out using either CALICE Si/W or Scintillator/W ECAL and a tail catcher (TCMT), using the CALICE mechanical support structure.

GEM/DHCAL Beam Test Plans

In order to continue testing GEM based DHCAL, we plan for the future particle beam tests of our GEM chambers in phases as listed below.

- Phase I: Chamber characteristics
  - A prototype chamber with dimension $30\,\text{cm}\times30\,\text{cm}$ will be constructed with the 64 channel KPiX v7 analog chips being characterized at SLAC and at UTA.
  - The primary goal of the test is to exercise the newly developed and bench-characterized KPiX v7 chip in particle beams with the trigger system synchronized to the accelerator clock, and fully characterize the chamber with KPiX readout chips.
  - This test will be performed at Fermilab's MTBF in early summer 2009.
- Phase II: Unit chamber ($100\,\text{cm}\times33\,\text{cm}$) beam test
  - We will construct a total of fifteen $100\,\text{cm}\times33\,\text{cm}$ unit chambers using the CERN-developed $100\,\text{cm}\times33\,\text{cm}$ GEM foils.
  - For readout of these unit chambers, we will be using the next generation 256 channel KPiX v8 chips. Twelve of these chips will be used to readout a unit chamber, six of each mounted on $50\,\text{cm}\times33\,\text{cm}$ anode board.
  - This test will be performed at Fermilab's MTBF sometime in late 2009 – mid 2010.
  - The goal of this test is to characterize large scale unit chambers built with CERN thin GEM foils.
  - We expect to receive a few large Thick GEM (TGEM) boards in this time period. We will then build a prototype chamber and expose to particle beams for characterization. We will be using 256 channel KPiX v8 chips for this test as well.
- Phase III: Five GEM Plane DHCAL Beam Test
  - We will then construct a total of five $100\,\text{cm}\times100\,\text{cm}$ chambers, each using three unit chambers.
  - This test will be performed at Fermilab's MTBF on a late 2010 – early 2011 time scale.
  - These chambers will be inserted into the existing CALICE $1\,\text{m}^3$ calorimeter stack as part of the on-going beam testing of RPC based DHCAL.
  - The goal of this test is to partially measure the responses and resolutions of GEM-based digital hadron calorimeter along with RPC planes.
  - This full scale prototype will be tested jointly with CALICE Si/W ECAL and the NIU tail catcher (TCMT), using the CALICE mechanical support structure.

Simulation and PFA development of GEM/DHCAL in the context of SiD

During the past several years, due in part to lack of funds, we have been concentrating on hardware development, rather than both hardware and simulation. While the geometry for the GEM DHCAL layer structure has been provided and incorporated into the SiD detector overall geometry, our previous studies were conducted using an old Mokka TESLA detector geometry. Since the performance of a detector

component is only meaningful as an integral part of an overall detector, it is important for our group to obtain funds to resume the performance studies of GEM in the context of SiD, develop simulations for beam test stacks, and to actively participate in Particle Flow Algorithm (PFA) development.

Since GEM is already included in the SiD detector geometry, thanks to Norman Graf's efforts at SLAC, we will start with verifying the implementation of this geometry and conduct performance studies of GEM DHCAL in the SiD context. We will investigate the responses and energy resolutions of single particles to compare the detector's performance to the previous studies and will compare GEM with other detector technologies, such as RPC and scintillator based HCAL.

In addition, given the fact that we will be taking series of test beam runs, we need to prepare simulation packages for beam tests. Since we are part of CALICE, and will be an integral part of the CALICE test beam set up, we can utilize the MC framework that allows an easy integration of our detector geometry for the test beam, especially the run with the full scale $1m^3$ prototype. This will allow our students to exercise their analysis techniques in time for the full scale prototype run.

Since the largest contribution in worsening jet energy resolution in PFA comes from the confusion term that stems from unmatched or mismatched energy clusters, the fine granularity of the calorimeter cells will be of particular importance. However, the studies that have been conducted so far have yet to clearly demonstrate the dependence of PFA resolution on the lateral size of the cells and/or the granularity of longitudinal layers. This probably has to do with the fact that there is no unique PFA that the R&D groups can use as a common tool. This, however, should not stop the groups studying these dependencies with one given algorithm. In addition, the recent completion of a PFA template should certainly be of great help.

Since GEM can essentially provide track position information, it is natural for us to perform the cell dependence study and to provide optimal cell sizes for a PFA detector and other parameters such as absorber thickness, sensitive gap size, on-board readout electronics sizes, and mechanical support structures. These studies will be done, in particular, for GEM DHCAL.

The preparation and verification of simulation packages and studies in optimal detector parameters will allow us to naturally move into the development of PFA in the following years. We will start with developing an H-matrix based electron and photon identification algorithm, taking advantage of experience in ATLAS. This will be tested at the test beam and will be made available to the community for broader use. We will then move into cluster matching algorithm for hadrons, utilizing GEM's fine granularity.

To expedite the use of the beam test data, we will work closely with the SiD software development team and the CALICE software development team to incorporate GEM software into already existing data analysis software. The development of GEM test beam analysis software should begin as soon as possible so that it is prepared in time for the anticipated beam tests of five layers in late 2010 and early 2011.

To summarize, the major deliverables for FY2009 - 2011 in simulation and software efforts are as follows:

- Verification of GEM in the SiD geometry and comparisons of detector performance with previous studies
- Development and verification of PFA with GEM in SiD

- Development of analysis software, and analysis of beam test data

References

[1] D. Decamp et al., ALEPH Collaboration, Nucl. Inst. Meth. **A360**, 481, 1995.

[2] R. Bouclier, e*t al.*, "The Gas Electron Multiplier (GEM)," IEEE Trans. Nucl. Sci. **NS-44**, 646, 1997.

[3] F. Sauli "GEM: A new concept for electron amplification in gas detectors," Nucl. Inst. Meth., **A386**, 531, 1997.

[4] H. Videau, Presentation given at the Linear Collider retreat, Santa Cruz, CA, June 2002.

[5] V. Kaushik, "Performance of Novel Digital Hadron Calorimeter Using Gas Electron Multiplier (GEM) and the Energy Flow Algorithm Development," MS Thesis, University of Texas at Arlington, UTA-HEP/LC-004, Unpublished 2004.

[6] J. Yu, "GEM DHCal Development," Proceedings of Linear Collider Workshop 2007, DESY, Hamberg, Germany, June 2007.

[7] D. Underwood, "RPC R&D for DHCAL at ANL," In the proceedings of International Conference on Linear Colliders, LCWS2004, April 2004.

[8] V. Ammosov *et al.*, "RPC as a Detector for High Granularity Digital Hadron Calorimetry," Serpukhov, IHEP, DESY-04-057, March 2004.

[9] RD51 Collaboration, M. Titov & L. Ropelewski spokespersons, https://espace.cern.ch/test-RD51/default.aspx

[10] Meson Test Beam Facility, Fermi National Accelerator Laboratory, http://www-ppd.fnal.gov/MTBF-w/

[11] D. Freytag, et al., "KPiX, an Array of Self Triggered Charge Sensitive Cells Generating Digital Time and Amplitude Information," N64 – 8, IEEE – NSS 2008, to be published in NSS08 proceedings

[12] D. Strom, R. Frey, M. Breidenbach, D. Freytag, N. Graf, G. Haller, O. Milgrome, V. Radeka, "Design and development of a dense, fine grained silicon tungsten calorimeter with integrated electronics," to appear in Proceedings of the XI International Conference on Calorimeters in High Energy Physics, Perugia, Italy, March 2004.

[13] R. Frey, D. Strom, M. Breidenbach, D. Freytag, N. Graf, G. Haller, O. Milgrome, V. Radeka, "Silicon/tungsten ECal for SiD - Status and Progress," to appear in Proceedings of the International Conference on Linear Colliders, (LCWS 2004), Paris, France, April 2004.

[14] SiD, Silicon Detector Concept group for International Linear Collider, http://silicondetector.org/display/SiD/home

[15] Shalem, C., *et al.*, "Advances in Thick GEM-like gaseous electron multipliers - Part I: atmospheric pressure operation," Nuclear Instruments & Methods in Physics Research Section a-Accelerators Spectrometers Detectors and Associated Equipment, **558**(2), 475-489, 2006.

[16] Shalem, C.K., *et al.*, "Advances in thick GEM-like gaseous electron multipliers Part II: Low-pressure operation," Nuclear Instruments & Methods in Physics Research Section a-Accelerators Spectrometers Detectors and Associated Equipment, **558**(2), 468-474, 2006.

[17] Di Mauro, A., *et al.*, "A New GEM-like Imaging Detector with Electrodes Coated with Resistive Layers," in *IEEE Nuclear Science Symposium*. 2006. San Diego, CA.

[18] F. Sefkow, Spokesperson, CALICE, The Calorimeter for the Linear Colllider with Electrons Collaboration, http://polywww.in2p3.fr/flc/calice.html

Appendix

MICROMEGAS
a compact approach

A very interesting alternative for the DHCAL active medium is the MICRO MEsh GAseous Structure (MICROMEGAS) [1], a detector based on micro-pattern technology, today widely used by many experiments: COMPASS, CAST, NA48, n-TOF, T2K and the ILC TPC project. Our prototypes consist of a commercially available 20 μm thin mesh which separates the drift gap (3 mm) from the amplification gap (128 μm). The mesh is supported by insulating pillars placed according to a square pattern every 2.5 mm which provides good gas gain uniformity over the whole area. This simple structure allows full efficiency for MIPs. The rate obtained with MICROMEGAS chamber is not constrained, as it is the case of Glass RPCs. Moreover, the tiny size of the electron avalanches results in fast signals without physical crosstalk and leads to low hit multiplicity. The chosen bulk technology based on industrial PCB processes, offers a robust detector with working voltages lower than 500 V. MICROMEGAS, with anode pads as small as 1 cm^2, is therefore a very appealing option for a DHCAL optimized for a Particle Flow Algorithm.

Description of Prototypes

Three different kinds of prototypes with 1 cm^2 pad size were developed and built at LAPP: one type with analog readout for characterization and two types with embedded digital ASICs.

The analog readout is performed with boards from the CEA-IRFU laboratory, each equipped with 6 GASSIPLEX chips (96 channels in total), connected to VME ADCs which provide high resolution charge determination (12 bits, 0.4 fC per ADC Count). The data acquisition is performed by the CENTAURE program from SUBATECH [2]. Three chambers with 6×96 pads and one with 12×32 pads (see Fig. 1) were built with this analog readout.

Two mixed-signal ASICs are foreseen for the digital readout, the HARDROC [3] and the DIRAC [4]. The former was chosen as a baseline for the 1 m^3 European DHCAL project in order to get rapidly the digital readout of either MICROMEGAS or Glass RPC. The latter

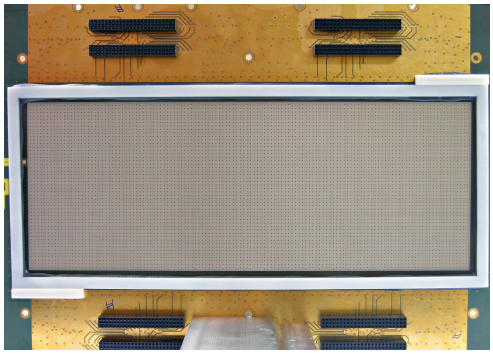

Figure 1: MICROMEGAS 12×32 cm^2 prototype with 1 cm^2 pads designed for analog readout.

is a long-term R&D which aims to obtain a low cost ASIC with an easy signal routing implementation on the detector PCB, easy calibration and digital readout down to MICROMEGAS MIP charges.

All MICROMEGAS bulks are realized by lamination of photosensitive foils and a mesh laid on a PCB with different signal routing depending on the readout. By photolithography, the photosensitive material is etched in some places producing the 128 μm high pillars. The drift gap is realized with a 3 mm thick frame which also provides the gas inlets (see Fig. 1 and 8). A thin copper foil, glued on the calorimeter absorber medium (2 mm thick plate out of a 2 cm thick absorber), defines the drift cathode. The top of the chamber, therefore, does not contribute to the active medium thickness.

The 1 m^2 prototype is an assembly on a single mask of six bulks with 24 ASICs each. The chamber is closed by two plates of 2 mm thick stainless steel (see Fig. 2). This prototype should not exceed a total thickness of 6 mm (without absorber). Its construction is on-going and it should be available for beam tests, with the former smaller prototypes, for late summer 2009. The 1 m^2 design is foreseen for large quantity production in order to build a 1 m^3 DHCAL prototype.

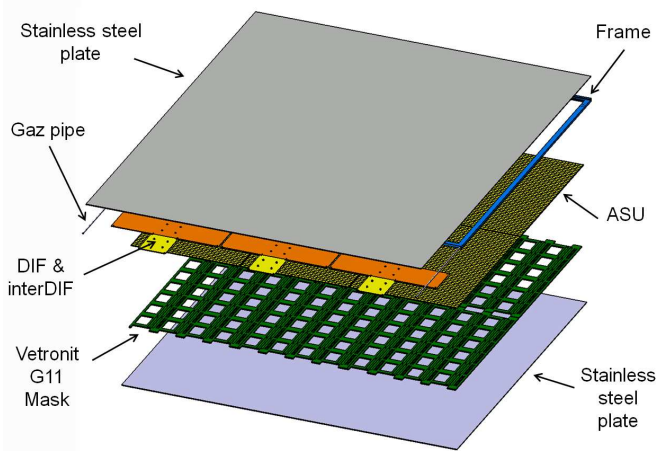

Figure 2: Design of the 1 m^2 MICROMEGAS prototype.

Analog Readout Prototypes

Using an ^{55}Fe X-ray source, the gain was measured with the analog readout up to 10^4 and an energy resolution down to 8.5% corresponding to a FWHM of 19.6 % was obtained (see Fig. 3 and 4). The gain and the resolution were measured as a function of the drift field, amplification field, gas flow and pressure variables. The expected exponential behavior of the gain versus the amplification field was verified (see Fig. 4) and an absolute pressure dependence of -2 fC/mbar was determined.

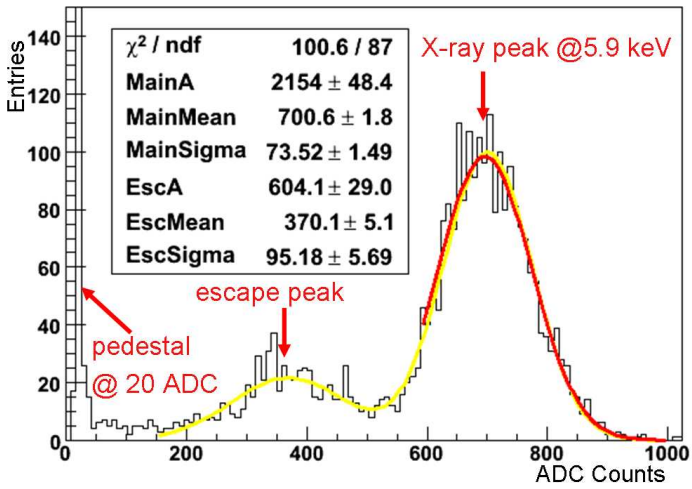

Figure 3: ^{55}Fe X-ray spectrum in 3 mm Ar/iC_4H_{10} 95/5 with E_{mesh} = 35 kV/cm and E_{drift} = 167 /cm. A gain of about 7600 is deduced from the 5.9 keV photopeak position (680 ADC Counts above perdestal, 277 fC).

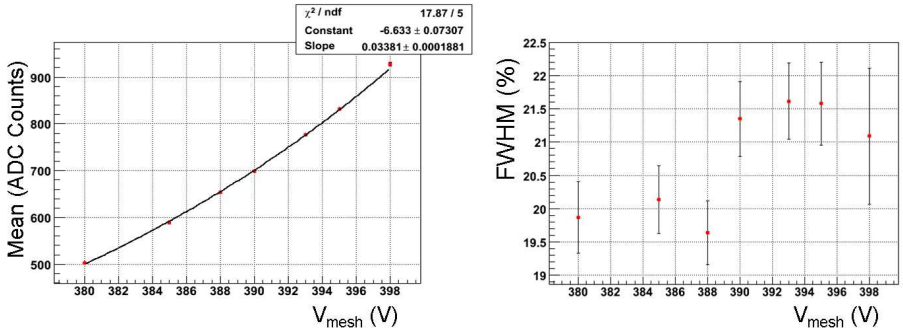

Figure 4: MICROMEGAS response and energy resolution at 5.9 keV as a function of mesh high voltage with E_{drift} = 167 V/cm.

In the summer 2008, four prototypes with analog readout were assembled in a stack and tested at the H2 line of the SPS-CERN. A total acquisition time of 5 days allowed the collection of about 200k muon and 200k pion events without absorber plus 250k pion events with an upstream 30 cm iron block and 1.8 cm iron absorbers between each prototype.

In the preliminary analysis of the 200k muons at 200 GeV, platinum events were selected by requiring one and only one hit (ADC Counts > 27) in each chamber. The Landau

distribution obtained on each pad has a Most Probable Value (MPV) around 45 fC. The four chambers mapping was performed in terms of pedestal mean and sigma, Landau distribution MPV and sigma. The pedestal gaussian fits showed very good noise conditions with an average standard deviation of 0.6 fC. The response is uniform within each prototype with a MPV relative variation of about 11 % RMS for the four prototypes (see Fig. 5). Electronics channel disparity and drift space non-uniformity are still to be quantified.

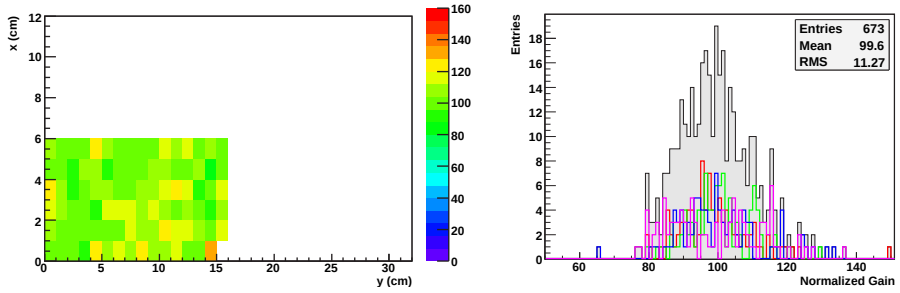

Figure 5: Example of a prototype mapping with analog readout: MPV in ADC Counts for golden events selected in a 200 GeV muons sample. MPV dispersion normalized to 100 % for the four prototypes with analog readout.

With the same muon sample, golden events were selected by requiring one and only one safe hit (ADC Counts > 51) in three of the four prototypes. A straight line was fitted to the three hits and the efficiency of the last prototype was calculated by looking for at least one hit (ADC Counts > 27, charge > 2.8 fC) in a 3×3 pad square centered around the extrapolated line (see Table 1). With the golden events the multiplicity was measured by counting the number of hits in the same square, a multiplicity of about 1.07 was found.

Prototype	Efficiency (charge > 2.8 fC)
0 (96 pads)	$97.05 \pm 0.07\%$
1 (96 pads)	$98.54 \pm 0.05\%$
2 (96 pads)	$92.99 \pm 0.10\%$
3 (384 pads)	$96.17 \pm 0.07\%$

Table 1: Efficiency of the MICROMEGAS prototypes with analog readout.

Digital Readout Prototypes

The DIRAC chip [4] was embedded on an 8×8 cm^2 PCB with additional spark protections (see Fig. 6). For the first time a functional prototype with a bulk laid on a PCB with embedded electronics reaching a total thickness of 12 mm including 2 mm of absorber could be exposed to 200 GeV pions at the H2 beam line in summer 2008. Fig. 7 shows the beam profile as measured with a threshold of 19 fC. Further tests with a stack of prototypes are foreseen to measure threshold dependence, efficiency and multiplicity.

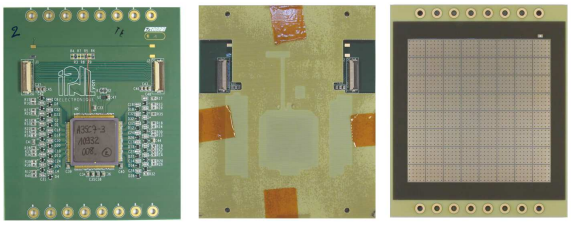

Figure 6: MICROMEGAS prototype with DIRAC digital readout. From left to right: ASIC side, ASIC side with mask for bulk laying and pad side with bulk.

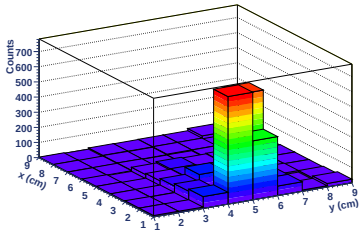

Figure 7: Chamber mapping of the MICROMEGAS prototype with DIRAC digital readout: digital counts in a 200 GeV pion sample.

Several new 8×32 pads prototypes have been realized with four HARDROC chips embedded on one PCB (see Fig. 8). The electronics is tested with the Detector InterFace board (DIF) which has been designed at LAPP in the frame of the DHCAL CALICE data acquisition system [5]. These prototypes have been exposed to 7 GeV pions at the T9 line of the PS-CERN in November 2008.

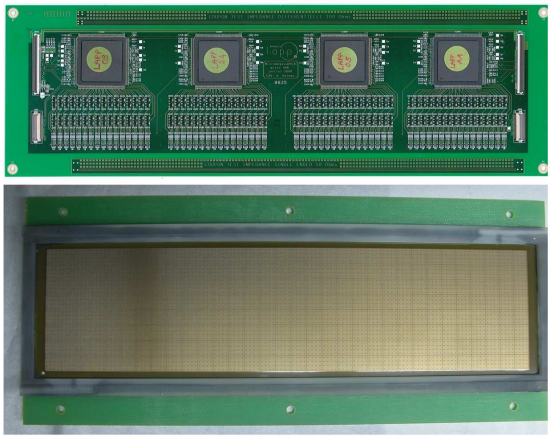

Figure 8: MICROMEGAS prototype with 4 HARDROCs digital readout. From top to bottom: ASIC side and pad side with bulk and drift frame.

References

[1] Y, Giomataris, Ph. Rebourgeard, J.P Robert and G. Charpak, "MICROMEGAS: A High granularity position sensitive gaseous detector for high particle flux environments", NIM A376, 1996, pp 29-35

[2] D. Roy, "CENTAURE Acquisition Program", http://www-subatech.in2p3.fr/ electro/infoaq/CENTAURE/main_centaure.html

[3] S. Callier, F. Dulucq, Ch. de La Taille, G. Martin-Chassard, N. Seguin-Moreau, R. Gaglione, I. Laktineh, H. Mathez, V. Boudry, J-C. Brient, C. Jauffret, "HARDROC1, readout chip of the Digital HAdronic CALorimeter of ILC", IEEE-NSS Conference Record, vol 3, 2007, pp 1851-1856

[4] R. Gaglione, "DIRAC: Digital Readout ASIC for hAdronic Calorimeter", IEEE-NSS/MIC 2008

[5] B. Hommels, "Data Acquisition Systems for Future Calorimetry at the International Linear Collider", IEEE-NSS/MIC 2008

High Resolution Jet Calorimetry Option

Principles of Operation: Energy Resolution

Principal limitations of the hadron energy resolution come from two sources:

sampling nature of the conventional hadron calorimeters. In addition to the inevitable fluctuations of the energy sharing between passive and active parts of the calorimeter (sampling fluctuations) it induces additional fluctuations due to the fact that the effective sampling fractions depend on the particle type and its energy

a significant and fluctuating fraction of the incoming hadron energy is converted into non-observable forms of energy (primarily nuclear binding energy)

These effects lead to a significant non-linearity of the response of the detector and to a difference of the response to neutral and charged pions (often referred to as e/ ratio). They are responsible for the dominant contribution to jet energy resolution, as the result of the fluctuations in the jet fragmentation.

Good jet energy resolution requires a calorimeter where both of the above-mentioned factors are eliminated or largely reduced. This can be accomplished with a homogenous, totally active calorimeter with dual readout: scintillation and Cherenkov. Totally active calorimeter eliminates all contributions related to the sampling nature of the device whereas an anti-correlation between the scintillation and Cherenkov light (see Fig.1) can be used to reduce the fluctuations of the nuclear binding energy loss.

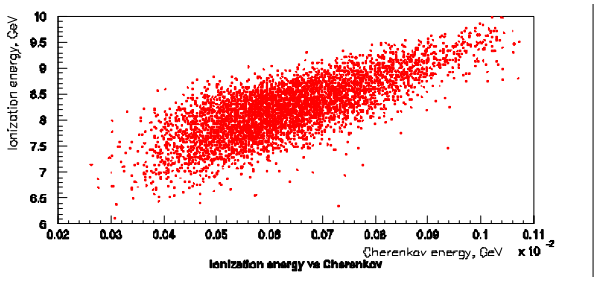

Fig. 1 Correlation of the total ionization energy loss in a hadron showers with the amount of the Cherenkov light.

Anti-correlation of Cherenkov and scintillation light can be expressed as a dimensionless fashion as a fraction of the total particle energy detected via scintillation as a function of Cherenkov-to-scintillation light, as shown in Fig. 2 (a). Application of such an event-by-event correction to a sample of hadron induced showers improves the energy resolution and makes the average hadron response equal to the beam energy (hence equal to the response to electrons on neutral pions of the same energy), as shown in Fig 2(b) .

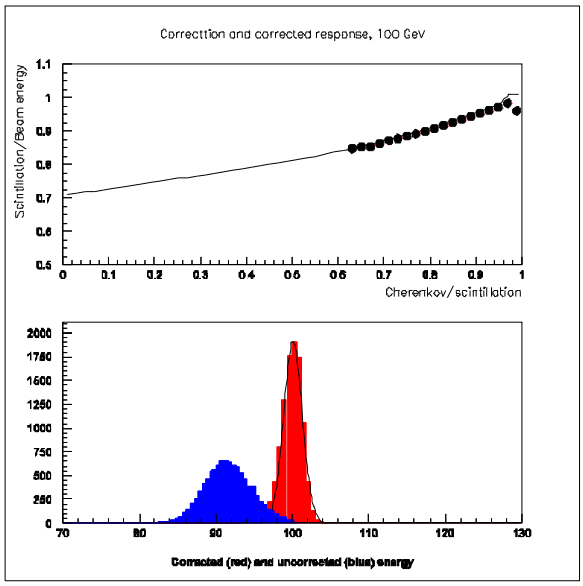

Fig. 2 (a) -top: The correlation between the average fraction of the beam energy detected via scintillation and the ratio of responses measured with the Cherenkov and the scintillation light. (b)-bottom: A response of the total absorption calorimeter to 100 GeV pion beam (blue) and the same response corrected on the event-by-event basis using the correlation from Fig. 2 (a). Both results are based on GEANT4 simulation.

The correlation function, Fig. 2(a), is very weakly dependent on the parent particle type and/or energy and even use of the same function at different energies does not spoil the energy resolution. This is of particular importance in the case of hadronic jets, where the contributions of different particles are in general summed up. Fig 3. illustrates the resulting energy resolution of the total absorption calorimeter for single hadrons and for hadronic jets (in the latter case a crude algorithm of summing up all scintillation and all Cherenkov light and applying one overall correction was used.) Figs 3 and 4 show the resulting corrected response to single hadrons and hadronic jets of different energies. The response function is to a good approximation gaussian with no visible tails of the resolution.

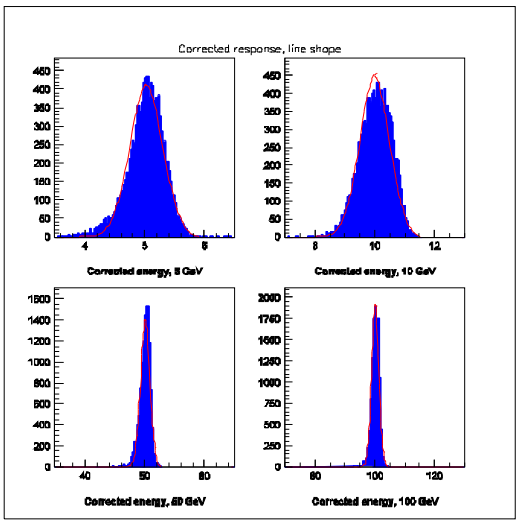

Fig. 3. Corrected response of a total absorption dual readout calorimeter to single hadrons of different energies.

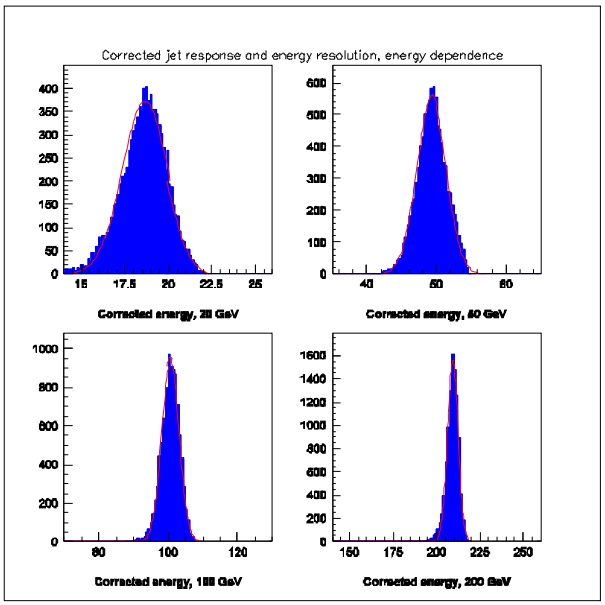

Fig. 4. Corrected response of a total absorption dual readout calorimeter to hadronic jets of different energies. Jets are generated using Pythia.

The resulting corrected response and energy resolution for single hadrons and jets energy is shown in Figs. 5 and 6. For single hadrons the energy resolution is of the order of $0.15/\sqrt{E}$ whereas for hadronic jets above 100 GeV the energy resolution is better than $0.25/\sqrt{E}$. There is no indication of a deviation from the $1/\sqrt{E}$ behavior of the resolution in the investigated energy range. In case of hadronic jets there some residual non-linearity of the overall response and a degradation of the energy resolution at low energies are probably a result of a very crude reconstruction and correction algorithm.

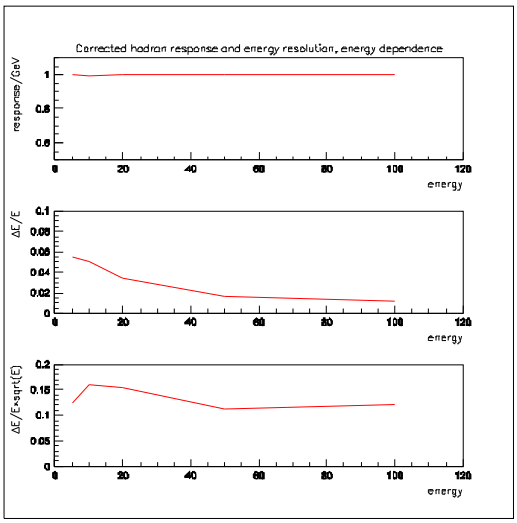

Fig. 5. Response linearity, energy resolution and scaled energy resolution for single hadrons.

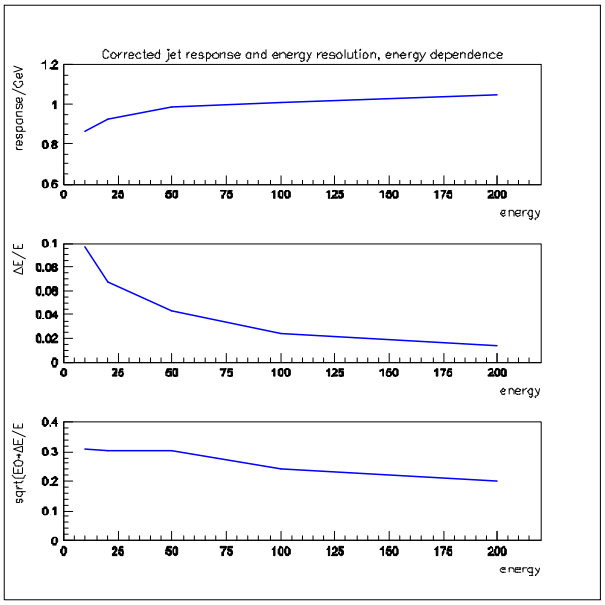

Fig. 6. Response linearity, energy resolution and scaled energy resolution for hadronic jets.

It should be pointed out that the energy resolution described above is attained without any relation to the detector granularity, only a total amount of scintillation and Cherenkov was used. Such a technique does not, therefore, require any particular segmentation of the calorimeter on one hand, but it does not preclude it other, provided that the adequate cross-calibration of the detector elements is accomplished. The calorimeter segmentation will be determined by a combination of 'other' physics-driven requirements and practical aspects like calibration and engineering aspects. One should expect that additional information available from the spatial distribution of the observed signals may be used to improve further the energy resolution for the hadronic jets.

Particle Identification Capabilities

One of the pre-requisites necessary to attain good energy resolution is the detection of

Cherenkov light produced by particles traversing the calorimeter. At the same time this may provide unique capabilities for the particle identification, at least for some of the jet particles. Recent initiatives on the development of picosecond timing [Chicago/Argonne/Saclay offer an interesting possibilities for very precise time-of-flight measurement and the identification of lower energy particles inside the hadronic jet; fast Cherenkov signal being an enabling factor. Full exploitation of the advantages offered by very fast timing require a development of fast, large area, pixelized photodetectors, though, and such an avenue is pursued by Argonne. This, in turns opens up yet another possibility of particles identification via the ring imaging of the Cherenkov light.

Particle identification capabilities require charged particle detection and measurement before the first hadronic interaction and the start of the resulting shower. They may also be affected by the particles overlap in the detector elements, hence the full assessment of the particle identification efficiency requires a careful optimization of the detector design.

Spatial/Topological Information

Calorimeters are used to provide more information than the energy of particles and/or jets. Measurement of an angle of the detected high energy photon or separation of close electromagnetic showers are the examples such additional functions of the calorimeters and they often are used to constrain the design and the granularity of electromagnetic calorimeters. From the point of vie of the hadron/jet energy resolution this is highly undesirable: separate and different section of the caalorimeter tend to produce a significant contribution to the energy resolution.

To maintain excellent hadronic energy resolution it is necessary to find a way to provide the spatial/topological information within a concept of a total absorption calorimeter. One of the possibilities may involve very fine segmentation of the front section calorimeter. Another possibility may involve several layers of silicon pixel detectors embedded at several depth in the front section of the calorimeter, as pioneered by the LCCAL project. Yet another possibility may involve use, perhaps in the early depth segment of the calorimeter, of some of the novel optical materials, composite of crystal fibers, which have been recently developed.

Enabling Technological Developments

The concept of the dual readout calorimetry has been around for more than two decades [Paul Mockett]. The required separation of the Cherenkov and scintillation light using the timing information has been demonstrated experimentally in 1984 [IEEE Transaction]. The DREAM Collaboration has recently demonstrated such a separation by using the wavelength separation [Wigmans]. Whereas the principles underlying the possible high resolution hadron calorimetry were known and understood for a very long time, the construction of a practical hadron calorimeter, especially with the hermeticity required in the colliding beam environment, was made possible by several technological breakthroughs:

development of affordable, high density, scintillating crystals. Good energy resolution requires an adequate depth of the calorimeter, in excess of 6-7 interaction length. The primary example here is the development of lead tungstate crystals for the CMS experiment, where the entire development and large scale production cycle was driven by the requirement of a single HEP experiment.

advent of compact, inexpensive silicon-based photodetectors (APD's and SiPM's) capable of operating in a string magnetic field.

The specific requirements of the hadron calorimeter case are quite different from the other applications, hence there are no off-the-shelf solutions to the detector problems but the recent developments allow for an optimistic view that some additional R&D efforts may lead to a successful construction of a hadron calorimeter with unique capabilities of very high energy

resolution, good particle identification and very good spatial localization of electromagnetic showers.

Conceptual Design of High Resolution Calorimeter (HRC)

A high resolution calorimeter is designed to fit into the space occupied by the ECAL and HCAL of the baseline design. It is constructed of optical "crystals" equipped with two sets of compact silicon photodetectors at the back. One set, equipped with the low pass optical filter and short integration gate electronics, is used to detect and measure the Cherenkov light. The other set, equipped with high pass filter and long integration gate electronics is used to detect and measure the scintillation component.

The barrel section is composed of four layers of crystals with approximate dimensions of 5 5 $5cm^3$, followed by ten layers of larger crystals with approximate dimensions of 10 10 $10cm^3$. First four layers of crystals have silicon pixel detectors attached to the front face.

The endcaps are constructed in a very similar fashion, with four layers of 5 5 $5cm^3$crystals followed by sixteen layers of 10 10 $10cm^3$ crystals. Assuming crystals of density similar to lead tungstate, with the absorption length of the order of 20 cm this leads to a calorimeter with the thickness of 6 at 90^o and 9 in a forward direction.

Calorimeter is constructed by assembling the crystals into non-projective modules with the help of structural epoxy and the readout cables transported to the back planes in non-projective slots. Compact nature of the photodetectors and minimal energy consumption of the photodetectors and the associated readout electronics assures high average density of the calorimeter. The construction may result in mechanical units identical to the ones of the baseline design.

Principal Challenges of the HRC

Fundamental physics principles of the total absorption dual readout hadron calorimetry are relatively well understood. It is, naturally, highly desirable that this understanding is confirmed by a practical demonstration of the performance in the test beam, but for a construction of a practical detector there are several more milestones which need to be reached:

development of inexpensive optical materials for the dual readout. The principal requirements are

- short interaction length, of the order of 20 cm
- capabilities of distinguishing the Cherenkov and scintillation light (by timing, wavelength or combination of both)
- low cost for large scale production
- adequate physical/mechanical properties for construction of a large detector

availability of compact photodetectors capable of operation in a strong magnetic field and the corresponding low power dissipation front-end readout electronics. The most challenging aspects of the photodetectors include:

- cost
- adequate area (this is especially important for the Cherenkov component)
- adequate sensitivity for short wavelength light. It is important to remember that the photodetector assembly may include some waveshifting elements converting the Cherenkov light to a longer wavelength, provided that it preserves the Cherenkov-scintillation separation capabilities.

In addition to these challenges, which must be met by industrial vendors, the realistic design of the detector will require detailed simulation and optimization studies as well as a complete

engineering design. A realistic and robust scheme for the relative (channel-to-channel, scintillation-to-Cherenkov) as well as the absolute calibration must be developed as well.

R&D Program

In order to bring the HRC concept to the level necessary for considerations as a possible alternative calorimeter for the SiD detector it is necessary that sufficient progress is achieved along the following directions:

Task 1: demonstration of good response linearity and energy resolution for hadrons in the test beam. At the same time the capabilities of adequate measurement of the spatial characteristics, in particular two close shower separation, must be established. Although it would be desirable, it is not necessary that these studies must utilize the final crystals and/or photodetectors.

Task 2: optimization of the detector performance, including the algorithms for local dual readout corrections, jet finding and reconstruction, optimization of the detector granularity

Task 3: engineering design of the detector and its support structure. In particular the attention must be paid that the inevitable structural members do not degrade the final energy resolution.

Task 4: development of novel inexpensive optical materials

Task 5: development of compact photodetection scheme and associated readout electronics

Task 1

Demonstration of an excellent energy resolution in the test beam is a very challenging project and it will require detailed preparations and several intermediate steps. They will include:

establishing a single crystal evaluation setup to perform the complete characterization of scintillation and Cherenkov light emission and collection. The principal results of these studies will be the measurement of absolute and relative light yields from scintillation and Cherenkov as a function of the particle angle.

studies of light propagation and collection in crystals, methods of optimizing the collection efficiency and uniformity

development of adequate crystal-to-crystal calibration scheme

demonstration of the energy resolution of the segmented and calibrated calorimeter for electrons

demonstration of the precision of measurement of spatial characteristics of an electromagnetic shower and two shower separation

This phase of the program will serve as learning ground to identify and understand possible practical problems and issues associated with segmented crystals calorimetry. It will evolve into a design and construction of a full scale hadron calorimeter prototype. The size and shape of such a prototype must be carefully optimized to ensure the adequate containment of the hadronic showers in a fiscally affordable. The full scale prototype may be constructed using the newly developed inexpensive crystals, but it is far more likely that it will use some of the currently available crystals. The same comments apply to the photodetectors and the front-end electronics. A particular attention must be paid to the development of the calibration scheme enabling precise cross-calibration of crystals and scintillation-to-Cherenkov response.

Task 2

Detailed Monte Carlo simulation studies will be continued to further the understanding of the dependence of the calorimeter performance on the detector design details. Possible use of local Cherenkov-to-scintillation ratio may improve the energy resolution. Jet identification and reconstruction algorithm will be studied to optimize the detector design, and in particular its spatial granularity. Possible use of particle flow algorithm to further improve the energy resolution and its relation to the detector granularity will be investigated. Particle identification capabilities via

time-of-flight and by ring imaging will be studied to optimize the detector design.

Task 3

Conceptual design of the calorimeter will be carried out to identify all the factors affecting the detector performance. In particular they will include structural members (dead materials), cracks for the cables and services and cables themselves. These design details will be implemented into the detailed detector simulation program to evaluate the impact on the detector performance. Practical constraints imposed by the solenoidal magnet will likely lead to some of the energy leaking out from the calorimeter. Use of the muon system as a backing calorimeter will be evaluated and it may impact details of the design of the muon system.

Task 4

Practicality of the optical calorimeter depends in a critical manner on the cost of the crystals. None of the crystals produced at present in large quantities present an affordable possibilty. Performance requirements, in particular the scintillation light yield, are substantially different from the specification of of the current generation of crystals, making it quite plausible that there are some potential crystals which can be produced at affordable cost.Search for crystals optimized for a dual readout has already begun, and some initial results have been presented at IEEE conference. The leand tungstate/lead molybdenate crystals have been produced in Bogoroditsk and offer attractive advanteges for the separation of Cherenkov and scintillation light [Korzhik]. Lead fluorite is a very good Cherenkov radiator several attempts to dope it with a scinitillating agent have been tried. The process is in its infancy, though and it will require closer contactes with the crystal making industry.

While single monocrystals offer the most promising material in terms of thei optical properties it may well be that recent advances in production of heavy scintillating glasses offer an adequate solution. We expect to survey the current status of the R&D and perhaps initiate some new efforts.

It should be also noted that there is a significant progress in the area of design and production of novel optical media: sintered ceramics and single-crystal fibers are good examples. We expect to develop closer contacts with this efforts, evaluate the existing materials and possibly stimulate some new studies.

The development of inexpensive optical materials is the key to high resolution calorimetry therefore we expect to deveop a comprehensive program of studies with the relevant industrial parters.

Task 5

Silicon-based photodetectors and in particlar Geiger mode Avalanche Photodiodes offer a very attractive possibility for a compact readout of light in a hermetic calorimeter. These detectors are relatively new and we are actively engaged in the efforts to eveluate and characterize them with the goal of improving their performance and establishing some fundamental principles of their use. Their principal limitation, especially for the purpose of the detection of Cherenkov light is their small size. Larger size detectors are becoming slowly available and we will keep evaluating them.

Development of the front-end electronics suitable for the use in hermetic calorimeter is one of the significant challenges in using these photodetectors. We expect to contribute here by developing a dedicated ASIC chip.

A separate effort to develop large area inexpensive fast photodetectors at Argonne is of great interest here and we envisage an active participation in it. Such detectors are likely to be enabling factors for the possible particle identification capabilities of the calorimeter.

Muon System R&D Overview

Editors: H.R. Band, H. E. Fisk

0.1 Introduction

The primary aim of the muon system R&D is to validate both possible detector choices and to develop cost-effective read-out designs. The RPC R&D effort is focused on adapting the KPIX ADC to digitize RPC signals[1]. Other studies will measure the aging characteristics of IHEP RPCs and search for gas mixtures or cathode materials with better aging properties[2]. The groups involved with the scintillating strip option will evaluate SiPM devices from different manufacturers and develop mounting, temperature control, and calibration designs[3]. Both the KPIX and SiPM effortswill be applicable to the HCAL RPC and scintillator detector options. Further details of the Muon System R&D plans can be found in the individual R&D proposals [1, 2, 3].

0.1.1 RPC R&D

Close integration of the RPCs and front-end and digitization electronics is necessary to minimize cabling and costs. It is imperative that low cost, reliable readout schemes for the RPCs be developed since the expected channel counts for the SiD detector are so high (nearly one million for the muon system). One possible low cost solution is to adapt the KPiX chip, presently being developed for use in the SiD electromagnetic calorimeter, for use with RPCs. An RPC/KPiX interface board was designed and built to provide ribbon cable connections to a 64 channel KPiX chip (v7). The RPC strip signal is AC coupled to the KPiX input through a 5 nF blocking capacitor and a 2 stage diode protection network. Each strip is also tied to signal ground via a resistor external to the interface board. Signals induced on the RPC strip have a very fast rise time (< 10 nsec) and a fall time determined by the RC time constant of the strip capacitance (300 pF) and R, if R is less than the effective resistance of the Bakelite cathode/anodes. Previous experiments such a BaBar and BELLE used small values of R (50-100 ohm) to make short fast signals (< 100 nsec) suitable for fast timing applications. However, the present KPiX chip samples the signal after > 400 nsec, requiring longer signal widths. Understanding the response of the KPiX device to different values of R and the blocking capacitor is of fundamental importance in adapting the KPiX chip to gas detectors. It is likely that optimizing the performance of the RPC/KPiX will require modification of the KPiX shaping and integration times. Future KPiX versions are planned to have more timing options.

A BaBar test RPC was connected to the interface board by a .5 m cable.The chamber was operated at 9300 V in avalanche mode using a premix gas with composition of 75.5% Freon 134a, 19.4% argon, 4.5% isobutane, and 0.%5 SF6. The chamber efficiency had been previously measured to be >90% using BaBar electronics. The sum of the 13 RPC strips on the HV ground side (positive signal) is shown in Figure 1.The sharp spike near zero is due to cosmic ray tracks that either missed the test RPC or to RPC inefficiency. The width of this spike was 29 fC about three times larger than expected based on the noise performance of KPiX, indicating that there may be electronic pickup. The data peak is centered at 3.8 pC with a width of 2.2 pC. The data signal is consistent with, but larger than, avalanche RPC signals measured by other groups (-1 pC) which used avalanche gases with no argon component. The BaBar avalanche gas contains 20% argon and should have a higher gas gain. The size and distribution of charge in the RPC pickup strips was studied. The charge of the strip with the maximum charge for each trigger has less than half of the total charge in the event. A strip multiplicity was calculated as a function of the discrimination threshold. With a threshold of 300 fC, about 92% of the cosmic triggers have 1 or more strips hit and the average strip multiplicity is 3.1, more than twice that observed in BaBar. High strip multiplicities are undesirable since they degrade the position resolution and the ability to separate two tracks near each other. Further characterization and optimization of the interface board between the RPC and KPiX chip is needed to understand the larger than expected noise and strip multiplicities that were observed.

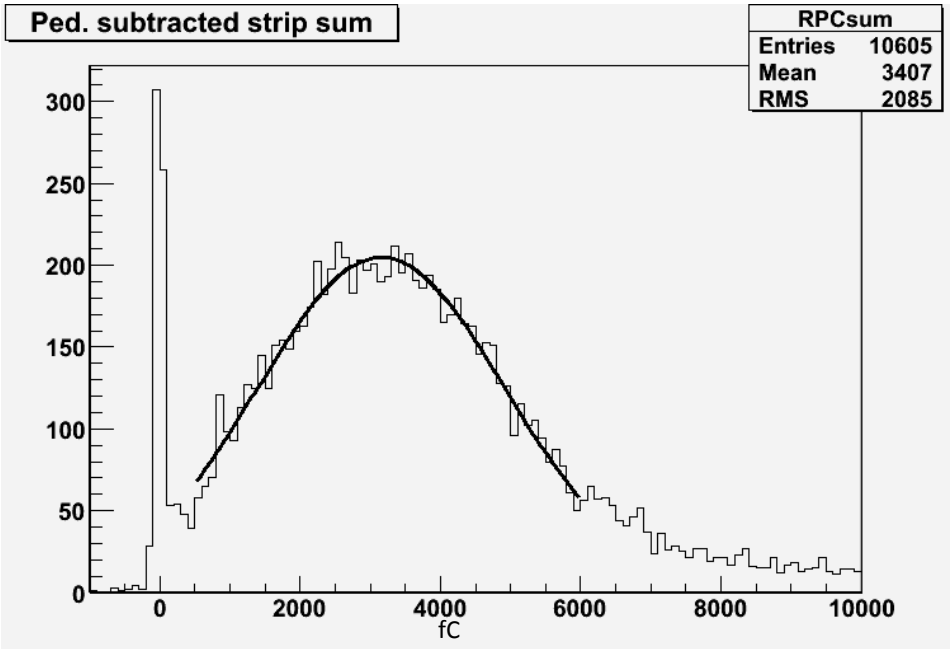

Figure 1: Sum of the pulse heights in 13 RPC strips readout by KPIX. The peak position of ∼3 pC and efficiency of >90% are consistent with previous studies of avalanche mode RPCs.

Many large RPC systems have been built within the last 10 years and understanding their performance will provide strong guidance for an SiD design. Several types of RPC construction have been used in high energy experiments. RPCs with Bakelite cathodes and anodes were pioneered by Santonico et al[4] and used in BaBar, CMS, ATLAS and a variety

of cosmic ray and neutrino experiments. The early failure of many BaBar RPCs stimulated detailed study of RPC aging and lead to many significant improvements in construction practices and operation. The linseed oil used to coat the inner HV surfaces has often been a source of concern. The IHEP group and Chinese industry have developed a Bakelite /melamine cathode for use in the BES III and Daya Bay detectors that does not require linseed oil treatment to achieve acceptable noise rates. These RPCs are operated in streamer mode in their present applications. SiD proposes to operate its RPCs in avalanche mode. Tests of IHEP RPCs in avalanche mode will be used to determine the efficiency, current and noise rate as a function of HV and gas composition and to establish their suitability for use in SiD. Longer term tests will also be needed to investigate the aging properties of the IHEP RPCs. All of the working RPC systems utilize Freon as a major gas constituent. Several researchers have found significant levels of HF acid in the exhaust gas indicating the breakdown of the Freon or SF6 during the gas avalanche or streamer. BELLE found that in the presence of water vapor that the HF would etch the glass surface, generating sizable noise currents and lowering efficiency. The effect on Bakelite RPCs is less understood, but there is clear evidence that pollutants generated by high rate in the gas can affect both the noise rate and dark current. Groups from the University of Wisconsin and Roma have measured the fluorine levels of the exhaust gas in both streamer and avalanche RPCs at BaBar and correlated these levels with the chamber current, noise rate, and efficiencyl[5]. Further studies of BaBar RPCs may shed light on the long term effects of HF on the Bakelite surfaces. Longer term goals are to develop RPC gas mixes which either eliminate or substantially reduce the Freon component. A group at Princeton University is also studying the effect of HF on Bakelite surfaces and will extend these studies to the new RPCs developed by IHEP.

0.1.2 Extruded Scintillator and Photodetector R&D

In 2000 it was noted that the ILC muon system requirements could be met with a MINOS type scintillator detector design[6] that would give both muon identification and be used to measure the tails of late developing or highly energetic hadron showers. This seems rather appropriate since the depth of the ILC calorimeters is limited because they are inside the superconducting (SC) solenoid. As an example, neutral hadrons that represent ∼11% of the final-state energy in Higgs and W-W production, primarily neutrons and K_L's, prove to be difficult to identify and measure[7]. The physics case for tail catching of showers is based on improvement of jet energy resolution when the energy downstream of the SC solenoid is included in the definition of jet energy[8],[9].

The MINOS experiment has already proved that a strip-scintillator detector works well for identifying muons and for measuring hadronic energy in neutrino interactions. The ILC R&D muon scintillator detector effort is directed at understanding how to deploy such detectors in the ILC environment and to understand possible improvements that could lead to reduced complexity and /or cost, with photon detection based on SiPMS.

A possible layout of quadrant strips for the forward muon scintillator system could have alternate planes of detectors rotated by 90^o relative to each other. Each quadrant would contain ∼ 158 strips 4.1 cm wide and of variable length. The mean strip length is 5.05 m. Muon scintillator-strip detectors located in the Fe barrel octant gaps could be arranged in

planes where the u-v strips are oriented at $\pm$ 45^o to a plane's edges or, alternatively, parallel to the edges in x-y fashion.

Earlier strip-scintillator R&D[10] using 4.1cm wide by 1cm thick extruded MINOS style scintillator that was readout with multi-anode photomultiplier tubes (MAPMTs) demonstrated that $>$ 9 photo-electrons were achieved with 1.8m long strips in which the wavelength shifted scintillation light was carried to MAPMTs through a thermally fused clear optical fiber to the MAPMT a few meters away[11]. The measured light transmission was required to be $>$ 80% for each splice.

We have recently procured Silicon based photon detectors (SiPMS) for tests with our scintillator. Sixty multi-pixel photon counters (MPPCs) have been purchased from Hamamatsu: 20 each of 100, 400 and 1600 pixels in a 1 mm square array. In addition INFN Udine-based collaborators have obtained 100 IRST SiPMS that have approximately 688 pixels inside a 1.2mm dia. circular matrix for muon/tailcatcher R&D.

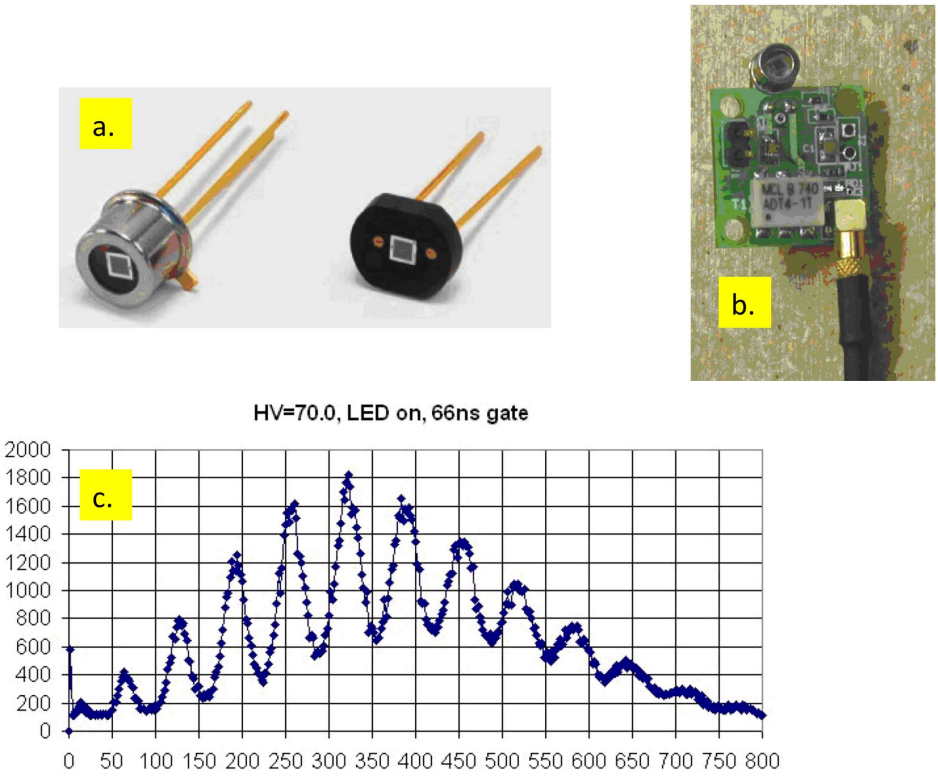

Figure 2: SIPM Hamamatsu MPPC and 2cm scale front-end electronics test setup. The output is generated with a pulsed LED providing the input light.

Recently strips with MPPCs and IRST devices have been assembled and tests with beam have begun. A real advantage of the SiPMS is the ability to see the summed output from the full assembly of pixels and observe in a pulse height spectrum that shows a number of photo-electron peaks. A modest calorimetric disadvantage is that the SiPMs put out spontaneous pulses with no defined input (noise). This disadvantage can be parlayed into an advantage in terms of calibration. With a good oscilloscope one observes bands of 1,

2 and sometimes 3 photo-electrons from which a reasonable calibration is possible. This calibration aspect needs study and engineering, which is part of our proposed R&D program. It should be mentioned that during our test beam studies we accumulated well over a million triggers using a 1.8m long strip and observed 100% efficiency when triggers were formed with independent trigger counters. Figure 2 shows an MPPC output spectrum from a test circuit and constant amplitude input LED pulses.

The SiD Muon Studies group consists of physicists from: Fermilab, Indiana U, INFN Udine, Livermore, NIU, U Notre Dame, Rochester, Wayne State and Wisconsin. These groups are testing RPCs, scintillator, SiPMS, prototype planes, frontend electronics and we are using beam test results to understand issues and costs associated with the application of RPCs and strip-scintillator technology to an LC muon system. The tests are an exploration of construction issues, device characteristics such as pulse shaping, readout, amplitude, gain and cross-talk, digitization, packaging, cables, signal collection from many strips and their transport from the detector to signal storage. A list of R&D items with the priorities and personnel is shown in Table 1.

0.1.3 Milestones

- RPC/KPIX proof of principle -2008-9
- Optimize interface board & protection circuitry design 2009-10
- Cosmic ray tests
- Beam tests – RPC/KPIX
- SiPM proof of principle -2008-9

Table 1: Muon/Tail Catcher R&D Summary

Rank	R&D Item	Institutions	Personnel	K$
1	Studies of KPIX/RPC readout with IHEP RPCs Continue tests of KPIX readout for RPCs in avalanche mode. Optimize interface board, test performance & reliability Begin aging tests of IHEP RPCs.	Wisconsin	H. Band & student	45 WIS
1	SiPMs from HPK and IRST - Bench Tests Current vs Bias Voltage to establish operating voltage, gain, noise rate vs. temp., threshold, etc. Test 150 devices from IRST (It.) & HPK (Jp.) LED pulser development.	Fermilab Indiana INFN Udine NIU Notre Dame Wayne State	Si Detector Facility: Para Van Kooten et al Pauletta et al. Hedin, Chakraborty, Dychkant, Zutshi. Wayne, Baumbaugh, McKenna Karchin, Gutierrez, et al.	30 F 21 IU 20 WSU
1	Strip & Fiber Mechanical R&D. Geometry of strip ends + SiPM FE miniature circuit. Prep. of ∼30 strips w/WLS fiber. QC checks. Light pulser tests.	Notre Dame Fermilab INFN Udine	McKenna, Wayne Rubinov, Fisk. Pauletta	23 UND 50 F
1	MTest studies of strips and instrumentation. Calibration from photo-electron peaks. Signal/noise vs. trans. & long. position. CAMAC/Minerva electronics.	INFN Udine Fermilab Notre Dame Wayne State	Pauletta et al Rubinov, Fisk Baumbaugh Gutierrez, students	20 F
2	FE electronics devel. AC vs. DC coupling; Temp. compensated gain; Strip signal transport, collection & digitization. Multiplexing scheme.	Fermilab Indiana Wayne State INFN Udine	Rubinov, Fitzpatrick Van Kooten Karchin Pauletta	30 F
2	Tail catcher R&D with CALICE; Gain issues, E Res. vs. # of pixels.	NIU	Chakaraborty, Zutshi	30 NIU
3	Fast timing studies	NIU	Hedin	
3	Simulations. Testbeam software. Analysis software.	Rochester INFN Udine All	Manly Pauletta, et al	
4	Co-extrusion of scintillator and WLS fiber	Fermilab Notre Dame	Fisk Ruchti, Wayne,	

References

[1] H. R. Band,"*RPC/KPiX Studies for Use in Linear Collider Detectors*,"
http://silicondetector.org/download/attachments/37323762/RPC_Wisc.pdf

[2] C. Lu *et al.* "*Aging Study for SiD Hcal and Muon System RPCs*,"
http://silicondetector.org/download/attachments/37323762/
RPC_Princeton_k.pdf

[3] P. Karchin *et al.*,"*Scintillator Based Muon System & Tail-CatcherR&D*",
http://silicondetector.org/download/attachments/37323762/
ILC_Muon_2009_proposal_v2.pdf

[4] R. Santonico, "*RPC understanding and future perspectives*". Nucl. Inst. and Meth. A**533**, 1-6(2004).

[5] H.R. Band et al, "*Study of HF production in BaBar Resistive Plate Chambers*". Nucl. Inst. and Meth. A**594**, 33-38(2008).

[6] Para, A. "*Solid Scintillator-based Muon Detector for Linear Collider Experiments*," Physics and Experiments with Future Linear e^+e^- Colliders, ed. A. Para and H. E. Fisk (2001)pg. 865-869, American Institute of Physics, Melville, New York (Vol. **578**)

[7] Frey, R."*Experimental Issues for the Workshop*," International Conference on Linear Colliders – LCWS 2004, p 29 Eds. H. Videau & J-C. Brient, Editions de l'Ecole Polytechnique, Julliet 2005, 91128 Palaiseau Cedex

[8] M. J. Charles,"*PFA Performance for SiD,*"
(to be published) proc. of the Linear Collider Work Shop,(2008),
Univ. of Illinois at Chicago,
http://arxiv.org/PS_cache/arxiv/pdf/0901/0901.4670v1.pdf

[9] Salcido, P., (CALICE Collab.) LCSW08 Calorimeter & Muons Session: TCMT and combined analysis, Nov. 17,2008 (unpublished)

[10] P. Karchin, "*A Scintillator-based Muon Detector for the Linear Collider,*"
in proceedings of the meeting of the Division of Particles and Fields of the American Physical Society, University of California, Riverside
, August, 2004, International
Journal of Modern Physics A, World Scientific Publishing Company.

[11] R. Abrams et al., *LC scintillator-based muon detector tail-catcher R&D.* FERMILAB-CONF-07-589-E, LCWS-2007-CAL14, Nov 2007. 5pp. International Linear Collider Workshop (LCWS07 and ILC07), Hamburg, Germany, 30 May - 3 Jun 2007, SLAC eConf C0705302 Proceedings, S. Riemann (ed.).

Appendix: Simulating the Silicon Detector

Using the fast and flexible detector simulation package developed by the ALCPG Simulation and Reconstruction group, over fifty different detector designs were modeled during the course of this LOI exercise before selecting the baseline design. A somewhat simplified geometry, called sid02, was used for the large-statistics detector response simulations used for the physics benchmarking analyses. For reference, we include here a fairly complete textual description of the sid02 baseline detector. Full details can be found at **http://confluence.slac.stanford.edu/display/ilc/sid02**.

In addition, another model, called sidloi, was developed to more closely represent the engineering drawings of the individual subdetectors described in the subsystems chapter of the LOI.

0.1 sid02

0.1.1 Beampipe

The beampipe is composed of three sections: a cylindrical central tube and forward and backward conical sections. The central tube has an inner radius of 1.2cm and a z extent of $\pm$ 6.251cm and is made of 0.040cm thick beryllium. The conical sections are 0.875mm thick beryllium and flare from 1.2cm inner radius at 6.25cm to 8.2cm at the edge of the tracking region. The beam pipe has a titanium inner liner 0.0025cm thick for the central barrel section and 0.0075cm thick for the conical sections.

0.1.2 Vertex Detector

The vertex detector is composed of a central barrel system with five layers and forward systems composed of four disks. The barrels are all 12.5cm long and are composed of 0.0113cm silicon, of which the outer 0.002 is sensitive. The inner radii of the layers are:

1.46, 2.26, 3.54, 4.8, 6.04cm.

There are four forward disks on either end, composed of a total of 0.0113cm of silicon, of which the inner 0.002cm is sensitive. All of the disks extend to a maximum radius of 7.1cm. The z positions and inner radii for the four disks are:

z (cm)	inner radius (cm)
7.18	1.4
9.02	1.6
12.16	1.8
17.0	2.0

The entire vertex detector is enclosed within a double walled carbon fiber support tube. The support tube walls are 0.05cm thick carbon fiber with inner radii of 16.87cm and 18.42cm and a $|z|$ extent of $|z|$ <89.48cm. The ends of the support tube are double-walled disks of 0.05cm thick carbon fiber disks.

The mechanical supports for the endcap disks are modeled as carbon fiber rings with a reduced density of 25% to reflect the lightening holes in the real structures. The VXD utility mixture of cooling channels, cables and fibers etc. is represented by layers of G10 and copper at the endplates, extending down to the beampipe and exiting the detector along the beampipe.

0.1.3 Tracker

The tracker is composed of five cylindrical barrels with four disk-shaped endplanes. The z extent of the barrels increases with radius and the endplane for each extends beyond its cylinder in radius to provide overlap. The sensitive medium is silicon, assembled into carbon-fiber/Rohacell/PEEK modules and read out via a bump-bonded chip and Kapton/copper cables. These modules are supported by carbon-fiber/Rohacell/carbon-fiber barrels or disks. Each barrel cylinder is supported from the next barrel out by an annular carbon fiber-ring. Outside each of these support rings in z, G10/copper printed circuit boards are mounted for power and readout distribution to all silicon modules in a layer.

Barrels The radii and z extent of the barrel silicon are:

layer	z (cm)	inner radius (cm)
1	55.8	21.8
2	82.5	46.8
3	108.3	71.8
4	134.7	96.8
5	160.6	121.8

For the barrels, the support tubes are composed of 0.05cm carbon fiber, 0.8cm of Rohacell31 (15% coverage) and 0.05cm carbon fiber. The sensor modules for the barrel are single-sided and have 0.03cm of silicon mounted on carbon fiber/Rohacell31 frames that clip into PEEK (Polyetheretherketone) mounts. The average thickness of the carbon fiber, Rohacell31 (50% coverage) and PEEK in the modules of each barrel layer are 0.016cm, 0.28cm and 0.02cm repectively. The average thicknesses of the readout materials are 0.00048cm of silicon, 0.0064cm of Kapton and 0.00065cm of copper, however, the thickness of the cable material varies by layer.

Endcap The z positions and radial extents of the endcap silicon are:

layer	inner radius (cm)	outer radius (cm)	z (cm) for u plane	z (cm) for v plane
1	20.7	49.4	85.5	85.9
2	20.7	74.7	111.4	111.8
3	20.7	99.9	137.8	138.2
4	20.7	125.0	163.6	164.0

where each layer is composed of two sensor modules to measure coordinates in two stereo (u-v) views. The forward disk supports are composed of .05cm carbon fiber, 0.63cm Rohacell31 (15% coverage) and 0.05cm of carbon fiber. There are two sensor modules mounted outside of the disks to provide stereo measurements and have 0.03cm of silicon mounted on either side of carbon fiber/Rohacell31 frames that clip into PEEK (Polyetheretherketone) mounts. The average thickness of the carbon fiber, Rohacell31 and PEEK in the modules of each disk double-layer is assumed to be the same as that for the barrel modules.

0.1.4 Calorimeters

Electromagnetic Calorimeter This element sets the basic size and aspect ratio for the rest of the detector. The inner radius for the barrel is 127cm. The aspect ratio is set to cosine(theta)=0.8, meaning the inner z of the endcap EM calorimeter is at z of 168cm. The EM calorimeter is a sampling calorimeter composed of 20 layers of:

material	thickness (cm)
Tungsten	0.250
Silicon	0.032
Copper	0.005
Kapton	0.030
Air	0.033

This is followed by ten layers of the same readout, but doubled thickness of tungsten. There is a sensitive silicon layer before the first layer of tungsten to provide additional electron/photon discrimination, giving a total of 31 layers of silicon readout. The tungsten alloy being used is TungstenDen24 (93% W, 6.1% Ni, .9% Fe) with a density of 17.8 g/cm^3.

The endcap plug sits inside the barrel cylinder, so the barrel z extent is $\pm$ 182cm. The endcap starts at an inner radius of 20cm and extends out to 126.5cm.

Hadron Calorimeter The hadron calorimeter is a sampling calorimeter composed of 40 layers of

material	thickness (cm)
Steel	2.0
PyrexGlass	0.11
RPCGas	0.12
PyrexGlass	0.11
G10	0.3
Air	0.16

It begins immediately outside of the EM calorimeters, with the endcap plug sitting inside the barrel. The barrel inner radius is 141cm with a z extent of ± 294cm. The endcap extends from an inner radius of 20cm to an outer radius of 140.75cm, inner z of 182cm.

0.1.5 Solenoid

The solenoid is modeled as a cylinder with an inner radius of 255cm. This is larger than the outer radius of the hadron calorimeter since we will not be building a cylindrical detector, but a polygonal one (current thinking is dodecagonal). The barrel composition is as follows:

material	thickness (cm)	z (cm)
Steel	6.0	271.0
Air	8.5	271.0
Aluminum	39.3	262.5
Steel	6.0	262.5
Air	20.0	271.0
Steel	3.0	271.0

This is capped with disk endplates of 6cm steel from r=250cm to 332.8cm. The field is solenoidal, constant 5 Tesla along z up to half the coil thickness and -0.6 outside.

0.1.6 Muon System

The muon system is composed of 11 layers of 20cm thick iron plates interspersed with double RPC readout. The barrel inner radius is 338.8cm with z extent of ± 294cm. The endcap sits outside the barrel at an inner z of 303.3cm and radius from 20.0cm to 608.2cm.

0.1.7 Masks and Far Forward Detectors

The far forward region is designed for the 14mr beam crossing solution so has separate incoming (inner radius 1.0cm) and outgoing (inner radius 1.5cm) beampipes. The far forward plug is designed to fit within a radius of 20cm. It starts with an electromagnetic calorimeter (LumiCal) with the same composition as the endcap calorimeter, extending from 6.0cm out to 19.5cm. The calorimeter is backed up by a conically tapered tungsten mask, inner radius 8.0cm at z of 182cm, tapering to 16cm at z of 313.5cm. The outer radius is constant at 15.5cm. There is a far forward low-Z shield (12.39cm thick Borated polyethylene) at z of 282cm. This is followed by a 50 layer silicon-tungsten calorimeter (BeamCal)at z of 295cm.

0.2 sidloi

The sidloi detector model is intended to reflect the design of the Silicon Detector, as described in this LOI, as faithfully as possible. All of the tracker elements are therefore modeled as planar silicon wafers with their attendant support structures. The readout geometry is simplified, but reflects the gross amount and general distribution of the materials. The calorimeters are modeled as polygonal staves in the barrel region or planes in the endcaps, with interleaved readouts. The complexity of this detector model does not lend itself to a simple textual description. We therefore present a few figures to give an indication of the detail implemented in this model. A full three-dimensional model built from the Geant geometry is available in PDF at **http://silicondetector.org/download/attachments/46170132/sidloi3D.pdf**

A cross section of the tracking detector is shown in Figure 1. This is to be compared with Figure 2 (Figure 2.5 in the LOI) which shows an engineering elevation view of the tracking system. An orthographic cutaway view of the central tracker as implemented in the sidloi model is shown in Figure 3. An orthographic cutaway view of the complete detector as implemented in the sidloi model is shown in Figure 4. The electromagnetic barrel calorimeter is modeled as a dodecagonal tube with overlapping staves. The main difference between this model and the LOI engineering design is the hadron calorimeter barrel. In this implementation it is built of twelve symmetric staves, as opposed to the model described in Section 2.2.3.1 of the LOI. The effect of projective cracks on the detector performance is still being studied. Finally, the octagonal layout of the magnetic flux return yoke, with its eleven layers of muon detection instrumentation is clearly visible. An X-Y cross section of the sidloi model at z=0 is shown in Figure 5. Finally, a Y-Z quadrant of the sidloi model is shown in Figure 6.

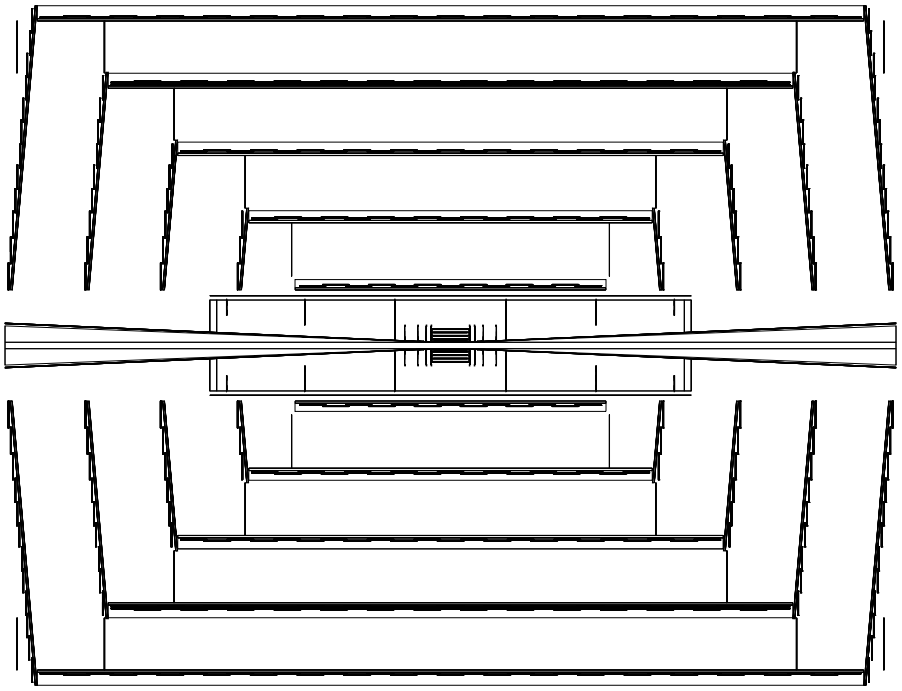

Figure 1: R-z view of the tracking system as implemented in sidloi. Some support and readout structures have been hidden to improve the visibility of sensors.

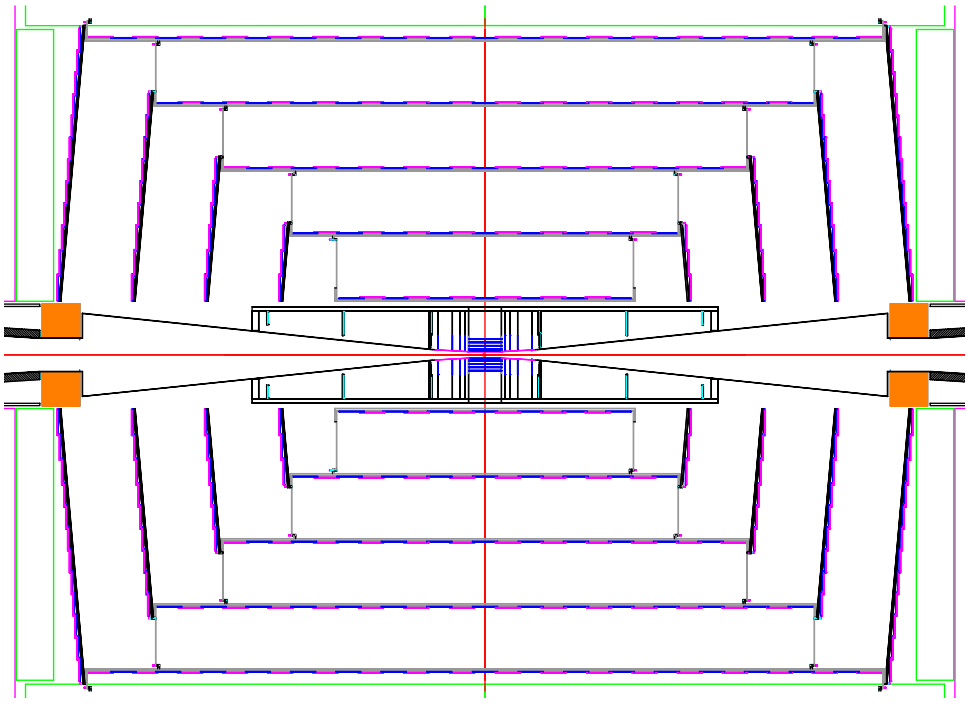

Figure 2: R-z view of the tracking system.

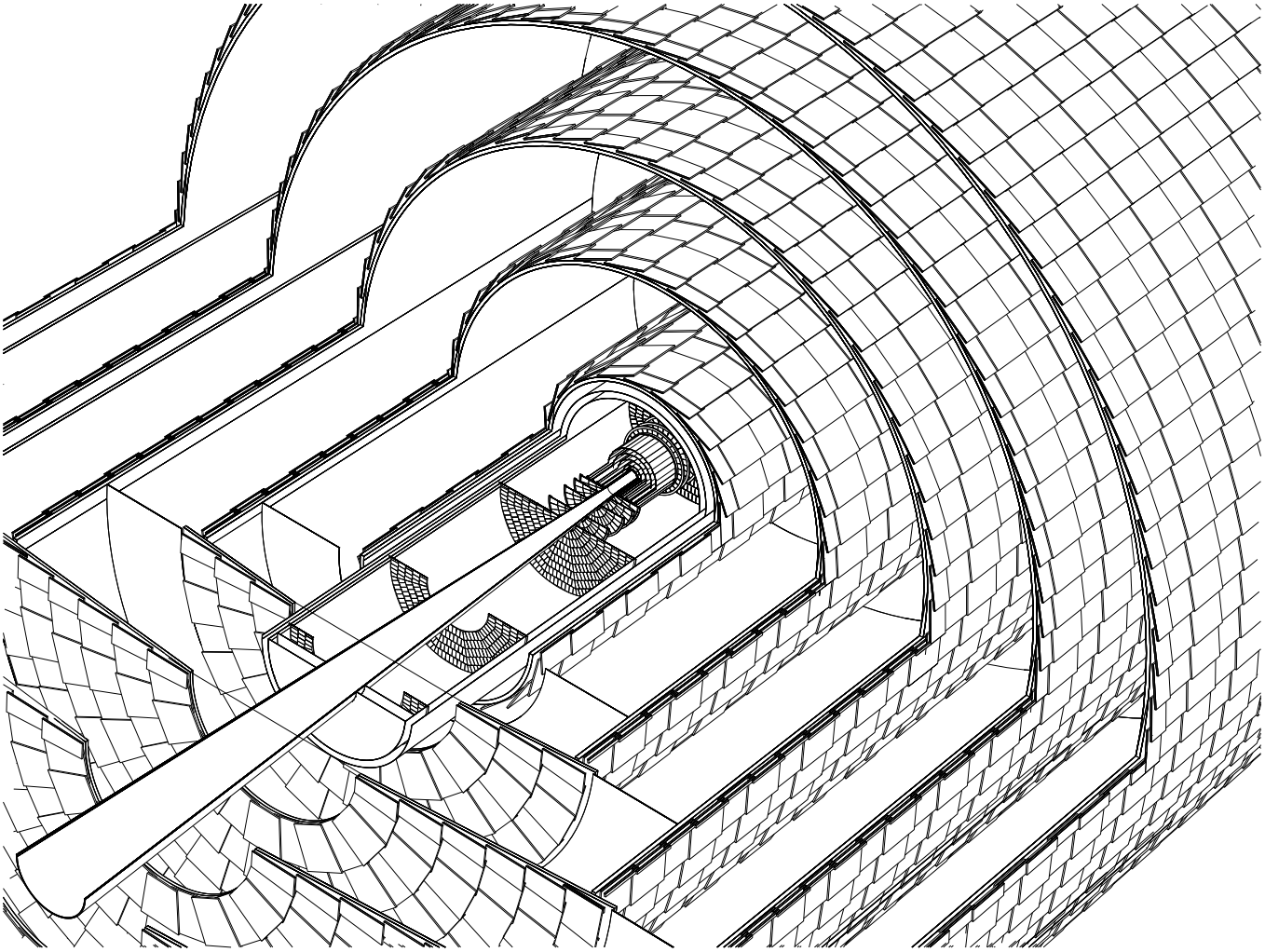

Figure 3: Cutaway view of the tracking system as implemented in sidloi. Some support and readout structures have been hidden to improve the visibility of sensors.

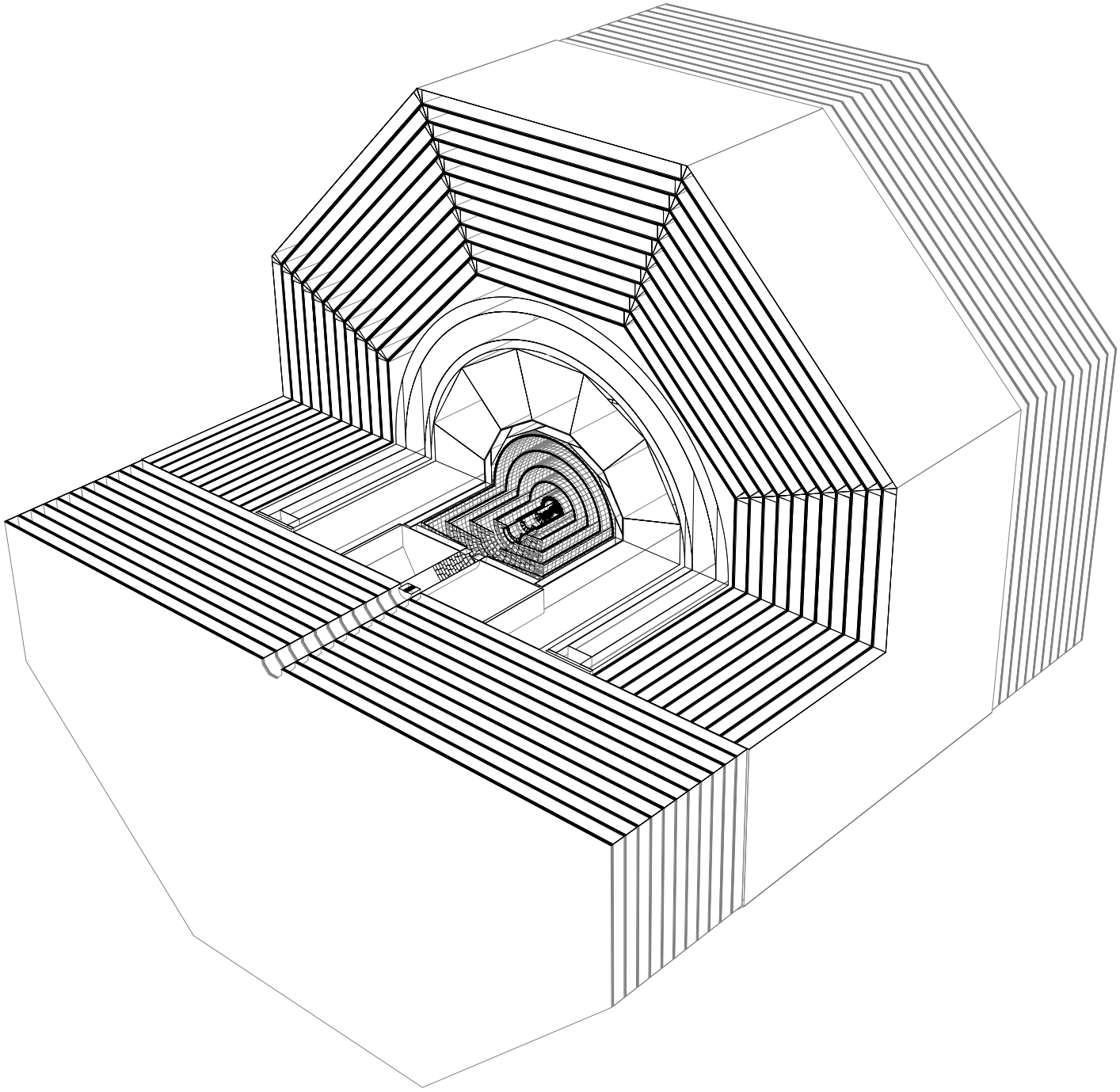

Figure 4: Cutaway view of the Silicon Detector as implemented in sidloi. Some support structures and layering details in the calorimeters have been hidden to improve the visibility of the model.

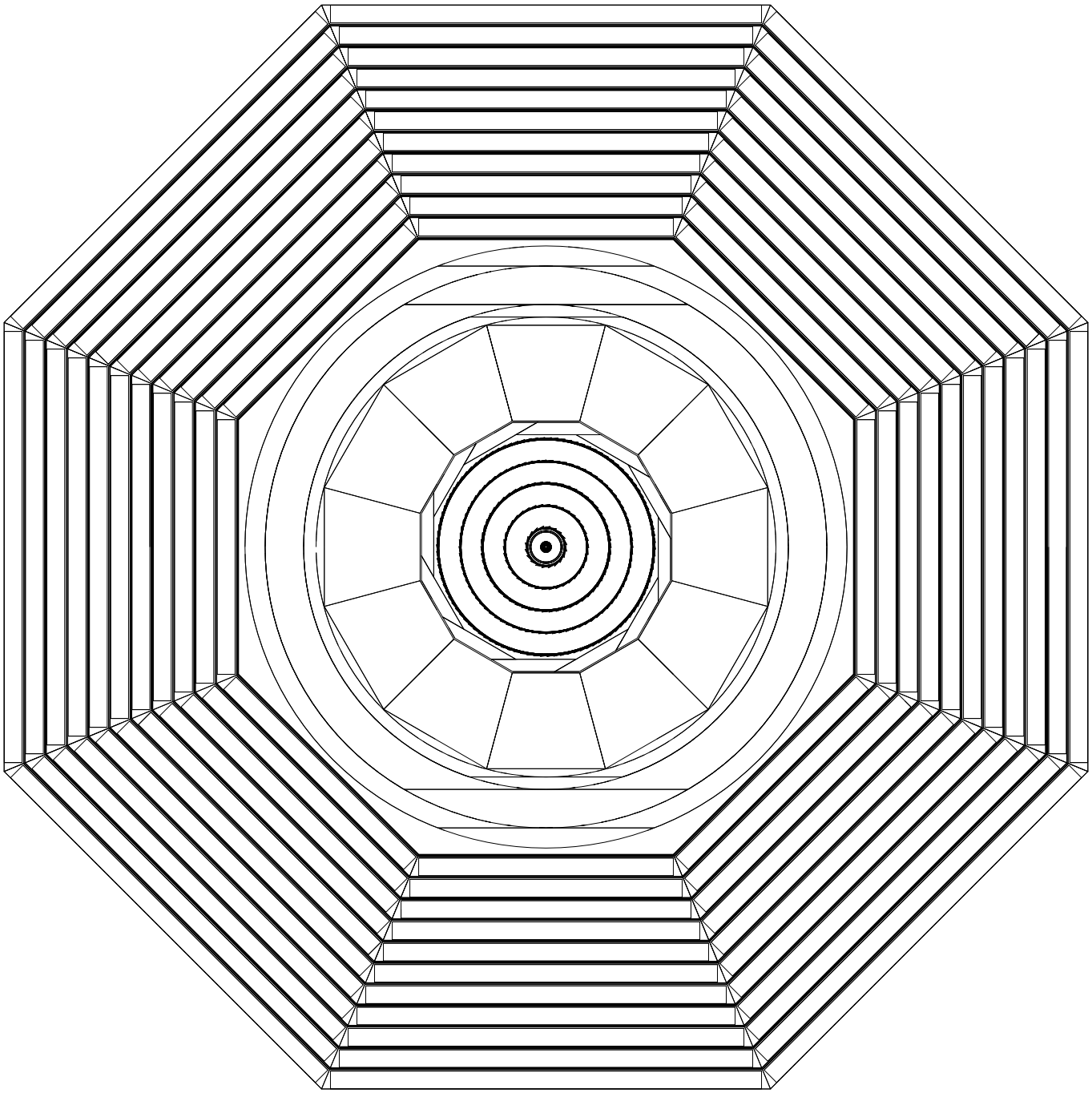

Figure 5: X-Y Cross section view through the center of the Silicon Detector as implemented in sidloi. Some support structures and layering details in the calorimeters have been hidden to improve the visibility of the model.

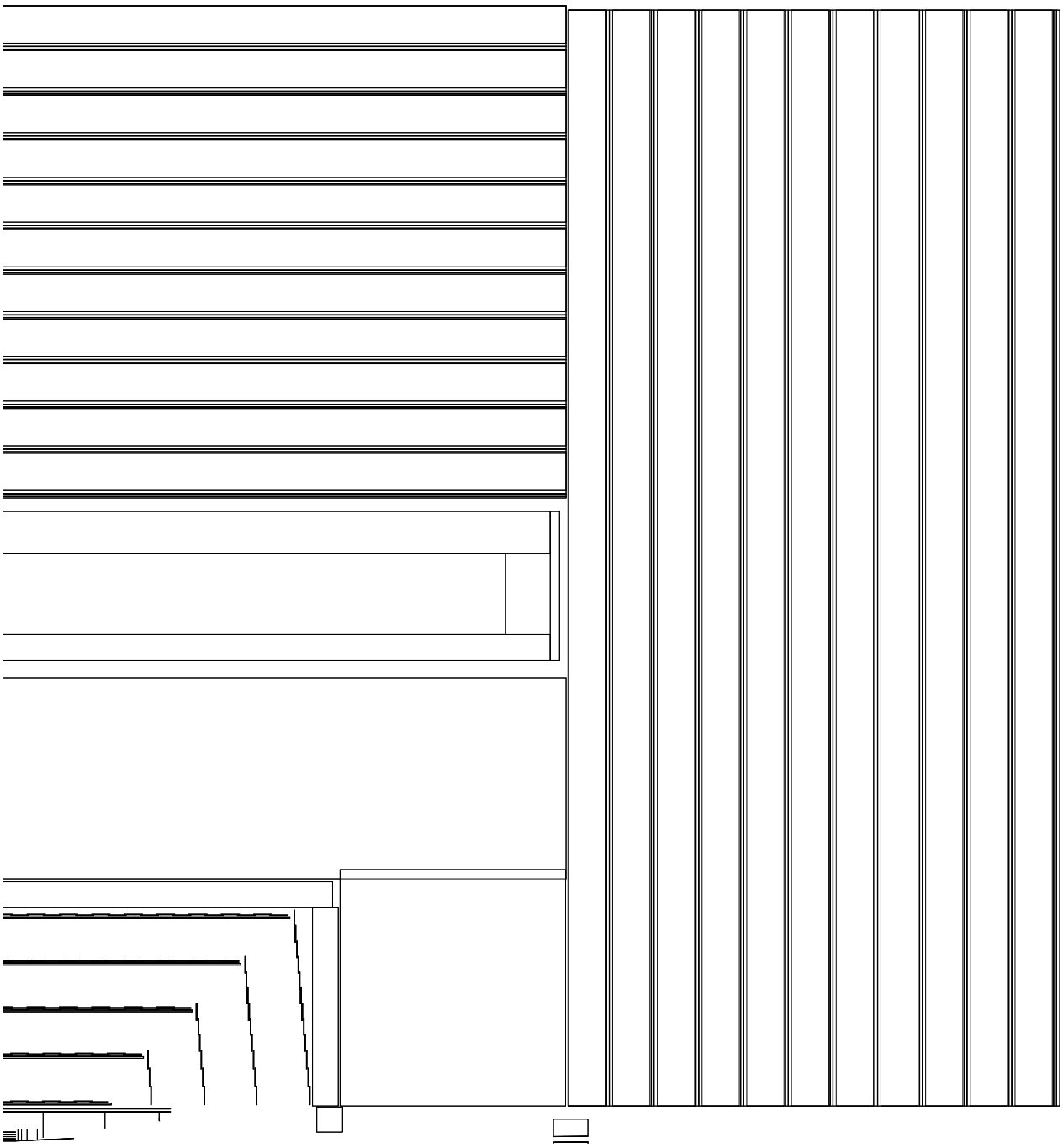

Figure 6: Y-Z Quadrant view of the Silicon Detector as implemented in sidloi. Some support structures and layering details in the calorimeters have been hidden to improve the visibility of the model.

The SiD Particle Flow Algorithm

M.J. Charles[1,2], U. Mallik[1], T.J. Kim[1], R. Cassell[3]

1- University of Iowa, Iowa City, Iowa 52242, USA
2- Oxford University, Oxford, United Kingdom
3- Stanford Linear Accelerator Center, Stanford, California 94309, USA

March 30, 2009

Abstract

A PFA has been developed for the SiD detector concept at a future Linear Collider. The algorithm is descibed in detail and the performance of the version of the algorithm used in the SiD LOI is presented for a number of physics processes with two hadronic jets.

1 Introduction

Reconstruction in SiD is based on the Particle Flow concept in which calorimeter energy deposits from individual particles are separated, allowing the energy of each particle to be measured in the optimal subsystem for that particle (the silicon tracker for charged particles, the EM calorimeter for photons, both calorimeters for neutral hadrons). In the limit of perfect separation, the contribution to the jet energy resolution from charged particles is negligible and only neutral hadrons need to have their energy measured in the hadronic calorimeter, leading to a jet energy resolution of roughly[1] $20\%/\sqrt{E}$ [1]. In practice, this limit is difficult to achieve. Degradation of the resolution due to imperfect separation of energy deposits is generically referred to as confusion, and is the most important effect for well-contained, high-energy jets in the SiD acceptance. A particle-flow algorithm (PFA) has been developed and tuned for SiD in the `org.lcsim` software framework with the goal of minimizing the confusion and therefore the resolution. A snapshot of the PFA has been used for the analysis and benchmarking results reported in this LOI; development is still in progress and performance is expected to continue improving in future versions.

A deliberate effort has been made to keep the code as modular as possible. Different components communicate with one another by reading and writing named objects in standard formats to the event-level data store. This makes the flow of information clear, and allows one component to be substituted for another.

2 Algorithm description

For each event, the SiD PFA takes as inputs the energy deposits in the calorimeters and muon system and the set of tracks found in the tracking system (as described in Reference [2]). The PFA then performs the reconstruction in a series of steps, described below. The general strategy for

[1] E is in units of GeV throughout.

pattern-recognition in the calorimeters is (a) to identify and set aside the easiest, most distinctive showers first, taking maximum advantage of the information, and (b) to recognize common classes of mistakes made earlier in the algorithm and correct for them. The PFA produces as output a collection of reconstructed particles suitable for use in a physics analysis. The first step is to prepare and validate the input. The track reconstruction and calorimeter hit digitization packages are run, and any data which are unphysical or unmeasureable—such as calorimeter hits below an energy threshold or occuring more than 100 ns after the primary interaction—are removed.

The second step is to reconstruct electrons, muons, and photons, since these have distinctive signatures in the calorimeters. Muons are identified by extrapolating tracks through the ECAL and HCAL and requiring them to connect to a MIP stub in the muon system. Electromagnetic showers in the ECAL are reconstructed and identified with a dedicated "photon-finder" clustering algorithm. If the shower is connected to a track whose momentum matches the shower energy, it is taken to be an electron; if it is not connected to any track then it is taken to be a photon; and if it is connnected to a track with the wrong momentum then it is flagged as potentially mis-reconstructed. The latter can occur if the calorimeter deposits of a charged particle and a photon overlap, or if part of a hadronic shower is misidentified as a photon.

The third step is to reconstruct MIP segments in the calorimeters. Hadrons often travel a significant distance before showering and leave a distinctive signature of isolated hits. We find these by propagating each non-leptonic track through the calorimeter, layer by layer, until we can no longer find isolated or semi-isolated hits, either because the MIP segment has ended (typically with a hadronic shower) or because it has overlapped with the shower of another particle.

After setting aside the identified electrons, muons, photons, and MIP segments, the remaining hits are expected to be from hadronic showers. We now use a series of clustering algorithms to find the main structure of these showers. We begin with the DirectedTree clusterer, which groups hits around local maxima in hit density and is quite effective at matching peripheral elements of showers to the correct shower core. This serves as a useful guide in cases where there is little topological information, and in particular plays a large role in the fuzzy clustering step described later. However, the DirectedTree clusters are relatively coarse-grained and do not have the purity we need. We therefore make additional clustering passes, looking for substructure within the DirectedTree clusters: track segments, or dense clumps of hits. This substructure will then form the skeletons of the hadronic showers, together with MIP segments found earlier (and a number of special cases such as DirectedTree clusters with no identified substructure).

We assemble the skeletons of the hadronic showers with an iterative algorithm. We begin with the non-leptonic tracks, each of which is connected to a "seed" cluster in the ECAL—often, but not always, a MIP segment. Starting with the seed, we add clusters to the skeleton. The clusters to add are chosen based on a score which describes how well-connected a pair of clusters is. The way the score is calculated depends on the kind of clusters involved—for example, for a pair of MIP/track segments in the calorimeter we use a likelihood selector taking as inputs the distance of closest approach of the extrapolated track segments, the proximity of the hits in the clusters to the point of closest approach, and whether the point of closest approach is in the calorimeter. We build up the shower recursively, adding clusters which have high scores to be connected to the seed, then looking for further clusters which have high scores to be connected to the ones just added, and so on. We stop when there are no more clusters with high enough scores to add, or when the energy of the shower would become too large compared to the momentum of the track (by default we require $E - p < \sigma$). We then move on to the next track and begin the same process again—except that the clusters we just assigned are no longer available.

After attempting to reconstruct a shower for each track, we look for common mistakes. The reconstruction is fairly conservative by default, and sometimes misses parts of a shower for one of two reasons. Firstly, the score connecting the cluster to the rest of the shower may be too low to pick it up; we deal with this by loosening the score requirement if the cluster energy is too low ($E < |p| - \sigma$). Secondly, if the shower energy has an upward fluctuation it may be prevented from adding all of its clusters; we deal with this by loosening the requirement on $E - p$ in cases where the shower was prevented from picking up a cluster for this reason and the cluster was not subsequently assigned to another shower and the current shower does not already have a high energy compared to the track momentum. When loosening these requirements, we make a relatively small change at each iteration to avoid over-compensating.

In each iteration, the tracks are considered in order of increasing momentum: the reason for this is that lower-momentum tracks have smaller showers which are generally easier to reconstruct, so the risk of incorrectly adding clusters from another shower is reduced. However, in some cases two or more showers are badly overlapped and we are unable to separate them. In this case we group them together for the purposes of shower reconstruction, adding clusters that connect to any of them and requiring that the combined shower energy balance the sum of the tracks' scalar momenta.

After the last clustering iteration, we make final attempts to identify and correct mistakes in the charged hadronic showers. We look for showers whose energy is too low compared to the track momentum and for clusters that were not assigned to any shower, and attempt to match the two. We also look for unassigned clusters downstream of a shower whose energy is too low—these can be caused by secondary neutrals.

In addition to the skeletons of the hadronic showers, we have a large number of individual hits and small clusters whose association is not clear. These typically come from secondary photons or from soft neutrons displaced from the detector material during a hadronic shower. The most likely source is the nearest shower, but since there is little pointing information and secondary neutrals can sometimes travel a significant distance, this may not be correct. We handle this case with a fuzzy clustering technique: the energy in these small fragment clusters is split between any nearby showers which could have contributed in a probabilistic way, favouring closer showers over distant ones. Where possible, this sharing uses information from the DirectedTree clustering pass: fragments which are inside a DirectedTree envelope cluster are shared preferentially with showers inside the same DirectedTree cluster. This energy sharing is handled implicitly throughout the shower-building process, so that associated fragments are taken into account when testing the energy of a shower during reconstruction.

At this point, the only remaining clusters should be from neutral hadrons. We apply a simplified version of the charged hadron reconstruction to these clusters—since there is no track, we cannot make energy-momentum comparisons and there is no need to iterate—and form neutral hadron showers. (Some of these may be misidentified photons; we look for special cases such as when the cluster was flagged earlier as a photon-MIP overlap and move them to the photon list instead.)

The final step is to produce a list of reconstructed particles suitable for physics analysis. This list contains electrons, muons, charged hadrons, neutral hadrons, and photons. The momentum of each charged particles is taken from its track fit; together with the appropriate mass hypothesis (e, μ, π) this defines the four-vector. The energy and direction of neutral particles are computed from the calorimeter energy deposits, and the four-vector is again defined assuming the appropriate mass hypothesis (K_L or γ). We also consider tracks which were not matched to energy deposits in the calorimeter as a special case. If the track lies outside the calorimeter acceptance then we

assume the particle was real and missed, and therefore add it to the output with the pion mass hypothesis. If the track is inside the calorimeter acceptance then the most likely explanations are that the track-cluster matching failed or that the track decayed or interacted before reaching the calorimeter; in either case the energy of the particle reached the calorimeter and will likely already have been included (e.g. as a neutral hadron), so to avoid double-counting we do not put an additional particle with the track's three-momentum in the output.

3 Performance

The true test of performance is the sensitivity to key physics observables—this is discussed in Reference [4]. However, for the purposes of studying and optimizing a PFA it is helpful to look at specific physics processes which are simple to analyse and depend primarily on the quality of the PFA output. We use two such processes:

- $e^+e^- \to q\bar{q}$ at $\sqrt{s} = 100, 200, 360, 500$ GeV, for $q = u, d, s$. Beamstrahlung and bremstrahlung in the initial state are disabled so that the collision energy $E_{\rm CM}$ is the same as $\sqrt{s}$. The figure of merit is the event energy sum residual $\Delta E_{\rm CM}$, i.e. the signed difference between the reconstructed and true values of $E_{\rm CM}$. Plots of the residual distribution are shown in Figure 1. Under the simplifying assumption that the invariant mass of two jets with energies E_1 and E_2 and opening angle θ_{12} is given by $m_{12}^2 = 2E_1E_2(1 - \cos\theta_{12})$, the resolution of energy sum residuals is equal to the resolution of the dijet mass for jets of the same energy.

- $e^+e^- \to Z(q\bar{q})Z(\nu\bar{\nu})$ at $\sqrt{s} = 500$ GeV, for $q = u, d, s$. The figure of merit is the dijet mass residual ΔM, the signed difference between the reconstructed and true values of $m_{q\bar{q}}$. Plots of the residual distribution are shown in Figure 2.

In both cases, the figure of merit depends upon the quality of hadronic jet reconstruction but does not require jet-finding or corrections for primary neutrinos.

Table 1 shows the measured resolutions[2] for the `sid02` detector. The resolution is quoted separately for the barrel ($0 < |\cos(\theta)| < 0.8$) and endcap ($0.8 < |\cos(\theta)| < 0.95$) regions of polar angle. There are several effects at work:

- The calorimetric component of the resolution function is expected to scale as $\sqrt{E}$, i.e. slower than linear. When this dominates, the fractional resolution ($\sigma_{\Delta E_{\rm CM}}/E_{\rm CM}$) decreases as the energy goes up.

- The confusion component of the resolution function will increase as the jet energy goes up and pattern-recognition becomes harder. The energy-dependence is not known from first principles, but it is likely to be at least linear if not faster.

- At high energies, leakage of energy out of the back of the calorimeter becomes important. The impact on the resolution has a strong angular dependence, since the effective depth of the calorimeter varies with $\cos\theta$; this is illustrated in Figure 3. This effect is modest for jet energies of 180 GeV but becomes dominant by 250 GeV. It is partially mitigated in the endcap region by using the muon system as a tail-catcher; this depends strongly on the longitudinal

[2]Resolutions are quoted in terms of rms_{90}, the RMS of the contiguous block of 90% of events with smallest RMS. Similarly, μ_{90} is defined to be the mean of these events. Note that for a Gaussian distribution, the rms_{90} is approximately 78% of the full RMS.

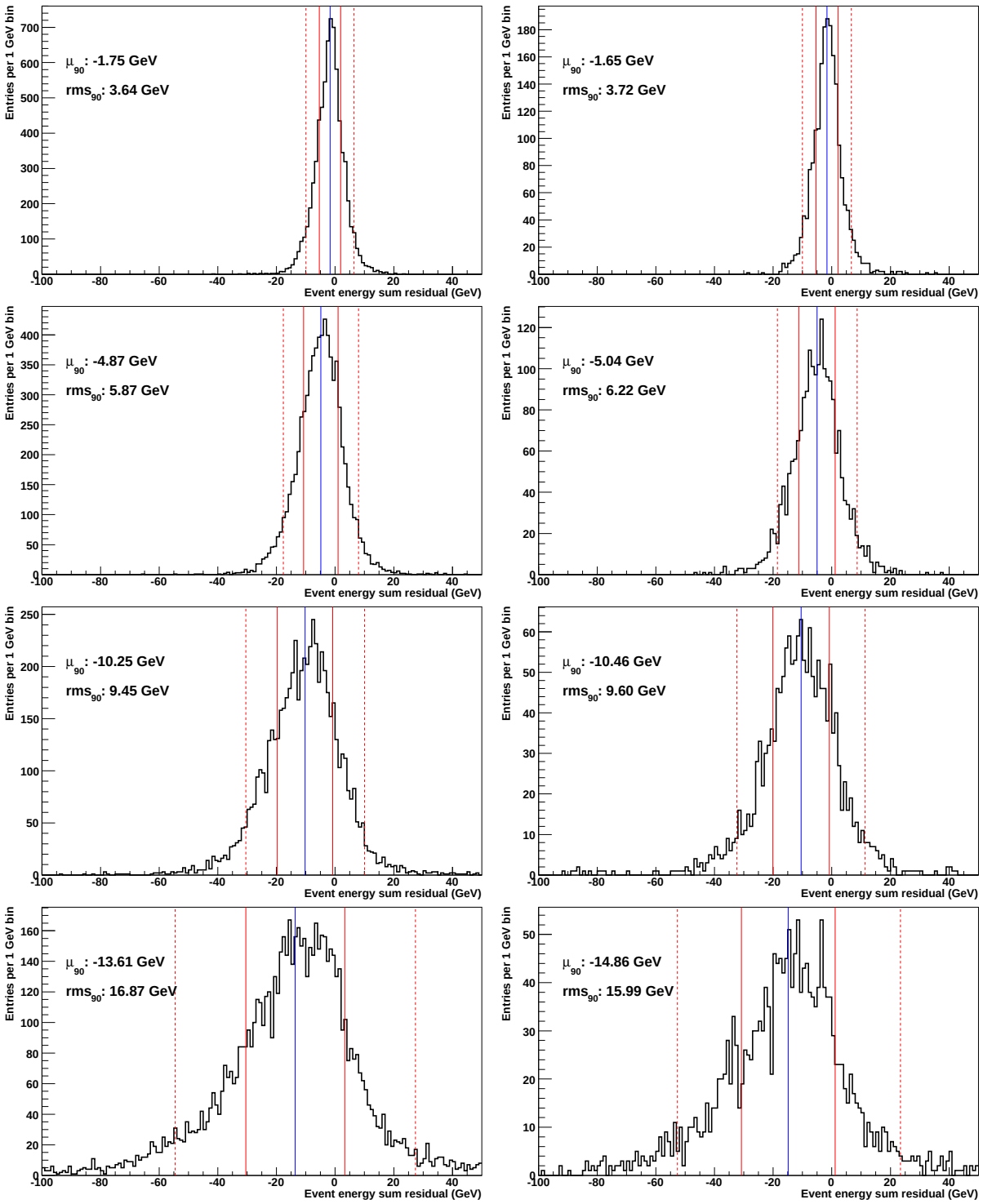

Figure 1: Energy sum residuals for $e^+e^- \to q\bar{q}$ events at $\sqrt{s} = 100, 200, 360, 500$ GeV (top to bottom), shown for the barrel (left) and endcap (right) regions of polar angle. The dashed lines indicate the 90% of events with smallest RMS, and the solid lines indicate the mean and RMS of those events.

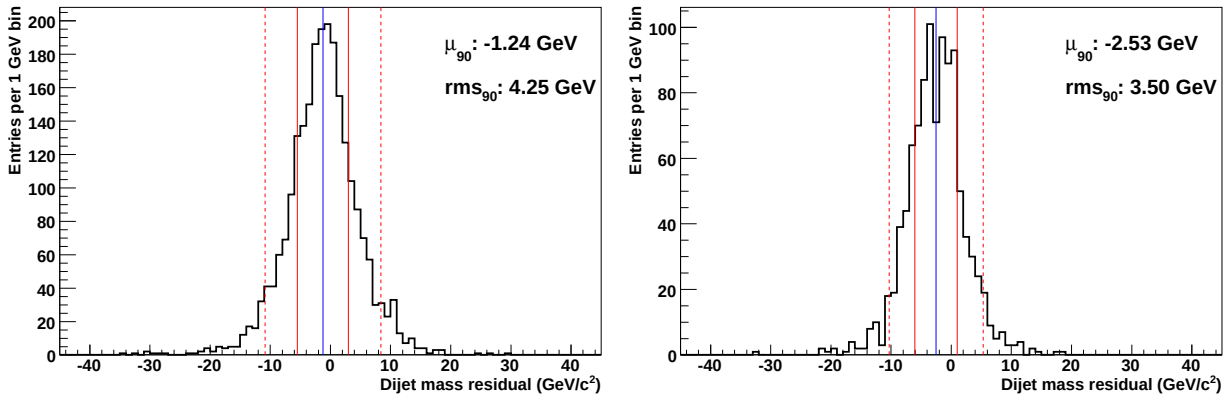

Figure 2: Dijet mass residuals for $e^+e^- \to Z(q\bar{q})Z(\nu\bar{\nu})$ events at $\sqrt{s} = 500$ GeV, shown for the barrel (left) and endcap (right) regions of polar angle. The dashed lines indicate the 90% of events with smallest RMS, and the solid lines indicate the mean and RMS of those events.

	Resolution (real tracking)		Resolution (cheat tracking)	
Process	Barrel	Endcap	Barrel	Endcap
$e^+e^- \to q\bar{q}$, $\sqrt{s} = 100$ GeV	3.7%	3.8%	3.4%	3.5%
$e^+e^- \to q\bar{q}$, $\sqrt{s} = 200$ GeV	3.0%	3.2%	2.8%	3.0%
$e^+e^- \to q\bar{q}$, $\sqrt{s} = 360$ GeV	2.7%	2.7%	2.6%	2.6%
$e^+e^- \to q\bar{q}$, $\sqrt{s} = 500$ GeV	3.5%	3.3%	3.5%	3.4%
$e^+e^- \to Z(q\bar{q})Z(\nu\bar{\nu})$	4.7%	3.9%	4.2%	3.7%

Table 1: PFA performance for `sid02`. For the $e^+e^- \to q\bar{q}$ processes, the rms_{90} of the energy sum residuals is quoted as a fraction of $\sqrt{s}$, and for the $e^+e^- \to ZZ$ process the rms_{90} of the dijet mass residuals is quoted as a fraction of m_Z. Resolutions are quoted for the LOI production snapshot and do not include subsequent improvements.

segmentation in the muon system and was found to be much more effective with an absorber thickness of 5 cm than 20 cm.

- For the ZZ events, the requirement that both jets lie in the angular region of interest constrains the kinematics of the decay.

- The dijet mass resolution measured in $e^+e^- \to ZZ$ events is observed to be larger than the resolution seen in $e^+e^- \to q\bar{q}$ events, even when the jet energy is comparable. This may be due to non-linearity in the energy response: the $e^+e^- \to q\bar{q}$ events have mono-energetic jets by construction and so a non-linear response would simply shift the mean of the energy sum distribution, whereas the jets in $e^+e^- \to ZZ$ events can be quite asymmetric and therefore the dijet mass residual distribution would be broadened by such an effect.

The resolutions in Table 1 are larger than those seen when running the PandoraPFA algorithm on the ILD detector design [5]. Understanding this difference is not straightforward: the performance of a PFA and the design of the detector on which it runs are coupled and it is not meaningful to take either in isolation. It is also technically very difficult to run one PFA on the other detector. However, a work-around has been developed: by starting from the LDC00Sc detector and adjust-

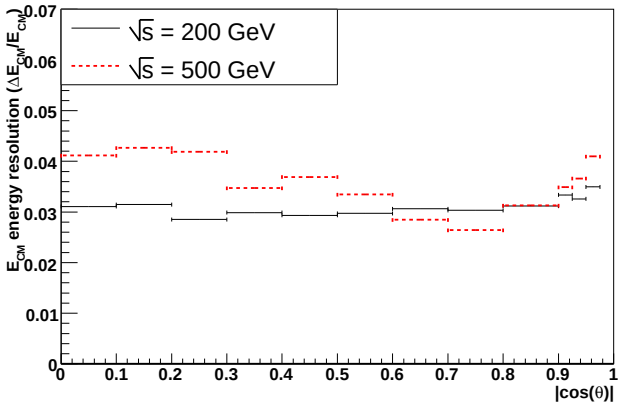

Figure 3: Resolution (rms_{90} of the energy sum residuals) as a function of angle for $e^+e^- \to q\bar{q}$ for $\sqrt{s} = 200, 500$ GeV. For 200 GeV (solid), leakage is not significant and the angular distribution is roughly flat, rising slowly towards $|\cos\theta| = 0.975$ as the effects of acceptance and tracking become important. For 500 GeV (dashed), leakage has a major impact—this can be seen from how the resolution varies in the barrel between $|\cos\theta| = 0$ where the calorimeter thickness is minimized to $|\cos\theta| = 0.8$ where it is greatest. For both energies, the resolution is very bad for $|\cos\theta| > 0.975$ due to acceptance losses.

ing the calorimeter geometry and layering, we can produce "SiDish" detectors which have similar dimensions to `sid02` and run PandoraPFA v2.01[3] on them [6]. Note that the SiDish detectors still use the same detector technology as LDC00Sc, though: a TPC tracker and iron/scintillator HCAL, unlike SiD's silicon tracker and iron/RPC HCAL.

The $e^+e^- \to q\bar{q}$ event energy sum resolution in $0.0 < |\cos\theta| < 0.7$ found when running PandoraPFA on SiDish detectors resembling `sid02` is 3.1% for $\sqrt{s} = 90$ GeV and 2.8% for $\sqrt{s} = 200$ GeV, superior to the performance we find in Table 1 (3.7% and 3.0%, respectively). Part of this difference is due to the difference between `sid02` and the SiDish detectors. In previous studies comparing SiD detectors with scintillator and RPC instrumentation of the HCAL, we found that the scintillator variant had better performance by about 10% relative (0.3% absolute). Likewise, the use of a TPC tracker gives more complete information for decays and interactions inside the tracking system (e.g. for $K_S \to \pi^+\pi^-$); we can place an upper bound on this of 0.3% for $\sqrt{s} = 100$ GeV and 0.2% for $\sqrt{s} = 200$ GeV from studies with cheat tracking. These effects are sufficient to explain most of the observed performance difference between PandoraPFA and the SiD PFA.

4 Conclusions

There has been a great deal of progress in SiD reconstruction since ALCPG07. We have switched to full track reconstruction and found that PFA performance in $e^+e^- \to q\bar{q}$ events remains close to that of cheat tracking. The PFA itself has been largely rewritten and gives event energy sum resolutions of order 3.0–3.5% for jet energies up to 250 GeV. The PFA performance was found to be approaching that of the gold standard, PandoraPFA, when running on a comparable detector design for jet energies up to 200 GeV. This is very encouraging for the jet physics prospects at SiD.

Nonetheless, there is a great deal of improvement still to come. A number of code fixes have

[3] PandoraPFA has continued to develop while this study was carried out; at the time of writing the current version is v03-β.

already been made [3] and more substantial revisions such as the integration of calorimeter-assisted tracking [7] are planned. At the broadest level, the two principal challenges are: (1) to understand the impact of leakage in high-energy jets on the physics potential of the detector, and to reduce it by adapting the algorithm and detector design if needed; and (2) to improve the reconstruction algorithm, and in particular to reduce the dijet mass resolution seen in $e^+e^- \to ZZ$ events. The confusion term still dominates the resolution for the range of jet energies likely to be used in physics analyses at a 0.5 TeV or even 1 TeV collider: we have plenty of room for improvement.

References

[1] R.E. Cassell, *SiD: Separating Detector Performance from PFA Confusion*, LCWS08, Chicago.

[2] R. Partridge, *SiD Track Reconstruction*, LCWS08, Chicago.

[3] T.J. Kim, *Implementation of PFA and Muon Identification*, LCWS08, Chicago.

[4] T.L. Barklow, *Status of SiD Benchmarking*, LCWS08, Chicago.

[5] D.R. Ward, *PFA Progress and ILD Detector Optimization*, LCWS08, Chicago.

[6] M. Stanitzki, *Detector Optimization for SiD*, LCWS08, Chicago.

[7] D.V. Onoprienko, *Integrated Tracking-Clustering Algorithm*, LCWS08, Chicago.

DESY 09-028
SLAC-PUB-13551
ILC-NOTE-2009-049
February, 2009

Polarimeters and Energy Spectrometers for the ILC Beam Delivery System*

S. Boogert[1], M. Hildreth[2], D. Käfer[3], J. List[3], K. Mönig[3], K.C. Moffeit[4], G. Moortgat-Pick[5], S. Riemann[3], H.J. Schreiber[3], P. Schüler[3], E. Torrence[6], M. Woods[4]

[1]Royal Holloway, University of London, UK
[2]University of Notre Dame, USA
[3]DESY, Hamburg and Zeuthen, Germany
[4]SLAC National Accelerator Laboratory, Stanford, USA
[5]IPPP, University of Durham, UK
[6]University of Oregon, USA

Abstract

This article gives an overview of current plans and issues for polarimeters and energy spectrometers in the Beam Delivery System of the ILC. It is meant to serve as a useful reference for the Detector Letter of Intent documents currently being prepared.

1 Introduction and Overview

The ILC will open a new precision frontier, with beam polarization playing a key role in a physics program that demands precise polarization and beam energy measurements. [1] The baseline configuration of the ILC, as described in the Reference Design Report (RDR), [2] provides polarized electron and positron beams, with spin rotator systems to achieve longitudinal polarization at the collider IP; upstream and downstream polarimeters and energy spectrometers for both beams; and the capability to rapidly flip the electron helicity at the injector, using the source laser. The possibility of fast positron helicity flipping is not included in the baseline configuration. A scheme for fast positron helicity flipping has been proposed. [3]

The electrons will be highly polarized with $P(e^-) > 80\%$. Positrons will also be produced with an initial polarization $P(e^+) \sim 30 - 45\%$. This expected small positron polarization can be used with great benefit for physics measurements if the possibility of fast helicity flipping of the positron spin is also provided. Excellent polarimetry for both beams, accurate to $\Delta P/P = 0.25\%$, is planned. [1, 4] Polarimetry will be complemented by e^+e^- collision data, where processes like W pair production can provide an absolute scale calibration for the luminosity-weighted polarization at the IP, which can differ from the polarimeter measurements due to depolarization in collision.

Precise beam energy measurements are necessary at the ILC in order to measure particle masses produced in high-rate processes. Measuring the top mass in a threshold scan to order 100 MeV or

*Work supported in part by the U.S. Department of Energy contract number DE-AC02-76SF00515

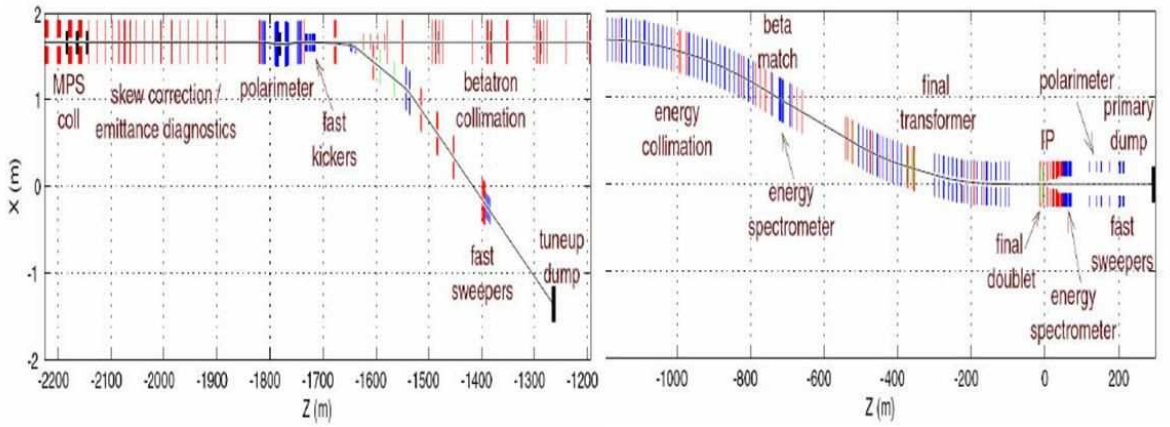

Figure 1: Beam Delivery System as described in the RDR, showing the locations of the polarimeter chicane 1800m upstream of the IR and the upstream energy spectrometer 700 m upstream of the IR. The location of the extraction line energy spectrometer and polarimeter are shown on the right side of the figure.

measuring a Standard Model Higgs mass in direct reconstruction to order 50 MeV requires knowledge of the luminosity-weighted mean collision energy $\sqrt{s}$ to a level of $(1-2)\cdot 10^{-4}$. [1, 4] Precise measurements of the incoming beam energy are a critical component to measuring the quantity $\sqrt{s}$ as it sets the overall energy scale of the collision process.

The baseline ILC described in the RDR provides collider physics with beam energies in the range 100-250 GeV. Precise polarization and energy measurements are required for this full energy range. The ILC baseline also provides for detector calibration at the Z-pole with 45.6 GeV beam energies. However, the RDR does not require accurate polarimetry or energy spectrometer measurements at the Z-pole. A proposal to modify the baseline ILC to require precise polarimetry and energy measurements at Z-pole energies was made at the *2008 Workshop on Polarization and Beam Energy Measurements at the ILC*. [4] The motivation for this includes polarimeter and energy spectrometer calibration, and physics measurements to improve on Z-pole results from LEP and SLC. The downstream polarimeter described in the RDR is expected to perform well at the Z-pole, while the upstream polarimeter is severely impacted due to inclusion of the laserwire detector and the energy collimator in the system design as noted below. For energy measurements, the downstream energy spectrometer should perform well while the upstream spectrometer needs further evaluation for how accurately the lower chicane magnetic fields can be measured.

Precise polarimeters and energy spectrometers will be installed in the Beam Delivery System (BDS) at the locations shown in Figure 1. These systems will need to be a joint effort of the ILC BDS team and the Detector collaborations, with collaboration members responsible for the performance and accuracy of the measurements. Data from the polarimeters and spectrometers must be delivered to the Detector DAQ in real time to be logged and permit fast online analysis. Fast online analysis results must also be provided to the ILC controls system for beam tuning and diagnostics. Details for the DAQ systems and assigning of responsibilities between the ILC and Detector collaborations remain to be worked out. Costing for the beamline components, conventional facilities and polarimeter laser systems are included in the ILC cost estimate. Costing for the detectors for the polarimeters and downstream energy spectrometer, and for the DAQ are expected to be provided by the Detector collaborations.

The 2008 workshop [4] also included presentations and discussions on i) physics requirements, ii) polarized sources, spin rotators and low energy polarimetry, iii) spin transport studies and iv) physics-based measurements of beam polarization and beam energy from collider data. Workshop participants included both detector and accelerator physicists. The need for close collaboration be-

tween the accelerator and detector efforts was demonstrated, as well as the need for detector physicists to play an active role in the design and evaluation of accelerator components that impact beam polarization and beam energy capabilities in addition to the polarization and energy diagnostics. Seven recommendations emerged from the workshop that need follow-up evaluations and actions from the GDE, the Detector collaborations and the Research Director. Specifically, these recommendations were:

- Relocate the laser-wire emittance diagnostic and MPS energy collimator away from the upstream polarimeter chicane.
- Modify the extraction line polarimeter chicane from 4 magnets to 6 magnets to allow the Compton electrons to be deflected further from the disrupted beam line.
- Include precise polarization and beam energy measurements for Z-pole calibration runs into the baseline configuration.
- Realize the physics potential for the initial positron polarization of 30-45%.
- Implement parallel spin rotator beamlines with a kicker system before the damping ring (DR) to provide rapid helicity flipping of the positron spin.
- Move the pre-DR positron spin rotator system from 5 GeV to 400 MeV to eliminate expensive superconducting magnets and reduce costs.
- Move the pre-DR electron spin rotator system to the source area to eliminate expensive superconducting magnets and reduce costs.

The importance of multiple energy and polarization measurements was also emphasized to realize the precision physics capabilities of the ILC. The importance of similar redundant measurements at LEP, SLC, JLAB and HERA was noted as well as similar desires for complementarity, redundancy and cross checks that two ILC Detectors provide.

2 Polarimetry

Both upstream and downstream BDS polarimeters will use Compton scattering of high power lasers with the electron and positron beams. [1, 2] Figure 2 shows the Compton cross section versus scattered electron energy for 250 GeV beam energy and 2.3 eV photon energy. There is a large polarization asymmetry for back-scattered electrons near 25.2 GeV, the Compton edge energy. The large asymmetry and the large difference between the Compton edge and the beam energy facilitate precise polarimeter measurements. The Compton edge does not change significantly for higher beam energies; this dependence is also shown in Figure 2. A spectrometer with segmented Cherenkov detectors that sample the flux of scattered electrons near the Compton edge will be used to provide good polarization measurements with high analyzing power. Compton polarimetry, utilizing measurements of back-scattered electrons near the Compton edge, is chosen as the primary polarimetry technique for several reasons:

- The physics of the scattering process is well understood QED, with radiative corrections less than 0.1% [5];
- Detector backgrounds are easy to measure and correct for by using laser off pulses;
- Compton-scattered electrons can be identified, measured and isolated from backgrounds using a magnetic spectrometer;

- Polarimetry data can be taken parasitic to physics data;
- The Compton scattering rate is high and small statistical errors can be achieved in a short amount of time (sub-1% precision in one minute is feasible);
- The laser helicity can be selected on a pulse-by-pulse basis; and
- The laser polarization is readily determined with 0.1% accuracy.

Each polarimeter requires a laser room on the surface with a transport line to the beamline underground. A configuration proposed for the extraction line polarimeter is shown in Figure 3. A similar configuration is planned for the upstream polarimeter. The polarimeters employ magnetic chicanes with parameters shown in Table 1.

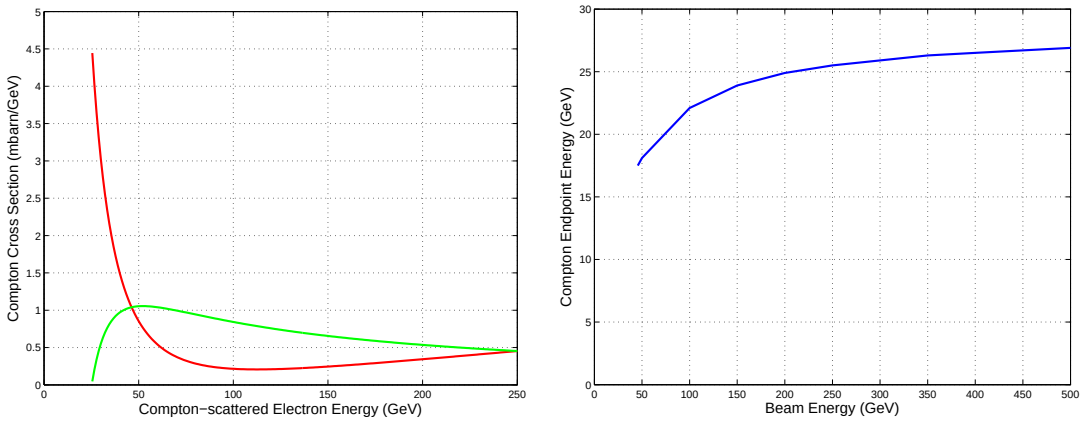

Figure 2: Left Figure: Compton differential cross section versus scattered electron energy for same (red curve) and opposite (green curve) helicity configuration of laser photon and beam electron; beam energy is 250 GeV and laser photon energy is 2.3 eV. Right Figure: Compton edge energy dependence on beam energy.

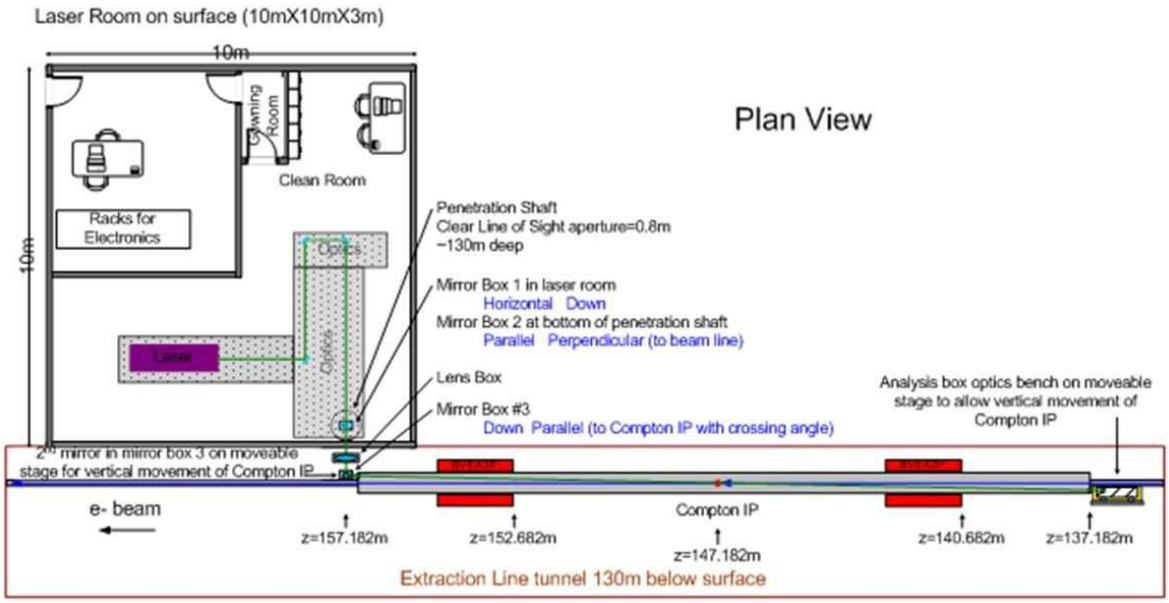

Figure 3: Proposed configuration of laser room, penetration shaft and extraction line layout for the downstream Compton polarimeter.

Table 1: Magnetic chicane parameters for the BDS Compton polarimeters.

Chicane Parameters	Upstream Polarimeter	Downstream Polarimeter
Chicane Length (m)	75.6	72.0
No. magnets	12	6
Magnetic Field (T)	0.0982	0.4170 (1, 2)
		0.6254 (3, 4)
		0.4170 (5,6)
Magnet Length (m)	2.4	2.0
Magnet 1/2-gap (cm)	1.25	11.7 (1-3)
		13.2 (4)
		14.7 (5,6)
Magnet pole-face width (cm)	10.0 (1-3)	40.0 (1-3)
	20.0 (4-9)	54.0 (4)
	30.0 (10-12)	40.0 (5-6)
Dispersion at mid-chicane at 250 GeV (mm)	20	20

2.1 Polarimeter Detectors

Design options for Cherenkov detectors are being studied: one uses gas tubes for the radiator with the Cherenkov light detected by conventional photomultiplier tubes (PMTs) or newer types of photo detectors. Figure 4 shows a schematic drawing of one such detector channel as well as the arrangement of 18 channels covering the whole exit window for the Compton electrons. The gas tubes would have a cross section of 1cm^2. C_4F_{10} is one gas being considered, which has a high Cherenkov threshold of 10 MeV. Consideration also needs to be given to gases that do not scintillate from lower energy particles. Propane was a gas chosen for the SLD polarimeter detector [6] that had a high Cherenkov threshold and low scintillation, but had a drawback of being flammable.

An alternative detector is a multi-anode photomultiplier (MAPM), where the anode is segmented into multiple pads that can be read out independently. An issue may be cross talk between the anodes, however, and will need to be studied.

Another alternative is silicon-based photomultipliers (SiPM) coupled to quartz fibers as radiator. SiPMs have excellent single photon detection capabilities and outmatch conventional PMTs in terms of robustness, size and cost. However the quartz fibers constituting the radiator material have a much lower Cherenkov threshold of 200 keV that would make them more susceptible to background radiation. [7] This may be acceptable for the upstream polarimeter, but is less likely to be acceptable for the downstream polarimeter.

Linearity and longterm stability of various photodetectors are currently studied in an LED test setup as well as in the DESY testbeam with a two channel prototype of the Cherenkov detector [7].

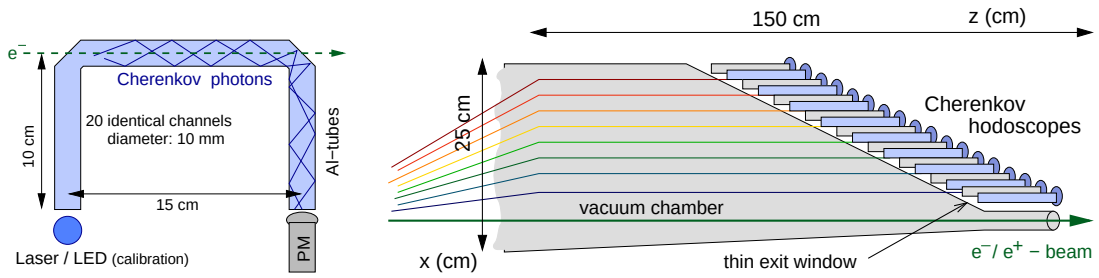

Figure 4: Schematic of a single gas tube (left) and the complete array of 18 tubes(right) as foreseen for the Cherekov detector for the polarimeters.

2.2 Upstream Polarimeter

The upstream Compton polarimeter is located at the beginning of the BDS, upstream of the tuneup dump 1800 meters before the e^+e^- IP. In this position it benefits from clean beam conditions and very low backgrounds. The upstream polarimeter configuration in the RDR is shown in Figure 5. It will provide fast and precise measurements of the polarization before collisions. The beam direction at the Compton IP in both the vertical and horizontal must be the same as that at the IP within a tolerance of $\sim 50\mu$rad.

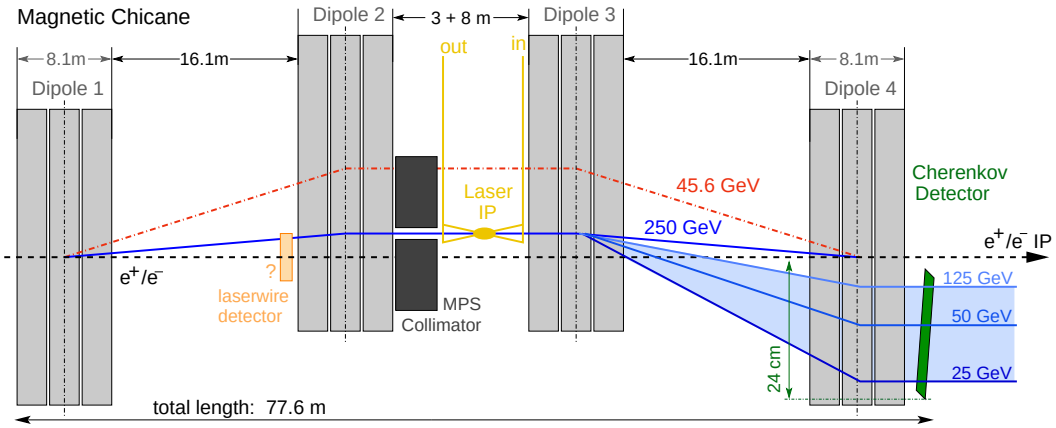

Figure 5: Schematic of the upstream polarimeter chicane [8] described in the Reference Design Report. This system combines functions for the laserwire detector, machine protection collimator and the Compton polarimeter.

The chicane has been designed such that the Compton spectrum covers 18 detector channels. This is independent of the beam energy if the magnetic field is kept constant. Instead the Compton IP moves laterally with the beam energy. Figure 6 shows a setup to adjust the laser accordingly.

The upstream polarimeter can be equipped with a laser similar to one used at the TTF/Flash source in operation at DESY. It can have the same pulse structure as the electron beam allowing measurements of every bunch. This permits fast recognition of polarization variations within each bunch train as well as time-dependent effects that vary train-by-train. The statistical precision of the polarization measurement is estimated to be 3% for any two bunches with opposite helicity, leading to an average precision of 1% for each bunch position in the train after the passage of only 20 trains (4 seconds). The average over two entire trains with opposite helicity will have a statistical error of $\Delta P/P = 0.1\%$. The systematic error goal is to achieve an uncertainty of $\Delta P/P = 0.25\%$ or better with the largest uncertainties coming from the analyzing power calibration (0.2%) and the detector linearity (0.1%). [8]

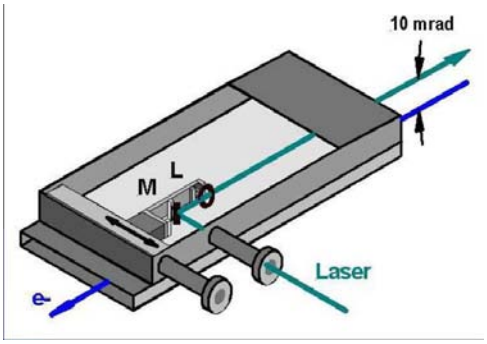

Figure 6: Movable mirror and lense focussing the laser onto the electron beam.

The RDR design for the upstream polarimeter chicane includes capability for a laserwire detector for beam emittance measurements and a machine-protection system (MPS) energy collimator. The combined functionality for these devices in the polarimeter chicane compromises some aspects of the polarimeter capabilities and operation, and recommendations to resolve this need evaluation. [4, 8]

2.3 Downstream Polarimeter

The downstream polarimeter, shown in Figure 7, is located 150 m downstream of the IP in the extraction line and on axis with the IP and IR magnets. It can measure the beam polarization both with and without collisions, thereby testing the calculated depolarization correction which is expected to be at the $(0.1 - 0.2)\%$ level.

A complete conceptual layout for the downstream polarimeter exists, including magnets, laser system and detector configuration. [9] The downstream polarimeter chicane successfully accommodates a detector for the downstream energy spectrometer and provides magnetic elements for the GAMCAL system. [9]

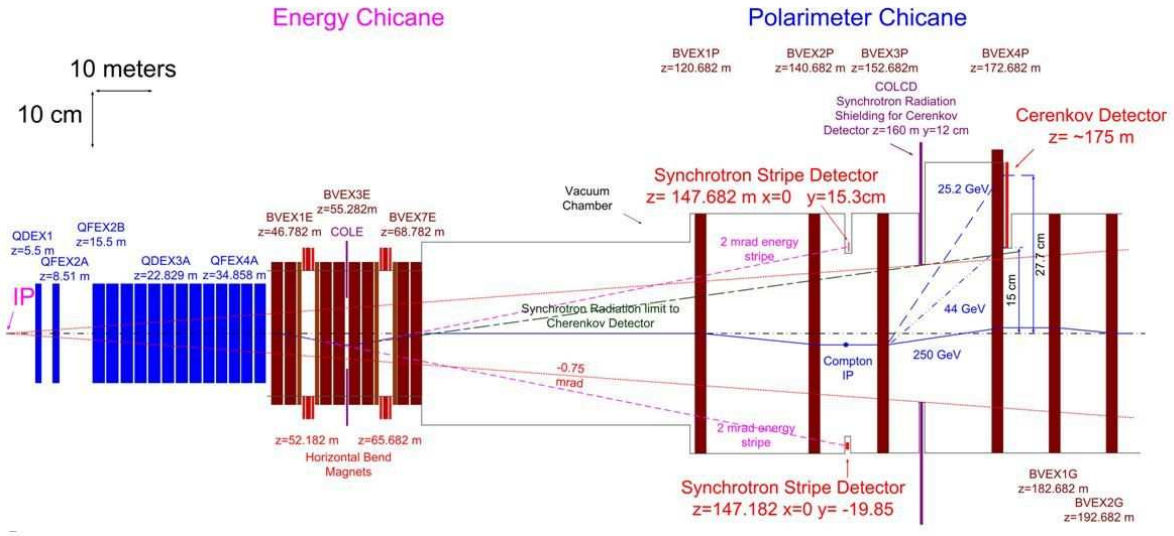

Figure 7: Schematic of the ILC extraction line diagnostics for the energy spectrometer and the Compton polarimeter.

The laser for the downstream polarimeter requires high pulse energies to overcome the larger backgrounds in the extraction line. Three 5-Hz laser systems will be used to generate Compton

collisions for three out of 2800 bunches in a train. Each laser is an all solid-state diode-pumped Nd:YAG, with a fundamental wavelength of 1064 nm that will be frequency-doubled to 532nm. Each laser will sample one particular bunch in a train for a time interval of a few seconds to a minute, then select a new bunch for the next time interval, and so on in a pre-determined pattern. The Compton statistics are high with more than 1000 Compton-scattered electrons per bunch in a detector channel at the Compton edge. With this design, a statistical uncertainty of less than 1% per minute can be achieved for each of the measured bunches. This is dominated by fluctuations in Compton luminosity due to beam jitter and laser targeting jitter and to possible background fluctuations.

Background studies have been carried out for disrupted beam losses and for the influence of synchrotron radiation (SR). There are no significant beam losses for the nominal ILC parameter set and beam losses look acceptable even for the low power option. An SR collimator protects the Compton detector and no significant SR backgrounds are expected. The systematic precision is expected to be about 0.25%, with the largest uncertainties coming from the analyzing power calibration (0.2%) and detector linearity (0.1%).

2.4 Impact of Crossing Angle and IR Magnets on Polarimetry

A crossing angle between the colliding beams means that the beam trajectory and the detector solenoid axis will be misaligned. This causes a vertical deflection of the beam and also impacts the trajectory of low energy pairs produced in the collision. [10] A detector-integrated dipole (DID) can be included in the solenoid to compensate either for the beam trajectory at the IP or the trajectory of low energy pairs as they leave the IR. To reduce backscattering of this pair background into the vertex and tracking detectors at the e^+e^- IP it is preferable to align the trajectory of low energy pairs with the extraction beamline (anti-DID solution). However, this results in a significant vertical beam angle at the IP. An example of this is shown for the SiD in Figure 8.

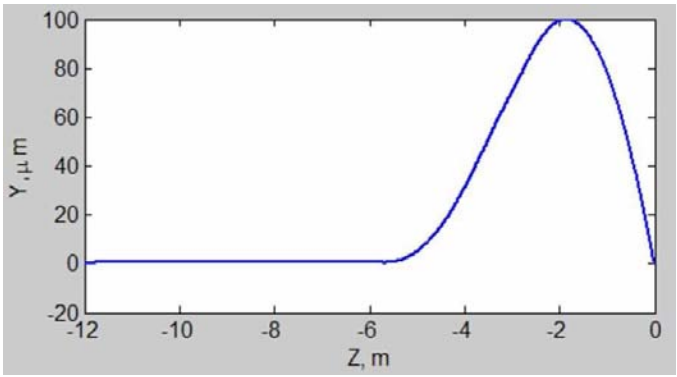

Figure 8: Vertical trajectory of the beam in SiD with anti-DID and 14-mrad crossing angle. Collider IP is at Z = 0 meters. (Taken from Figure 9 in Reference [10].)

With the anti-DID solution, additional orbit compensation is needed to achieve the goal of less than 50 μrad misalignments between the beam trajectory at the collider IP and the polarimeter Compton IPs. This compensation is energy-dependent and is not easily done by compensating the orbit at the upstream polarimeter with correctors due to tolerances on emittance growth. Corrector compensation is more easily done for the downstream polarimeter. For the upstream polarimeter, it is highly desirable to implement local orbit compensation near the IR to align the incoming vertical beam trajectory with the trajectory at the collider IP. Such a scheme looks feasible, but has not yet been fully described. [10] For the downstream polarimeter, the following procedure can be used to set the extraction line corrector magnets:

- Obtain an extraction line reference orbit with the solenoid, anti-DID and correctors off.

- Then use correctors to reproduce the reference orbit as the solenoid and anti-DID are ramped to nominal settings (can compare calculated and actual corrector settings).
- Then adjust correctors to match beam angle at the Compton IP with the collider IP angle (if non-zero).

3 Beam Energy Measurements

The ILC RDR design provides redundant beam-based measurements of the incoming beam energy, capable of achieving 10^{-4} accuracy. The measurements would be available in real time as a diagnostic tool to machine operators and would provide the basis for the determination of the luminosity-weighted center-of-mass energy for physics analyses. Physics reference channels, such as a final state muon pair resonant with the known Z-mass, are then foreseen to provide valuable cross checks of the collision scale, but only long after the data has been recorded.

The two primary methods planned for making precise beam energy measurements are a non-invasive BPM-based spectrometer, located upstream of the interaction point just after the energy collimators (Figure 1), and a synchrotron imaging detector which is located downstream of the IP in the extraction line to the beam dump (Figures 1 and 7). The BPM-based device is modeled after the spectrometer built for LEP-II, which was used to calibrate the energy scale for the W-mass measurement, although the parameters of the ILC version are much more tightly constrained by allowances on emittance dilution in the beam delivery system. The synchrotron imaging detector is similar in design to the spectrometer used at SLAC for the SLC program. Both are designed to provide an absolute measurement of the beam energy scale to a relative accuracy of 10^{-4} (100 parts per million, ppm). The downstream spectrometer, which observes the disrupted beam after collisions, can also measure the energy spectrum of the disrupted beam.

3.1 Upstream Energy Spectrometer

The RDR includes a BPM-based energy spectrometer, shown in Figure 9, located $\sim$ 700 meters upstream of the interaction point. It is important that the energy spectrometer be able to make precision energy measurements between 45.6 GeV (Z-pole) and the highest ILC energy of 500 GeV. However, due to operation with a fixed dispersion the spectrometer magnets will need to operate at low magnetic fields when running at 45.6 GeV where the magnetic field measurement may not be accurate enough. There is a research program to determine how to perform accurate magnetic field measurements for low fields.

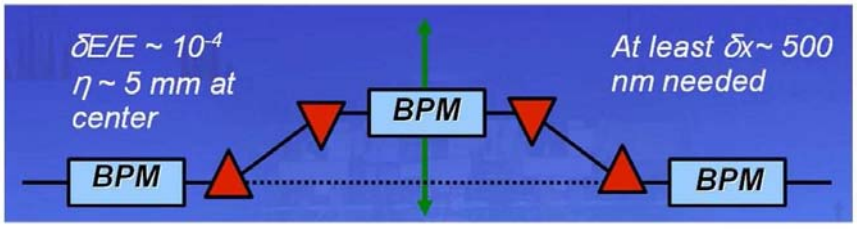

Figure 9: Schematic for the upstream energy spectrometer using precision BPMs.

A prototype test setup for such an instrument was commissioned in 2006 and 2007 in the T-474 experiment in the End Station A beamline at SLAC. The setup involved four dipole magnets and high-precision RF cavity BPMs in front, behind and in between the magnets. ESA test beams operated at 10 Hz with a bunch charge of $1.6 \cdot 10^{10}$ electrons, a bunch length of 500 μm and an energy spread

of 0.15%, i.e. with properties similar to ILC expectations. The beam energy is directly deduced from the beam offset measurements normalized to the 5 mm dispersion (same dispersion as for the present ILC baseline energy spectrometer). When combining all the BPM stations to measure the precision of the orbit over the whole ESA-chicane beamline, a resolution of 0.8 μm in x and 1.2 μm in y was achieved. The system turned out to be stable at the micron level over the course of one hour, which would translate to an energy precision of 200 ppm. [11] Additional studies are being conducted to measure and correct for motions much smaller than 1 micron.

3.2 Extraction Line Energy Spectrometer

At the SLC, the WISRD (Wire Imaging Synchrotron Radiation Detector) [12] was used to measure the distance between two synchrotron stripes created by vertical bend magnets which surrounded a precisely-measured dipole that provided a horizontal bend proportional to the beam energy. This device achieved a precision of $\Delta E_b/E_b \sim 2\cdot 10^{-4}$ (200 ppm), where the limiting systematic errors were due to relative component alignment and magnetic field mapping. The ILC Extraction-Line Spectrometer (XLS) design [13] is largely motivated by the WISRD experience. The energy spectrometer will make precision energy measurements between 45.6 GeV (Z-pole) and the highest ILC energy of 500 GeV.

The analyzing dipole for the XLS is provided by a vertical chicane just after the capture quad section of the extraction line, about 55 meters downstream of the interaction point (see Figure 7). The chicane provides a ± 2 mrad vertical bend to the beam and in both legs of the chicane horizontal wiggler magnets are used to produce the synchrotron light needed to measure the beam trajectory. The optics in the extraction line is designed to produce a secondary focus about 150 meters downstream of the IP, which coincides with the center of the polarimeter chicane and the Compton interaction point. The synchrotron light produced by the wigglers will also come to a vertical focus at this point, and position-sensitive detectors in this plane arrayed outside the beampipe will measure the vertical separation between the synchrotron stripes.

With a total bend angle of 4 mrad, and a flight distance of nearly 100 meters, the synchrotron stripes will have a vertical separation of 400 mm, which must be measured to a precision of 40 μm to achieve the target accuracy of 10^{-4}. In addition to the transverse separation of the synchrotron stripes, the integrated bending field of the analyzing dipole also needs to be measured and monitored to a comparable precision of 10^{-4}. The distance from the analyzing chicane to the detectors needs to only be known to a modest accuracy of 1 cm. For the XLS spectrometer, it has been proposed to use an array of radiation-hard 100 μm quartz fibers. These fibers do not detect the synchrotron light directly, but rather detect Cherenkov radiation from secondary electrons produced when the hard photons interact with material near the detector. At ILC beam energies, the critical energy for the synchrotron radiation produced in the XLS wigglers is several tens of MeV, well above the pair-production threshold, and copious numbers of relativistic electrons can be produced with a thin radiator in front of the fiber array. The leading candidate for reading out these fibers is multi-anode PMTs from Hamamatsu, similar in design to those used in scintillating fiber calorimeters. The advantage of this scheme over wires (as used in the SLC energy spectrometer) is to produce a reliable, passive, radiation-hard detector which does not suffer from cross talk or RF pickup, and still allows for easy gain adjustment and a large dynamic range.

The energy spectrum of the beam after collision contains a long tail as a result of the beam-beam disruption in the collision process. This disrupted beam spectrum is not a direct measure of the collision energy spectrum, but it is produced by the same physical process, and direct observation of this disrupted tail will serve as a useful diagnostic for the collision process. The position-sensitive detector in the XLS is designed to measure this beam energy spectrum down to 50% of the nominal beam energy. Near the peak, for a beam energy of $E_b = 250$ GeV, each 100-micron fiber spans an

energy interval of 125 MeV. Given a typical beam energy width of 0.15%, this means the natural width of the beam energy will be distributed across at least a handful of fibers, which will allow the centroid to be determined with a precision better than the fiber pitch, and some information about the beam energy width can be extracted as well.

3.3 Alternative Methods for Energy Measurements

R&D on three alternative methods for precise beam energy measurements with 100 ppm accuracy is being carried out by different groups. The first method utilizes Compton backscattering, a magnetic spectrometer and precise position measurements of the electron beam, the centroid of the Compton photons and the kinematic edge of the Compton-scattered electrons. [14, 15] The spectrometer length needed is about 30 m and would be located near the upstream polarimeter (or may utilize the upstream polarimeter chicane). Precise position measurements approximately 25 meters downstream of an analysis magnet are needed with accuracies of 1 μm for the Compton photons, 10 μm for the Compton edge electrons and 0.5 μm for the beam electrons.

The second method utilizes the SR emitted in the dipole magnets of the upstream BPM-based spectrometer. [16] Accurate determination of the edges of the SR fan is needed. Studies include a direct measurement of the SR fan as well as the use of mirrors to deflect soft SR light to detectors located away from the beamline. Novel high spatial resolution detectors are considered.

A third method relies on the Resonance Absorption method. [17, 18] Under certain conditions, laser light can be absorbed by beam particles when both co-propagate in close proximity in a solenoid. The beam energy can be inferred from the measured dependence of light absorption on the magnetic field and laser wavelength.

4 Summary

Concepts for high precision polarization and energy measurements exist. These concepts have resulted in detailed system layouts that are included in the RDR description for the Beam Delivery System. The RDR includes both upstream and downstream polarimeters and energy spectrometers for both beams. This provides needed complementarity and redundancy for achieving the precision required, with adequate control and demonstration of systematic errors.

The BDS polarimeters and energy spectrometers need to be a joint effort of the ILC BDS team and the Detector collaborations, with collaboration members responsible for the performance and accuracy of the measurements. Details for this collaboration and assigning of responsibilities remain to be worked out. There is also a demonstrated need for Detector physicists to play an active role in the design and evaluation of accelerator components that impact beam polarization and beam energy capabilities, including the polarized source and spin rotator systems. A workshop was held in 2008 on ILC Polarization and Energy measurements, which resulted in a set of recommendations for the ILC design and operation. Additional input and action is needed on these from the Detector collaborations, the Research Director and the GDE.

Work is continuing during the ILC engineering design phase to further optimize the polarimeter and energy spectrometer concepts and fully implement them in the ILC. This includes consideration for alternative methods, detailed design and cost estimates, and prototype and test beam activities.

References

[1] G. Moortgat-Pick et al. The role of polarized positrons and electrons in revealing fundamental interactions at the linear collider. *Phys. Rept.*, 460:131–243, 2005.

[2] N. Phinney, N. Toge and N. Walker Editors, *International Linear Collider Reference Design Report - Volume 3: Accelerator*, http://www.linearcollider.org/cms/?pid=1000437 (2007).

[3] K.C Moffeit, P. Bambade, K. Moenig, P. Schuler, M. Woods, *Spin Rotation Schemes at the ILC for Two Interaction Regions and Positron Polarization with both Helicities*, LCC-159, SLAC-TN-05-045 (2005); K.C. Moffeit, D. Walz and M. Woods, *Spin Rotation at lower energy than the damping ring*, ILCNOTE-2008-040 IPBI TN-2008-1 (2008); and K.C. Moffeit, *Spin Rotation before the Damping Ring*, IPBI TN-2008-3, Proceedings of Workshop on Polarization and Beam Energy Measurements, Zeuthen (2008).

[4] B. Aurand et al., *Executive Summary of the Workshop on Polarisation and Beam Energy Measurement at the ILC*, DESY-08-099, ILC-NOTE-2008-047, SLAC-PUB-13296 (2008); Workshop website is https://indico.desy.de/conferenceDisplay.py?confId=585.

[5] M.L. Swartz. A complete order alpha**3 calculation of the cross-section for polarized compton scattering. *Phys. Rev.*, D58:014010, 1998.

[6] SLD Collaboration, Phys. Rev. Lett. **70**, 2515 (1993); SLD Collaboration., Phys. Rev. Lett. **8678**, 11622075 (20011997); R. Elia, SLAC-Report-429 (1994); R. King, SLAC-Report-452, 1994; A. Lath, SLAC-Report-454, 1994; E. Torrence, SLAC-Report-509, 1997.

[7] D. Kaefer, *Compton Cherenkov Detector Development for ILC Polarimetry*, Proceedings of LCWS08, Chicago (2008), arXiv:0902.3221v1 [physics.ins-det].

[8] J. List and D. Kaefer, *Improvements to the ILC Upstream Polarimeter*, Proceedings of LCWS08, Chicago (2008), arXiv:0902.1516v1 [physics.ins-det]; J. List, *The ILC Upstream Polarimeter*, Proceedings of Workshop on Polarization and Beam Energy Measurements, Zeuthen (2008).

[9] K.C. Moffeit et al., *Proposal to modify the polarimeter chicane in the ILC 14 mrad extraction line*, SLAC-PUB-12425, IPBI TN-2007-1, (2007); K.C Moffeit, *Downstream Extraction Line Polarimeter*, IPBI TN-2008-5, Proceedings of Workshop on Polarization and Beam Energy Measurements, Zeuthen (2008).

[10] A. Seryi, T. Maruyama, and B. Parker, *IR Optimization, DID and anti-DID*, SLAC-PUB-11662 (2006).

[11] M. Slater et al., Nucl. Instrum. Meth. **A592**, 201-217 (2008).

[12] F. Rouse et al. *Measuring the Mass and Width of the Z0: The Status of the Energy Spectrometers*, SLAC-PUB-4977 (1989).

[13] E. Torrence, *Downstream Synchrotron Radiation Stripe Spectrometer Status*, Presentation at 2008 Workshop on Polarization and Energy Measurements at the ILC.

[14] N. Muchnoi,H.J. Schreiber, M. Viti, *ILC Beam Energy Measurement by means of Laser Compton Backscattering*, e-Print: arXiv:0812.0925 [physics.ins-det] (2008).

[15] N. Muchnoi, *Proposal for Eb Measurement at Novosibirsk Using Compton Backscattering*, Presentation at 2008 Workshop on Polarization and Beam Energy Measurements at the ILC.

[16] K. Hiller, R. Makarov, H.J. Schreiber, E. Syresin, and B. Zalikhanov, *ILC Beam Energy Measurement Based on Synchrotron Radiation from a Magnetic Spectrometer*, Nucl. Instrum. Meth. **A580** 1191 (2007).

[17] R. Melikian, *Development of the Theory of Measurement of Electron Beam Absolute Energy by Resonance Absorption Method*, Presentation at 2008 Workshop on Polarization and Beam Energy Measurements at the ILC.

[18] A. Ghalumyan, *Experiment Proposal for Eb Measurement using the Resonance Absorption Method*, Presentation at 2008 Workshop on Polarization and Beam Energy Measurements at the ILC.